Interferometric Intensity Correlation: From Sensing to Imaging

---

Khaled Kassem

Submitted in fulfilment of the requirements for the
Degree of Doctor of Philosophy

School of Physics and Astronomy
College of Science and Engineering
University of Glasgow

Abstract

Second-order intensity correlations ($g^{(2)}$) of the optical field offer a robust framework for various applications due to their inherent resistance to phase noise and independence from temporal or spatial coherence, relying solely on intensity measurements. This thesis demonstrates the feasibility and advantages of this approach effectively.

The first project applies the $g^{(2)}$ detection method to microscopy. Initially, a single laser beam with a 10 nm bandwidth was used to achieve micron-level axial resolution, demonstrated with a biological sample. We then enhanced the resolution by using two laser beams of 10 nm bandwidth, separated by a wavelength of 150 nm, achieving nanometric axial resolution, as demonstrated by measuring a 5 nm step in a 10-layer graphene sample.

Next, we extend the dual-wavelength approach used in microscopy to synthetic wavelength holography, a technique commonly applied in non-line-of-sight imaging. We demonstrate that our method offers several advantages, including phase noise resistance and enhanced light gathering through the use of a larger aperture, which are crucial in low-light scenarios. This is validated by imaging through various scatterers: first, by imaging through two thin glass diffusers, then through 2.3 cm of optically thick volume scatterer, and finally by showing that we can measure while the scatterer is moving (dynamic), demonstrating our robustness to fluctuations induced by changes in the scattering medium.

Moreover, the potential of a dual-comb laser modality is tested within the experimental setup, aiming to enhance both speed and robustness by eliminating the necessity for mechanical scanning. By leveraging the dual-comb laser's ability to perform optical delay scanning without mechanical movement, this method offers greater flexibility in terms of range and resolution. Proof-of-principle measurements substantiate this advancement and discuss both the potential of dual-comb lasers and the further developments needed to make them useful and applicable in practical scenarios.

Finally, we highlight the broad range of possible applications for $g^{(2)}$ methods, emphasizing how this work lays the foundation for future projects. By combining these techniques with emerging technologies, there is great potential to tackle new challenges and further expand the impact of this work in various fields.

Acknowledgements

بِسْمِ اللَه الرَحمَنِ الرَحيمِ

I am deeply grateful for the strength and guidance my faith has provided me throughout this journey. This PhD has been a transformative path of growth, learning, and discovery, and I owe immense gratitude to those who have supported and encouraged me along the way

First and foremost, I would like to express my heartfelt gratitude to my parents, whose hard work and dedication provided me with the education and opportunities that have led me to this moment. Their sacrifices, love, and unwavering belief in me have been a constant source of strength throughout this journey. To my sisters, your playful teasing, unwavering kindness, and steadfast presence have brought countless smiles to my face and made my journey a little lighter. And to my fiancé, your patience and encouragement have meant the world to me, helping me navigate the challenges of this PhD with love and unwavering strength.

I extend my deepest gratitude to my PhD supervisor, Daniele Faccio, for his invaluable guidance, mentorship and support throughout this journey. I am also incredibly grateful to Ashley Lyons, whose advice and insights have been instrumental for this work.

To my dear friends in Glasgow and all my colleagues in Extreme Light, your friendship and collaboration have made this experience truly memorable. I am grateful to all the research groups I've had the pleasure of working with for their contributions and shared knowledge along the way.

Declaration

I hereby declare that all work presented and figures produced in this thesis were conducted by the author unless otherwise explicitly stated.

Sections 4.3 and 5.3 describe experiments conducted as part of a collaboration, with individual contributions clearly detailed in the thesis outline.

Contents

List of Figures

Abbreviations

Λ	synthetic wavelength
φ_{CEO}	Carrier-Envelope Phase
$g^{(1)}$	First-Order Correlation
$g^{(2)}$	Second-Order Correlation
ASM	Angular Spectrum Method
AWG	Arbitrary Wave Generator
BS	Beam-Splitter
CANDi	Counterpropagating All-Normal Dispersion
DCANDi	Dynamically Tuned Counterpropagating All-Normal Dispersion
DCS	Diffuse Correlation Spectroscopy
DHM	Digital Holographic Microscopy
FI	Fisher Information
HBT	Hanbury Brown and Twiss
HOM	Hong-Ou-Mandel
IGM	Interferogram
IRF	Instrument Response Function
ITSM	imaging through scattering media
LiDAR	Light Detection and Ranging
LOS	Line-of-Sight
MTS	Mechanical Translation Stage
MZ	Mach-Zehnder
NLOS	Non-Line-of-Sight
OCT	Optical Coherence Tomography
PCM	Phase-Contrast Microscope
PDF	Probability Density Function
QPI	Quantitative Phase Imaging
RF	Radio Frequency
RIN	Relative Intenstiy Noise
ROI	region-of-interest
SLIM	Spatial Light Interference Microscopy
SLM	Spatial Light Modulator
SNR	Signal-to-Noise Ratio
SPAD	Single Photon Avalanche Diode
SWH	Synthetic-Wavelength Hologram

SWL	Synthetic-Wavelength
TCSPC	Time-Correlated Single Photon Counting
ToF	Time-of-Flight
TV	Total-Variation
USAF	United State Air Force
VSD	virtual source/detector

Truth is sought for its own sake. And those who are engaged upon the quest for anything for its own sake are not interested in other things. Finding the truth is difficult, and the road to it is rough.

Ibn Al-Haytham (c. 1011)- 'the father of modern optics'

Chapter 1.

Introduction

1.1 Thesis Outline

This thesis investigates imaging techniques utilizing second-order correlation ($g^{(2)}$) methods, spanning applications from high-resolution microscopy to imaging through scattering media. The research is organised into three core projects, each employing $g^{(2)}$ correlations in innovative ways to address key challenges in optical imaging.

Chapter 2 introduces the fundamental concepts of coherence and higher-order correlation of light, starting with a comprehensive theoretical background that covers both classical and quantum perspectives. It discusses interferometric methods, deriving the Second-Order Correlation ($g^{(2)}$) equations, and explains the fundamental principles of coherence functions and how they are applied in $g^{(2)}$ measurements. The chapter also explores the dual-wavelength approach and introduces a new term into these calculations, while concluding with a discussion on the implications of normalization and the significance of decorrelation time. This theoretical foundation prepares the reader for the experimental work that follows, highlighting the significance of the developed techniques and their impact on the field. All derivations, calculations, and simulations presented in this chapter were carried out by the author.

Chapter 3 introduces the first application of $g^{(2)}$ correlation in high-resolution imaging, focusing on Time-of-Flight (ToF) widefield microscopy using $g^{(2)}$ correlations. The chapter begins with an overview of existing depth imaging techniques, discussing their advantages and limitations. It then details the development of single-wavelength and dual-wavelength $g^{(2)}$ approaches for depth sensing in microscopy, showcasing their ability to achieve axial resolutions down to several nanometres, while remaining robust against phase noise. A Fisher information analysis highlights the enhanced resolution offered by the dual-wavelength approach. Finally, the chapter explores alternative $g^{(2)}$-based methods for microscopy applications. The experimental work and data analysis for this chapter were developed and executed solely by the author.

Chapter 4 shifts focus to a completely different domain: Imaging through scattering media (ITSM). In this chapter, the $g^{(2)}$ correlation principle is applied to synthetic wavelength holography for imaging through scattering media. The experimental setup was designed and built by the author at the University of Arizona in collaboration with Prof. Florian Willomitzer and Patrick Cornwall, with Patrick Cornwall providing hands-on assistance. The algorithm development

and data analysis were carried out solely by the author, except for the iterative optimization algorithm, which was contributed by Areeba Fatima (University of Glasgow). Prof. Willomitzer contributed through discussions and collaborative input. It begins by reviewing the current state-of-the-art methods in Non-Line-of-Sight (NLOS) imaging and ITSM before introducing Synthetic-Wavelength Holograms (SWHs) and their applications. The chapter then details the experimental setup, describing the generation of SWH through $g^{(2)}$ techniques. Various settings, such as static and dynamic diffusers and volume scatterers, are explored to demonstrate the versatility of this approach. Finally, the chapter highlights the potential impact of these findings for applications in fields like autonomous navigation and medical imaging.

Chapter 5 explores the possibility of replacing traditional mechanical translation stages with a dual-comb system, offering the potential for simplified, more robust, and faster operation. It begins by explaining the fundamental principles of frequency-comb and dual-frequency-comb lasers, followed by a focus on the specific case of dynamically tunable dual-comb systems, highlighting their advantages and operating mechanisms. The chapter then presents proof-of-principle methods and experimental measurements, discussing the challenges encountered and findings. Additionally, a more advanced technique for calculating the $g^{(2)}$ curve is introduced to mitigate the effects of jitter and noise. The dual-comb laser was provided by Prof. Shu-Wei Huang and Neeraj Prakash from the University of Colorado Boulder. The author developed the $g^{(2)}$ measurement method and designed the experiment. The experiments, including additional interferometer configurations, were conducted collaboratively by Neeraj Prakash and the author at the University of Colorado Boulder. The data analysis was performed solely by the author. Additionally, the author contributed to developing a new and more stable method for triggering the dynamic scan using an optical reference signal.

The thesis concludes in **Chapter 6** with a synopsis of the main findings and a discussion of future directions. The versatility and ease of implementation of $g^{(2)}$ techniques are emphasized, along with their potential to address challenges in dynamic scattering environments. Future work is expected to focus on refining single-shot imaging methods, incorporating on-chip processing for real-time applications, and expanding the use of dual-comb lasers in both scientific and industrial contexts.

1.2 Publications & Conferences

The following journal papers and conference contributions were published or submitted during my PhD. The papers relevant to this thesis are highlighted, while the other contributions fall outside the scope of this work.

- **Kassem, K.**, Caramazza, P., Mitchell, K. J., Miller, M., Emadi, A., & Faccio, D. (2022). *Real-time scene monitoring for deaf-blind people*. Sensors, 22(19), 7136.
- Mitchell, K., **Kassem, K.**[1], Kaul, C., Kapitany, V., Binner, P., Ramsay, A., ... & Murray-Smith, R. (2023, June). *mmSense: Detecting Concealed Weapons with a Miniature Radar Sensor*. In ICASSP 2023-2023 IEEE International Conference on Acoustics, Speech and Signal Processing (ICASSP) (pp. 1-5). IEEE.
- Cornwall, P., Forschner, S., **Kassem, K.**, Matito, M. B., Balaji, M. M., Katsaggelos, A., Faccio, D., & Willomitzer, F. (2024). *Single-Shot Synthetic Wavelength Imaging Through Scattering Media.* Optica Open.
- Kaul, C., Mitchell, K. J., **Kassem, K.**[1], Tragakis, A., Kapitany, V., Starshynov, I., ... & Faccio, D. (2024). *AI-Enabled Sensor Fusion of Time-of-Flight Imaging and mmWave for Concealed Metal Detection*. Sensors, 24(18), 5865.
- **Kassem, K.**, Lyons, A., Fatima, A., Cornwall, P., Willomitzer, F., & Faccio, D. (2024, July). *Second Order Correlation Interference Imaging*. In Computational Optical Sensing and Imaging (pp. CF1B-4). Optica Publishing Group.
- Lyons, A., **Kassem, K.**, Radford, J. & Faccio, D. (2024, March). *Dual wavelength Hong-Ou-Mandel imaging*. In Quantitative Phase Imaging X (p. PC1285201). SPIE.
- **Kassem, K.**, Lyons, A., Binner, P. & Faccio, D. (2024, September). *Time-of-Flight Wide-field Microscopy*. In Review

[1] Co-First Author

Chapter 2.

Background

2.1 Coherence

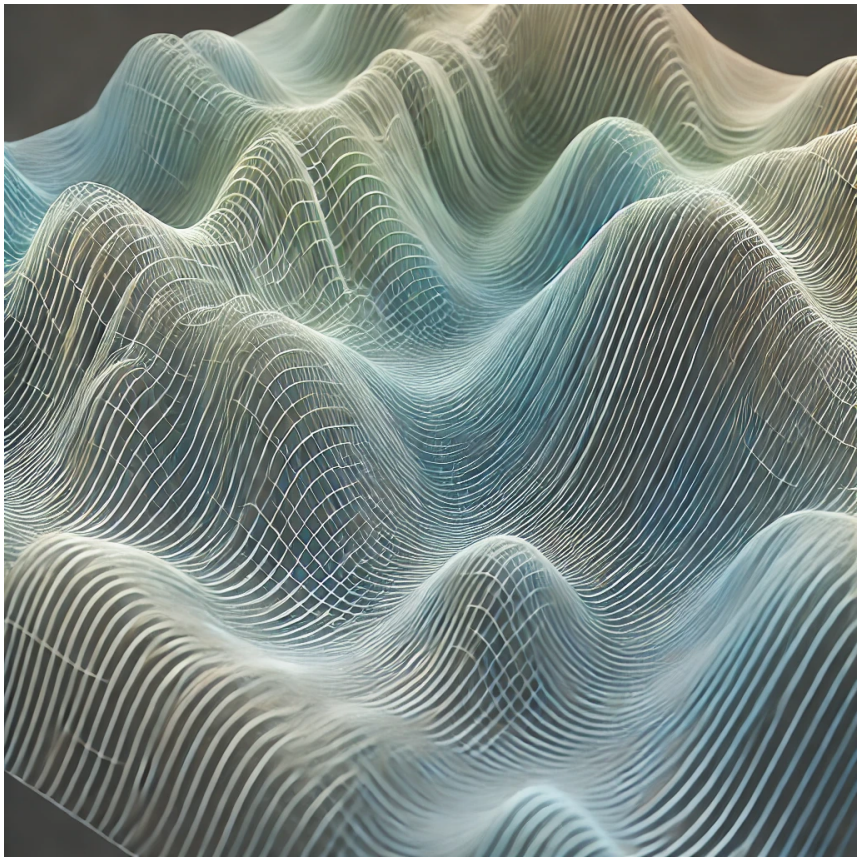

Figure 2.1: **Coherence:** A schematic illustrating the interference of coherent waves, resulting in the formation of a standing wave pattern. This image was created using Dall-E 3.

The propagation of light can be described through the Maxwell equations [1, 2]. In the vacuum they are linear differential equations, indicating that when multiple fields interact, the resulting field can be expressed as the sum or superposition of all individual fields. A key aspect of this interaction is how these fields are interconnected and how they change in relation to one another, a concept encapsulated by coherence. Coherence is fundamental to the field of optics, formally describing the phase relationship or degree of correlation between waves at different points in space and time, and it plays a crucial role in interference phenomena. A light field is considered coherent when its electric field values maintain a fixed phase relationship, either across space or over time. Spatial coherence describes a consistent phase relationship between different points across the beam spatial profile, while temporal coherence refers to the correlation

of the field at a fixed location but at different times.

To measure or describe coherence of a system, nth-order correlation functions are utilized [3, 4]. In many cases of interest, these functions can quantify the system in terms of its degree of coherence. In this section, we will discuss first- and second-order coherence. First-order coherence is crucial for experiments such as Young's double-slit and general interferometry. It is defined by the correlation of electric fields, which is why it is sometimes referred to as field correlation. Mathematically, the first-order coherence function $g^{(1)}(x_1, t_1; x_2, t_2)$ is expressed as

$$g^{(1)}(x_1, t_1; x_2, t_2) = \frac{\langle E^*(x_1, t_1) E(x_2, t_2) \rangle}{\sqrt{\langle |E(x_1, t_1)|^2 \rangle \langle |E(x_2, t_2)|^2 \rangle}}, \tag{2.1}$$

where $E(x, t)$ represents the electric field at position x and time t, and the angled brackets denote ensemble averaging over many pulses/photons. The magnitude of $g^{(1)}(x_1, t_1; x_2, t_2)$ is upper and lower bounded and can classify coherence in the following way:

$$\begin{aligned} |g^{(1)}| &= 1 \quad \text{(completely coherent)} \\ 0 < |g^{(1)}| &< 1 \quad \text{(partly coherent)} \\ |g^{(1)}| &= 0 \quad \text{(not coherent)} \end{aligned} \tag{2.2}$$

For coherent light, $|g^{(1)}|$ is determined by the degree to which the fields are similar across various degrees of freedom. For monochromatic light (with infinite coherence time), $g^{(1)}$ is predominantly determined by the balance of the field amplitudes and polarization. While this discussion focuses on the ideal case of monochromatic light, non-monochromatic light introduces additional complexities. It has a non-zero linewidth, which imposes further limitations on coherence in time. We can define the coherence length l_{coh} and time τ_{coh} for a uniform spectral distribution over which light stays coherent as,

$$\tau_{coh} = \frac{1}{\Delta\omega} \quad , \quad l_{coh} = c \cdot \tau_{coh}, \tag{2.3}$$

where c is the speed of light. In reality, the spectrum is non-uniform and follows a Gaussian spectral distribution; therefore, we redefine the coherence properties as follows [5]:

$$\tau_{coh} = \frac{2\ln(2)}{\pi\Delta\omega} \tag{2.4}$$

Second-order coherence describes the statistical properties of light fields beyond the traditional descriptions based solely on amplitude and phase. The second-order coherence function $g^{(2)}(x_1, t_1; x_2, t_2)$ is defined as [3]:

$$g^{(2)}(x_1, t_1; x_2, t_2) = \frac{\langle E^*(x_1, t_1)E^*(x_2, t_2)E(x_2, t_2)E(x_1, t_1)\rangle}{\langle |E(x_1, t_1)|^2\rangle\langle |E(x_2, t_2)|^2\rangle}. \tag{2.5}$$

In classical terms, this function represents the correlation of intensities rather than electric fields. The Hanbury Brown and Twiss (HBT) effect demonstrated that we can utilize second-order correlations to extend our understanding of light beyond classical descriptions, allowing us to analyse phenomena such as photon bunching and anti-bunching [6, 7]. Their work underscored the importance of second-order coherence in understanding photon statistics and highlighted the need to extend classical coherence theory into the quantum realm. The value of $g^{(2)}$ is theoretically not upper-limited and can go to infinity. For coherent monochromatic light that follows a Poissonian distribution, $g^{(2)}$ equals 1 at all times, meaning there is no correlation. For chaotic light that follows a super-Poissonian distribution (e.g., from a thermal source), which exhibits bunching, Siegert formulated the relation showing the connection between $g^{(1)}$ and $g^{(2)}$ [8]:

$$g^{(2)}(t_1, t_2) = 1 + |g^{(1)}(t_1, t_2)|^2 \tag{2.6}$$

Since $|g^{(1)}(t_1, t_2)|$ can range between 0 and 1, this means that for chaotic light, the $g^{(2)}$ can take values between 1 and 2. $g^{(2)} = 2$, is the limit for classical sources, but it can be higher for quantum sources (e.g., photon pairs), where we encounter super-bunched sources. For quantum sources, the $g^{(2)}$ can also fall below 1 for sub-Poissonian statistics, as is the case for a single-photon source. We often compare the different regimes for the stationary case and $(t_1 = t_2)$ as follows [9]:

$$\begin{aligned} |g^{(2)}| &> 2 \quad \text{(super-bunched)} \\ 1 < |g^{(2)}| &< 2 \quad \text{(bunched)} \\ |g^{(2)}| &= 1 \quad \text{(coherent)} \\ |g^{(2)}| &< 1 \quad \text{(anti-bunched)} \end{aligned} \tag{2.7}$$

These are the values when measuring the $g^{(2)}$ of the intensities directly from the light source.

Glauber was the one who first introduced the correlation functions in reference to the coherence properties of fields [10, 11]. His theory, inspired by inspired by the HBT experiment, aimed to establish a standard description of classical and quantum higher-order coherence, deepening our understanding of classical interference while paving the way for quantum optics. His work highlighted the degree of correlation between waves at different points in space and time, revealing quantum mechanical properties of light that challenge classical wave theories. The HBT effect demonstrated the correlation of light through coincidence measurements, prompting

Glauber to create a quantum framework for coherence analysis that bridges classical optics with quantum phenomena. In this framework, classical optical coherence serves as the classical limit for first-order quantum coherence, while higher-order coherence accounts for essential quantum phenomena such as photon bunching and anti-bunching. Today, coherence remains pivotal in cutting-edge technologies like quantum information processing, secure communications, and high-precision measurements, where controlling the coherence properties of light is essential. For his pioneering contributions, Glauber was awarded the Nobel Prize in Physics in 2005 "for his contribution to the quantum theory of optical coherence," and his formalism continues to lay the foundation for modern quantum optics.

Having established the fundamental concepts of coherence and its various orders, we now turn our attention to interference phenomena, where these principles come to life.

2.2 Interference

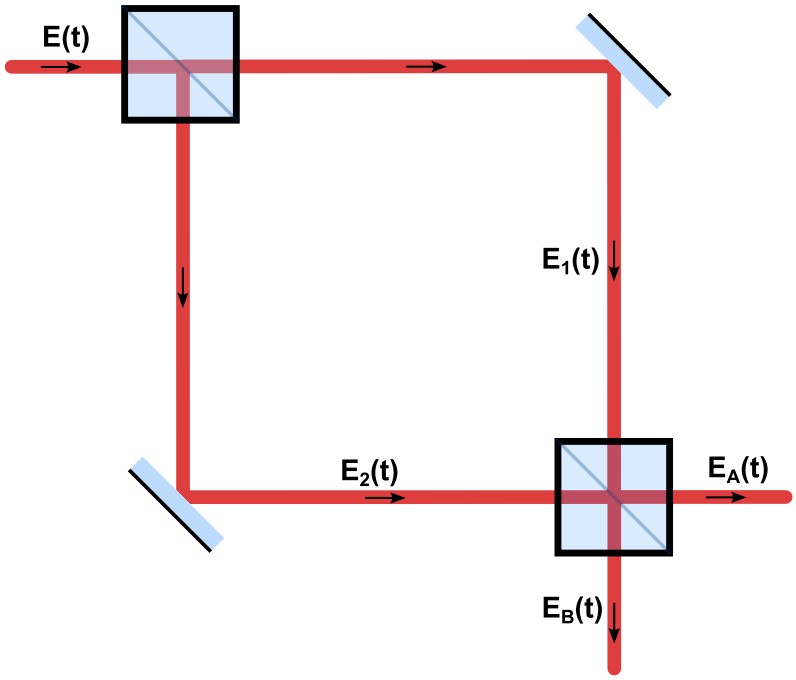

Figure 2.2: **Single Wavelength Mach-Zehnder Interferometer:** Schematic of the electric fields in a Mach-Zehnder interferometer. The single-wavelength input field $E(t)$ is split into two paths, $E_1(t)$ and $E_2(t)$, and then recombined at the exit beamsplitter, producing interference at outputs A and B.

The phenomenon of optical interference has been well known since the time of Robert Hooke

and Isaac Newton, who significantly advanced our understanding of light as a wave. Interferometric methods have been utilized in research since the pioneering work of Albert A. Michelson, whose innovative application of the interferometer earned him the Nobel Prize in Physics in 1907 [12].

Interference occurs when measuring the intensities of a superposition of fields that are at least partially coherent. Characteristic patterns of bright and dark fringes arise from the phase relationships between the interacting waves; constructive interference happens when the path difference is an integer multiple of the wavelength, while destructive interference occurs when it is an odd multiple of half the wavelength. These fundamental principles not only deepen our understanding of wave behaviour but also lay the groundwork for various practical applications, including high-precision measurements and advanced imaging techniques.

Among the many interferometric configurations, the Mach-Zehnder (MZ) interferometer [13] stands out for its versatility in investigating wavefronts and phase shifts. This setup consists of two lossless and perfectly balanced beam splitters and two mirrors, creating two unique optical paths. When light enters the first beam splitter, it is divided into two beams that traverse different paths before recombining at the second beam splitter. This design enables the measurement of phase shifts resulting from changes in optical path length, variations in refractive index, or external influences.

In the context of analysing second-order interferometric correlations, the Mach-Zehnder interferometer serves as a prime example. Here, an incoming electric field $\mathbf{E}$ is split into two distinct paths, producing the electric fields E_1 and E_2, as illustrated in Fig. 2.2. These fields then recombine at a beamsplitter, creating a sum of fields measured at the output of the interferometer. For simplification, we assume identical electric field amplitudes and co-located fields in space, allowing us to treat the problem in only the time and frequency domains. The electric fields at the output ports, labelled E_A and E_B, can be expressed as:

$$\begin{aligned} E_A(t_1, t_2, t) &= \frac{1}{\sqrt{2}} \left[E_1(t - t_1) + j E_2(t - t_2) \right], \\ E_B(t_1, t_2, t) &= \frac{1}{\sqrt{2}} \left[E_2(t - t_2) + j E_1(t - t_1) \right], \end{aligned} \tag{2.8}$$

where t is the global time, and t_i represents the time taken by the electric field to traverse path i in the interferometer. Assuming plane waves for the electric fields in both paths, we can express the individual fields as:

$$E_i(t) = |E_0| e^{j(\omega_i t + \varphi_i)}, \tag{2.9}$$

where $|E_0|$ denotes the amplitude of the electric field, ω_i is the frequency of the field, and φ_i is the phase. If the interferometer is not balanced in electric field amplitude, this can introduce additional complexity to our analysis.

To measure the intensity at each output port, we define the intensities in terms of the electric fields:

$$I_i(t_1, t_2) = \langle E_i^*(t_1, t_2, t) E_i(t_1, t_2, t) \rangle, \tag{2.10}$$

where $\langle \cdot \rangle$ represents the ensemble average over t. The intensity at port A can be computed with Eq. (2.8) as follows:

$$I_A(t_1, t_2) = \frac{|E_0|^2}{2} \langle \left[e^{i(\omega_1(t-t_1)+\varphi_1)} + i e^{i(\omega_2(t-t_2)+\varphi_2)} \right] \left[e^{-i(\omega_1(t-t_1)+\varphi_1)} - i e^{-i(\omega_2(t-t_2)+\varphi_2)} \right] \rangle. \tag{2.11}$$

Next, we need to consider finite coherence length by accounting for the non-zero spectral bandwidth, which necessitates adding a mutual coherence term $g^{(1)}_{(t_2-t_1)}$ that describes the degree of coherence between the two electric fields [5, 14]. We can then rewrite the intensity at port A as:

$$I_A(t_1, t_2) = \frac{|E_0|^2}{2} \langle 2 + |g^{(1)}_{(t_2-t_1)}| \left(i e^{-i(\omega_2(t-t_2)+\varphi_2)} e^{-i(\omega_1(t-t_1)+\varphi_1)} - i e^{i(\omega_1(t-t_1)+\varphi_1)} e^{-i(\omega_2(t-t_2)+\varphi_2)} \right) \rangle. \tag{2.12}$$

To simplify this further, we can apply the trigonometric identity $\sin(x) = \frac{e^{ix} - e^{-ix}}{2i}$. The intensity at port A can now be expressed as:

$$I_A(t_1, t_2) = |E_0|^2 \left(1 + |g^{(1)}_{(t_2-t_1)}| \langle \sin\left(\omega_2 t_2 - \omega_1 t_1 - \Delta\omega t - \Delta\varphi \right) \rangle \right), \tag{2.13}$$

where $\Delta\omega = \omega_2 - \omega_1$ is the frequency difference of the fields in both paths, and $\Delta\varphi = \varphi_2 - \varphi_1$ is the phase difference. In the case where the frequencies are identical ($\omega_1 = \omega_2 = \omega$) , as shown in Fig. 2.2, and assuming coherent inputs, where the phase difference $\Delta\varphi$ remains constant, we can simplify the expression by substituting $\Delta t = t_2 - t_1$:

$$I_A(\Delta t) = |E_0|^2 \left(1 + |g^{(1)}_{(\Delta t)}| \sin(\omega \Delta t - \Delta\varphi)\right). \tag{2.14}$$

The intensity at port B can be written correspondingly as:

$$I_B(\Delta t) = |E_0|^2 \left(1 - |g^{(1)}_{(\Delta t)}| \sin(\omega \Delta t - \Delta\varphi)\right). \tag{2.15}$$

$I_A(\Delta t)$ & $I_B(\Delta t)$ are shown in Fig. 2.3(a). In the case of mutually incoherent fields E_1 & E_2, where the phase difference $\Delta\varphi$ varies randomly during a measurement, the sinusoidal term averages out to zero, resulting in no measurable interference (see Fig. 2.3(b)). In this scenario, the intensities at both ports become equal:

$$\begin{aligned} I_A(\Delta t) &= |E_0|^2 = I_0, \\ I_B(\Delta t) &= |E_0|^2 = I_0. \end{aligned} \tag{2.16}$$

2.3 Second-Order Correlation

Moving on to second-order correlations, the second-order correlation function is defined as [10, 3]:

$$g^{(2)}(t_1, t_2) = \frac{\langle E_1^*(t_1) E_2^*(t_2) E_1(t_2) E_2(t_1)\rangle}{\langle |E_1(t_1)|^2 \rangle \langle |E_2(t_2)|^2 \rangle}. \tag{2.17}$$

By expressing the second-order correlation function in terms of classical intensities, we can rewrite it as:

$$g^{(2)}(t_1, t_2) = \frac{\langle I_1(t_1) I_2(t_2)\rangle}{\langle I_1(t_1)\rangle \langle I_2(t_2)\rangle}. \tag{2.18}$$

To simplify the notation, we can redefine the time variables such that $t_1 = t$ and $t_2 = t + \tau$. Furthermore we add a new variable Δt which defines the optical delay between the two arms of the interferometer. Hence, substitute I_i for $I_X(t, \Delta t)$ or $I_Y(t, \Delta t)$:

$$g^{(2)}_{XY}(\Delta t, \tau) = \frac{\langle I_X(t, \Delta t) I_Y(t + \tau, \Delta t)\rangle}{\langle I_X(t, \Delta t)\rangle \langle I_Y(t, \Delta t)\rangle}. \tag{2.19}$$

In this context, there are three important time variables to consider:

- **t**: The global time, representing the overall temporal evolution of the system. Variations with respect to this time can typically be averaged out across the ensemble, as they tend to be much faster than the exposure time.
- Δt: The interferometric delay, which is a key parameter in Time-of-Flight (ToF) measurements and is the primary variable of interest when determining optical path differences.
- τ: The relative time delay between two intensity measurements in the $g^{(2)}$. This parameter is crucial for analysing the decorrelation time, helping us assess how long the intensities remain correlated before decoherence effects take over.

Initially, the primary focus is on the degree of correlation for a specific interferometer delay. We can simplify our analysis by assuming we have the ideal case where the system immediately decorrelates to a value of 1 [15], as illustrated in Fig. 2.6(b) and discussed in Section 2.2.

Therefore, we only need to examine the correlation at the point where $\tau = 0$, allowing us to measure the maximum correlation directly without the need to evaluate the entire decorrelation curve.

There are two approaches to measuring second-order correlations in an interferometer. One can either measure the auto-correlation of the intensity at a single port or the cross-correlation between the intensities at two different ports. For cross-correlation, using the intensities from both ports A and B, and assuming $\langle I_i(t_i)\rangle = I_0$, we obtain:

$$g^{(2)}_{AB}(\Delta t) = \frac{I_0^2\langle 1 - |g^{(1)}_{(\Delta t)}|^2 \sin^2(\omega\Delta t - \Delta\varphi)\rangle}{I_0^2}. \tag{2.20}$$

For the auto-correlation, using the intensity at only one port, the second-order correlation function becomes:

$$g^{(2)}_{AA/BB}(\Delta t) = \frac{I_0^2\langle 1 + 2|g^{(1)}_{(\Delta t)}| \sin(\omega\Delta t - \Delta\varphi) + |g^{(1)}_{(\Delta t)}|^2 \sin^2(\omega\Delta t - \Delta\varphi)\rangle}{I_0^2} \tag{2.21}$$

With a completely stable phase between the two arms, oscillatory terms appear in the $g^{(2)}$ as illustrated in Fig. 2.3(c). However, for a varying phase over time t across the entire angular range $(0, 2\pi)$, the expectation values of the terms simplify as $\langle \sin(x)\rangle = 0$ and $\langle \sin^2(x)\rangle = 0.5$. This gives the final expressions:

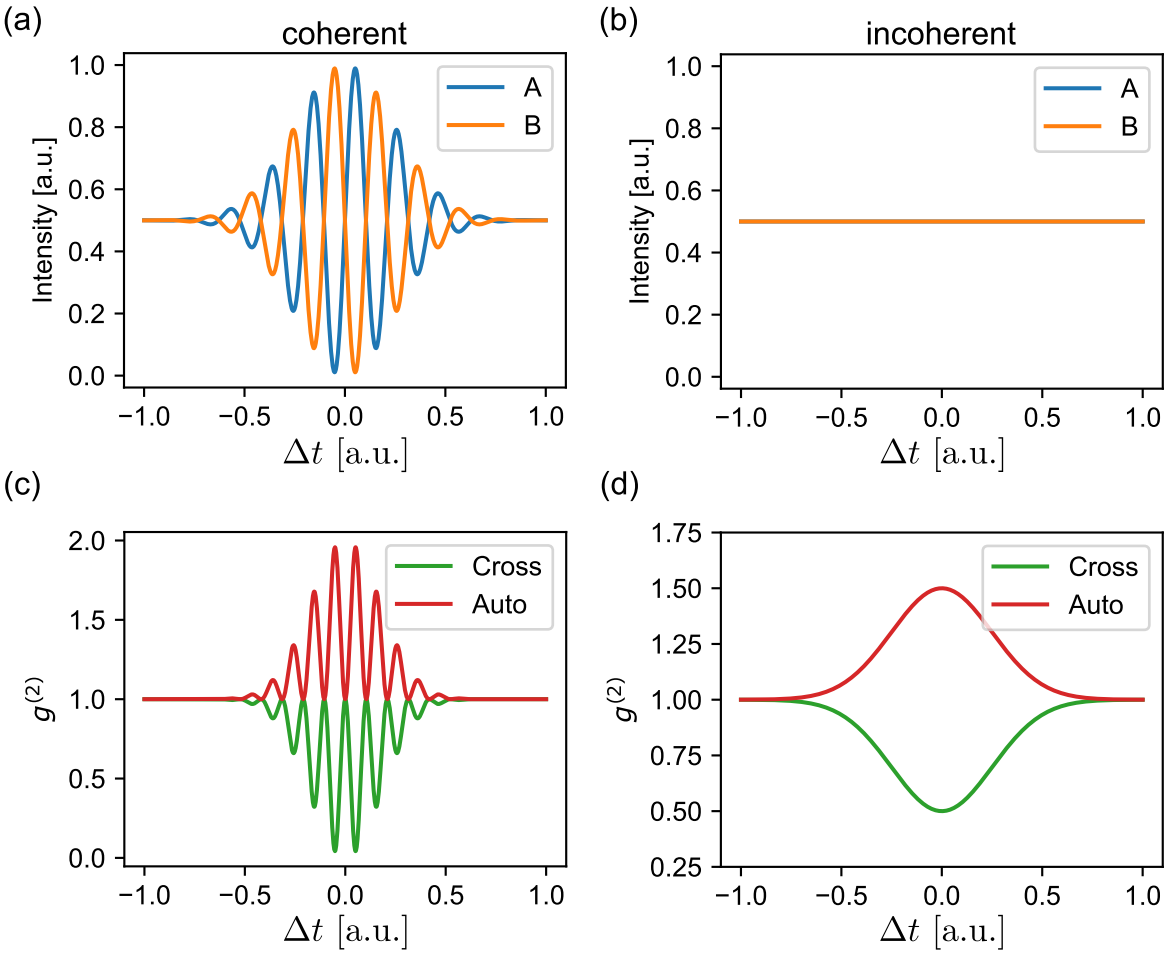

Figure 2.3: **Single Wavelength Second-Order Correlation:** The $g^{(1)}$ intensity interferogram and the corresponding $g^{(2)}$ correlation function. (a) The ideal interferogram measured at ports A and B, with a coherence length l_{coh}. Ports A and B exhibit opposite phases. (b) The interferogram acquired in the presence of large phase noise (c) The calculated $g^{(2)}$ when there is no phase noise; remnants of the first-order coherence fringes are still present. (d) In the presence of large phase noise, the envelope function remains in the $g^{(2)}$ curve. The units are arbitrary and meant to showcase the different imaging modalities without conveying specific measurement values. The figures were created using $\tau_{coh} = 0.5$ a.u. and a frequency of 30 a.u. .

$$g^{(2)}_{AB}(\Delta t) = 1 - \frac{|g^{(1)}_{(\Delta t)}|^2}{2}, \qquad g^{(2)}_{AA/BB}(\Delta t) = 1 + \frac{|g^{(1)}_{(\Delta t)}|^2}{2}. \tag{2.22}$$

This result indicates that we observe a smooth dip (anti-bunching) or peak (bunching) in the $g^{(2)}$ correlation function (see Fig. 2.3(d)). hen the two paths have zero delay ($\Delta t = 0$), the correlation is maximal, and as the delay increases, the correlation decreases, following a

Gaussian profile, eventually approaching 1, depending on the mutual coherence length of the two fields. The maximum visibility of 50 % arises from the use of classical fields; in a quantum framework, this visibility can be significantly higher [4]. The degree of visibility is directly dependent on the first-order coherence, $g^{(1)}_{(\Delta t)}$, which varies from 0 for incoherent fields to 1 for fully coherent fields. In this specific case of equal intensities in both arms the visibility of the resulting interference pattern is related to the absolute value of the first-order coherence $|g^{(1)}|$.

Multi-Spectral Interferometry

Up to this point, we have discussed the scenario, where a field with a single wavelength band of non-zero bandwidth field enters the interferometer and is split into two, resulting in matched frequencies in both arms of the interferometer. Now, we extend this analysis to the case where two distinct fields, each with a different frequency, enter the interferometer. This situation leads to multiple frequencies propagating through both arms, resulting in more complex interference dynamics. Instead of dealing with just two fields, we now have four fields inside the interferometer, two associated with each input.

Continuing with the same argumentation from the previous section, at the output ports A and B, the electric fields can be described as follows:

$$\begin{aligned} E_A(t_1, t_2, t) &= \frac{1}{\sqrt{4}} \left[E_{\omega_1}(t - t_1) + jE_{\omega_2}(t - t_2) + E_{\omega_3}(t - t_1) + jE_{\omega_4}(t - t_2) \right], \\ E_B(t_1, t_2, t) &= \frac{1}{\sqrt{4}} \left[E_{\omega_2}(t - t_2) + jE_{\omega_1}(t - t_1) + E_{\omega_4}(t - t_2) + jE_{\omega_3}(t - t_1) \right], \end{aligned} \tag{2.23}$$

Here, each $E_{\omega_i}(t)$ represents the electric field associated with a specific frequency ω_i. These fields correspond to the different input frequencies after passing through the interferometer. The two paths (t_1 and t_2) represent the travel times through the respective arms.

In this scenario, two approaches exist for computing the second-order correlation function $g^{(2)}$, that will depend on the experimental configuration and wavelength separation of the two bands.

Measurement through Bandpass Filtering: One approach focuses on measuring the second-order correlation by filtering the frequencies ω_1 at port A and ω_2 at port B. This method allows for the direct assessment of the correlation between the two input fields at separate output ports. By isolating these specific frequencies, we can gain insights into their individual contributions

to the overall correlation.

Cross-Detection of Input Fields: Alternatively, we can detect both ω_1 and ω_2 at both ports A and B. This setup enables us to explore cross terms between the two input fields, by calculating the $g^{(2)}$ from a single port. Such an approach offers a more integrated view of the relationship between the input fields and their collective behaviour at the output.

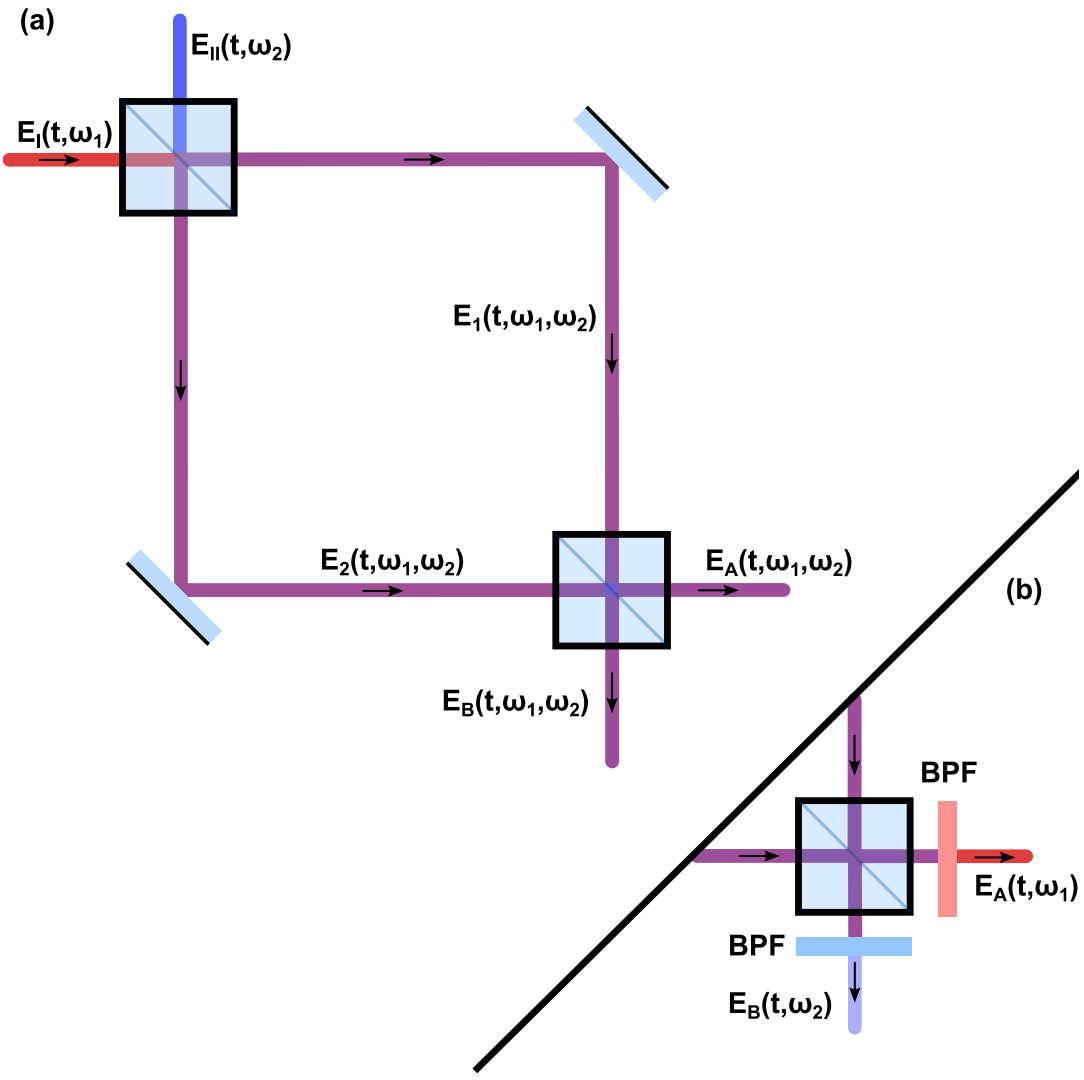

Figure 2.4: **Dual Wavelength Mach-Zehnder Interferometer:** Schematic of the electric fields in a Mach-Zehnder interferometer with two inputs at the first beamsplitter. The two input fields, $E_I(t,\omega_1)$ and $E_{II}(t,\omega_2)$, are each split into two paths, $E_1(t,\omega_1,\omega_2)$ and $E_2(t,\omega_1,\omega_2)$, which are then recombined at the exit beamsplitter. In case (a), both exit ports contain a combination of the two wavelengths, resulting in interference fringes and a beating pattern. In case (b), input I interferes at Port A and input II interferes at Port B, producing individual interference fringes for each wavelength.

Measurement through Bandpass Filtering (ω_1 & ω_2)

For the case of filtering specific frequencies at each port, the intensities at the output ports A and B are given by the following equations using Eq. (2.10):

$$\begin{aligned} I_A(\Delta t) &= |E_0|^2 \left(1 + |g^{(1)}_{(\Delta t,I)}| \sin\left(\omega_I \Delta t - \Delta\varphi\right)\right), \\ I_B(\Delta t) &= |E_0|^2 \left(1 - |g^{(1)}_{(\Delta t,II)}| \sin\left(\omega_{II} \Delta t - \Delta\varphi\right)\right), \end{aligned} \tag{2.24}$$

where ω_I and ω_{II} are the respective frequencies of the input fields, and $g^{(1)}$ represents the first-order coherence function.

Using the intensity correlation function Eq. (2.18) to calculate the second-order auto-correlation for one port, we obtain:

$$g^{(2)}_{AA/BB}(\Delta t) = 1 + \frac{|g^{(1)}_{(\Delta t)}|^2}{2}. \tag{2.25}$$

This leads to a peak in the second-order correlation function, similar to the single-field case. However, when performing a cross-correlation between the two output ports, the second-order correlation becomes:

$$g^{(2)}_{AB}(\Delta t) = \frac{I_0^2 \langle 1 - |g^{(1)}_{(\Delta t,I)}| \sin\left(\omega_I \Delta t - \Delta\varphi\right) |g^{(1)}_{(\Delta t,II)}| \sin\left(\omega_{II} \Delta t - \Delta\varphi\right)\rangle}{I_0^2}. \tag{2.26}$$

We can further simplify this expression using the trigonometric identity $\sin(x)\sin(y) = \frac{1}{2}[\cos(x-y) - \cos(x+y)]$, yielding:

$$g^{(2)}_{AB}(\Delta t) = \langle 1 - |g^{(1)}_{(\Delta t,I)}||g^{(1)}_{(\Delta t,II)}| \left[\cos\left(\Delta\omega\Delta t\right) - \cos\left((\omega_I + \omega_{II})\Delta t - 2\Delta\varphi\right)\right]\rangle. \tag{2.27}$$

The second cosine term averages out to zero due to the ensemble averaging process, leaving:

$$g^{(2)}_{AB}(\Delta t) = 1 - |g^{(1)}_{(\Delta t,I)}||g^{(1)}_{(\Delta t,II)}| \frac{\cos\left(\Delta\omega\Delta t\right)}{2}. \tag{2.28}$$

Thus, we observe an oscillating term that arises when cross-correlating the two filtered output fields of the interferometer with different input frequencies. However, in the auto-correlation scenario, we still recover the same result as for the single input field case.

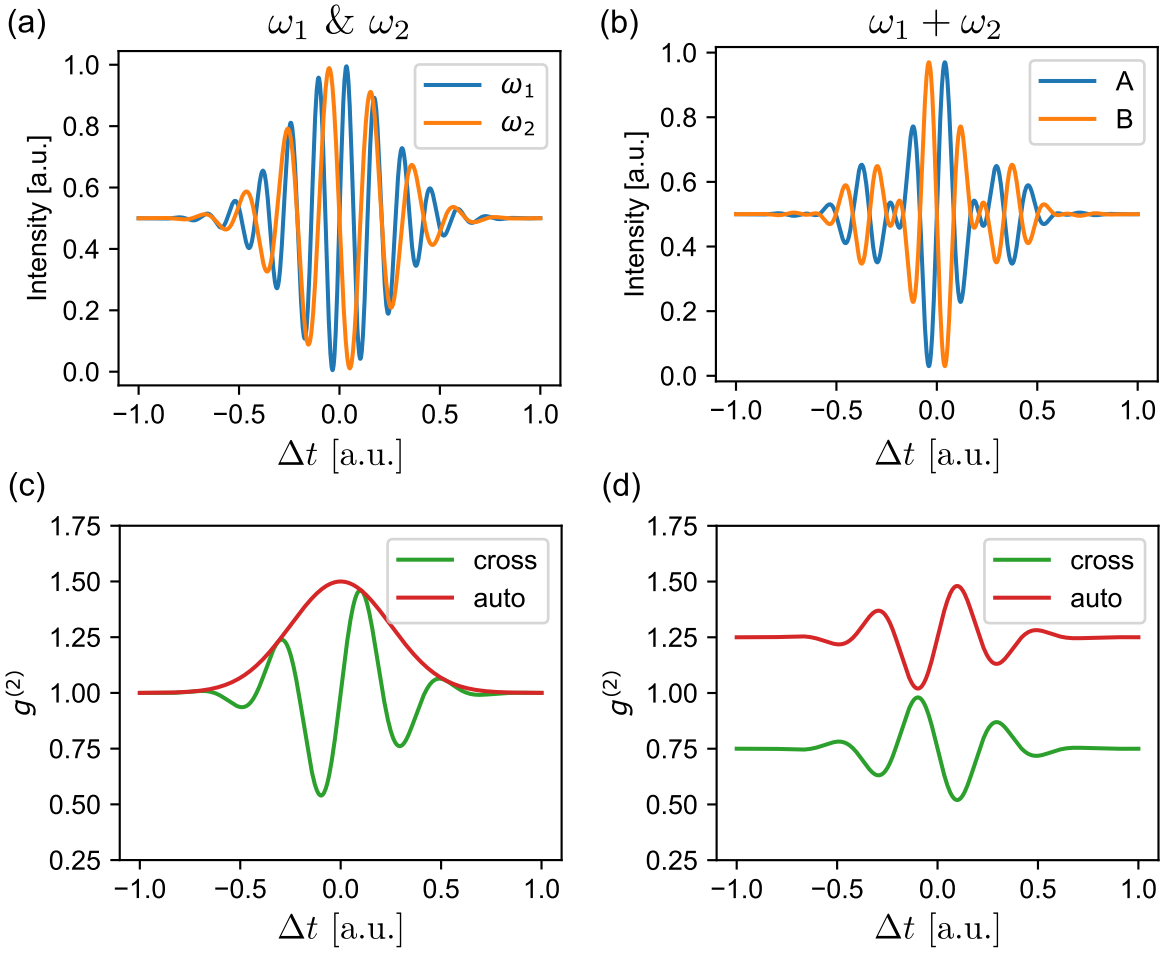

Figure 2.5: **Dual Wavelength Second-Order Correlation:** The $g^{(1)}$ intensity interferogram and corresponding $g^{(2)}$ correlation function for the case with two wavelength inputs, each filtered at the output. (a) The ideal interferogram measured for ω_1 and ω_2 with a common coherence length l_{coh}. (b) The interferograms acquired when we bulk detect both wavelength at port A and port B (c) The calculated $g^{(2)}$ when filtering each wavelength at one port. The auto-correlation shows the same result as for the single wavelength case. The cross-correlation then gives rise to the beating of the two wavelengths. (d) The calculated $g^{(2)}$ when bulk detecting both ω_1 & ω_2. The auto- and cross-correlation method show to have an offset and conjugate phase of the beating. The units are arbitrary and meant to showcase the different imaging modalities without conveying specific measurement values. The figures were created using wave packets with $\tau_{coh} = 0.5$ a.u. and a frequency of 30 a.u. and 45 a.u.

.

Cross-Detection of Input Fields ($\omega_1 + \omega_2$)

In this configuration, all input fields are present at both output ports, allowing for a comprehensive analysis of their interactions. The intensities at each port, derived from Eq. (2.10), are expressed as follows:

$$\begin{aligned} I_A &= \frac{I_0}{2}\left[2 - \sin\left(\omega_I \Delta t + \Delta\varphi\right) - \sin\left(\omega_{II}\Delta t + \Delta\varphi\right)\right], \\ I_B &= \frac{I_0}{2}\left[2 + \sin\left(\omega_I \Delta t + \Delta\varphi\right) + \sin\left(\omega_{II}\Delta t + \Delta\varphi\right)\right]. \end{aligned} \tag{2.29}$$

By substituting these intensity expressions into the second-order correlation function defined in Eq. (2.18), we obtain the correlation functions for the same port measurements:

$$g^{(2)}_{AA/BB} = I_0^2\left[1 + \frac{1}{8}|g^{(1)}_{(\Delta t,I)}|^2 + \frac{1}{8}|g^{(1)}_{(\Delta t,II)}|^2 + \frac{1}{4}|g^{(1)}_{(\Delta t,I)}||g^{(1)}_{(\Delta t,II)}|\cos(\Delta\omega\Delta t)\right]. \tag{2.30}$$

When cross-correlating the outputs from both ports, the correlation function takes the form:

$$g^{(2)}_{AB} = I_0^2\left[1 - \frac{1}{8}|g^{(1)}_{(\Delta t,I)}|^2 - \frac{1}{8}|g^{(1)}_{(\Delta t,II)}|^2 - \frac{1}{4}|g^{(1)}_{(\Delta t,I)}||g^{(1)}_{(\Delta t,II)}|\cos(\Delta\omega\Delta t)\right]. \tag{2.31}$$

In this scenario, the sinusoidal term also emerges, introducing an oscillatory behaviour in the correlation function. However, it is important to note that the visibility of this correlation is reduced compared to the filtered case. This reduction in visibility reflects the more complex interactions occurring when both input fields are detected simultaneously, as opposed to when individual fields are isolated at the output.

Correlation Time (τ)

Thus far, our focus has largely been on the correlation magnitude, specifically the degree of decorrelation, with the assumption that it converges to a value of 1. While we have considered the case of $\tau = 0$ as sufficient for our analysis, it is important to also take into account the full curve to enhance measurement accuracy in noisy environments. The second-order correlation function, $g^{(2)}$, typically demonstrates a bi-exponential decay, characterized by a distinct decorrelation time. This decorrelation time signifies the interval over which the correlation diminishes to half of

its maximum value, offering critical insights into the temporal dynamics of the system being studied. An ideal example of fluctuating intensity with a τ shifted copy and its corresponding decorrelation curve is shown in Fig. 2.6.

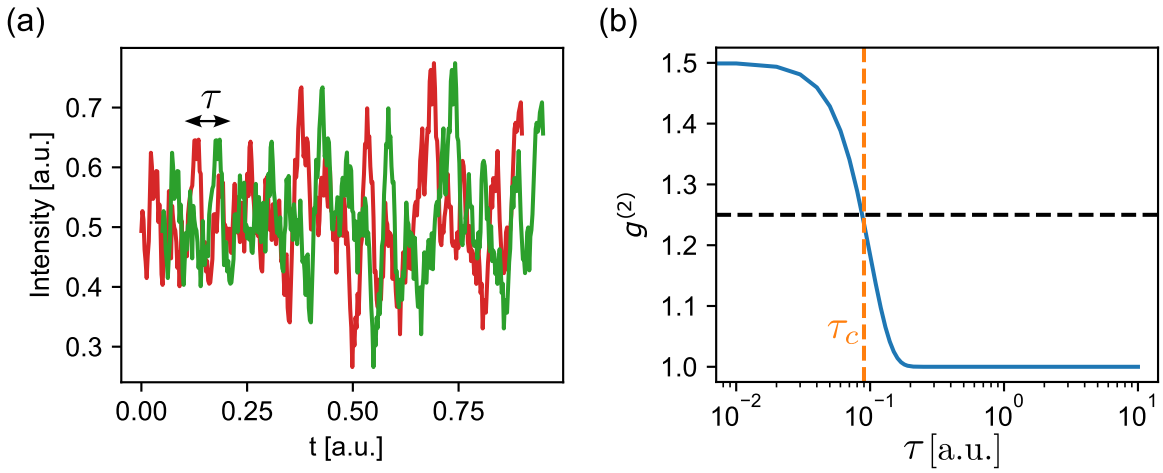

Figure 2.6: **Decorrelation Time:** (a) Intensity trace alongside a copy shifted by a temporal delay τ. (b) The full $g^{(2)}$ correlation curve calculated as a function of this temporal shift τ. The decorrelation time τ_c is the temporal shift where the correlation value drops to half of its initial peak. The units are arbitrary and meant to showcase the different imaging modalities without conveying specific measurement values.

One critical aspect is ensuring that our exposure time remains shorter than the decorrelation time; otherwise, this would result in a degradation of the maximum correlation value. In the intended applications, we have control over the required phase scrambling and can adjust the exposure time accordingly. In some fields, such as in Diffuse Correlation Spectroscopy (DCS) [15, 16], the decorrelation time itself is the primary quantity of interest. However, this concept is also useful in our case. For instance, when dealing with significant noise, $g^{(2)}(\tau > \tau_c) \neq 1$, the noise is often much slower than the phase fluctuations, whether controlled or uncontrolled. This implies that the noise decorrelates over a much longer timescale compared to the actual signal.

Therefore, it can be advantageous to normalize by the decorrelated value, as shown below:

$$\tilde{g}^{(2)}(\Delta t) = \frac{g^{(2)}(\Delta t, \tau = 0)}{g^{(2)}(\Delta t, \tau > \tau_c)} \tag{2.32}$$

This normalization helps eliminate any offset when the signal does not fully decorrelate to 1 or when there are slow decorrelation processes that persist, even in the absence of a signal (e.g., for large Δt).

2.4 Outlook

The concepts discussed in this chapter provide the foundation for the novel imaging techniques explored in the forthcoming chapters, which build on the fusion of classical interferometers and second-order (intensity) correlations. This very versatile approach, robust to phase noise, allows for detailed information extraction about the scene or sample being imaged and proves applicable across a range of imaging scenarios.

Chapter 3.

Time-of-Flight Widefield Microscopy

In this chapter, I apply the concepts introduced in the previous chapter to a ToF widefield microscopy technique using a thermalized light source. I demonstrate its robustness to phase noise, with no requirement for either spatial or temporal coherence, while achieving much higher resolution than conventional ToF techniques. Additionally, I demonstrate that the dual-wavelength approach achieves nanometric axial resolution in imaging, showcasing its effectiveness and rivalling state-of-the-art techniques in terms of axial resolution.

3.1 Literature Review: Depth Sensing Techniques

Depth imaging techniques in microscopy enable the detailed visualization and analysis of three-dimensional structures within specimens via optical sectioning. These methods provide information about complex biological processes, cellular architecture and tissue morphology, providing insights for scientific research and medical diagnostics. The axial resolution of optical imaging devices generally depends on two key factors: the wavelength of the light used and the numerical aperture of the imaging system.

Confocal microscopy is a popular and widely used technique for depth imaging [21]. This microscopy technique invented by Marvin Minsky [22] performs a point-by-point image construction by focusing a point of light and scanning it across a specimen and then collecting some of the returning rays. By illuminating a single point one can avoid most of the unwanted scattered light that obscures the image . A pinhole aperture will filter reflected light and hence only collect light within a very small volume of the specimen. Scanning in 3-D will allow to create a depth resolved micrograph. A sample schematics is given in Fig. 3.1(a). One of the major drawbacks is the limitation to acquisition speed due to the 3D point-by-point scanning. Secondly, due to the use of pinholes we will lose orders of magnitude of light intensities. When optimally used it gives high resolution diffraction limited depth images with resolutions down to 180 nm laterally and 500 nm axially [23, 24]. Recent advancements, such as 4Pi microscopy, have been developed to enhance resolution by utilizing interference between counter-propagating light waves, allowing for significantly improved axial resolution beyond the limits of conventional confocal microscopy. It has been shown to improve the lateral and axial resolution to 200 nm and 145 nm [25].

Interferometric methods introduce a distinct modality for depth imaging, enhancing higher-

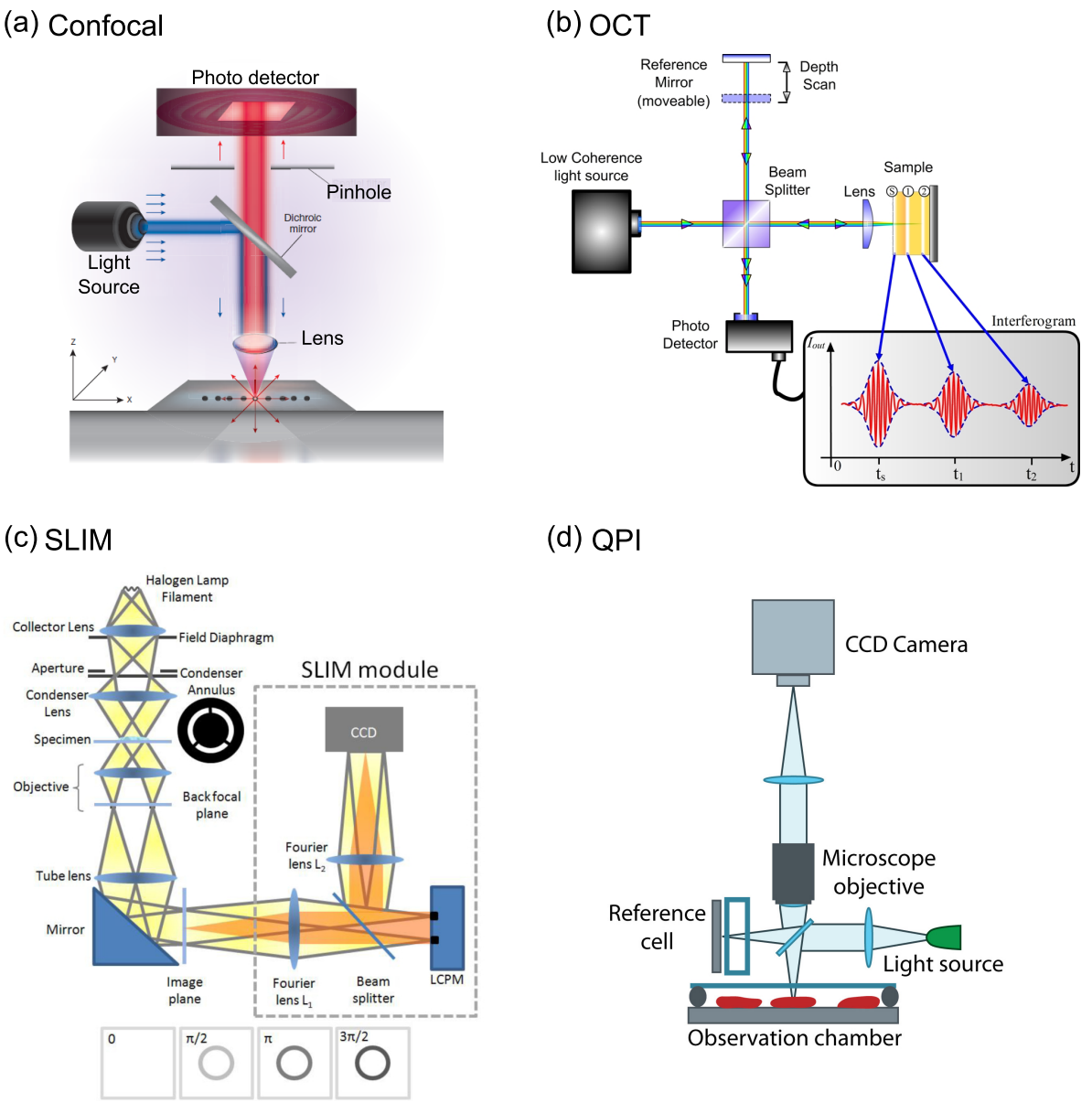

Figure 3.1: **Overview of Depth Sensing Techniques in Microscopy:** (a) Schematic of a confocal microscopy setup designed for fluorescence measurement. (b) Illustration of an OCT setup, where reflections from different layers of the sample are measured. (c) Overview of the SLIM technique, which uses a linear interferometer combined with a spatial light modulator (SLM). (d) Schematic overview of an example QPI setup. Figures adapted from [17, 18, 19, 20].

resolution imaging capabilities and enabling widefield applications. A prominent technique that employs interferometry is **Optical Coherence Tomography (OCT)** [26]. It measures reflected light from different layers within a sample interfered with a reference beam, as depicted in Fig. 3.1(b). This technique employs a short-coherence, broad-spectrum light source to capture micrometer-resolution images, with diverse medical applications. It is particularly critical in ophthalmology for diagnosing and monitoring retinal diseases and glaucoma, and extends to

fields like cardiology and dermatology. The lateral resolution of OCT is diffraction limited [27] and the axial resolution ranges from $1 - 10\mu m$ [28] depending on the quality of the instruments. Advances such as Spectral-Domain OCT and Swept-Source OCT [29, 30, 31, 32] have further enhanced its resolution and imaging speed, making OCT a valuable tool in both clinical practice and research. However, its reliance on coherence makes it susceptible to phase noise and requires mechanical phase stability as compared to the confocal technique.

Other phase sensitive methods such as **Digital Holographic Microscopy (DHM)** [33] or **Quantitative Phase Imaging (QPI)** [34] where phase-sensitive interference patterns are analysed, have a much higher axial resolution [35]. As it can detect subtle variations in phase that correspond to nanometric changes in the sample. A schematic of a common setup is given in Fig. 3.1(d). While DHM and similar holographic methods are powerful, they are not without challenges. These techniques rely on coherence but do not strictly require long coherence lengths, as partially coherent light can still produce usable interference patterns. However, phase noise and interferometer instability can impact the accuracy of phase retrieval, particularly in dynamic environments or when working with low-contrast samples. Holographic methods that eliminate the need for mechanical phase stability between the reference and sample arms often rely on common-path interferometry. One of the most widely used techniques is Zernike's **Phase-Contrast Microscope (PCM)** [36]. In PCM, background light is separated from light passing through the sample, with the background light being attenuated and 90 deg phase-shifted. This modified background light then interferes with the light passing through the sample, resulting in an image with constructive interference where the sample interacts with the light and destructive interference in the background. This process enhances contrast, visualizing topological features at the nanometre scale. However, a drawback of PCM is the presence of a halo effect around the sample, which can obscure fine details. Additionally, a simple PCM can only qualitatively measure depth. For quantitative measurements, it must be combined with other techniques, such as in **Spatial Light Interference Microscopy (SLIM)** [19], where PCM is integrated with Gabor's holography by incorporating a Spatial Light Modulator (SLM) into the experiment for measuring thin samples in transmission. The SLM provides multiple phase shifts of the background light, enabling the full recovery of the accurate depth of the sample, as shown in Fig. 3.1(c). SLIM and other developments have combined PCM with additional tools to quantify depth, achieving state-of-the-art axial resolutions down to sub-nanometres [19, 37, 38]. While these methods maintain mechanical phase stability, they still depend on coherence and are therefore less suitable for samples that are moving or vibrating during the acquisition time with displacements exceeding a pixel pitch within the exposure time (tens of ms), or for measuring fluorescence.

ToF sensing for Light Detection and Ranging (LiDAR) is a class of depth measurement techniques that definitely do not require coherence. ToF techniques measure the distance between a sensor and an object by measuring the time elapsed between the emission of a pulse or photon and its detection by the sensor. By scanning a point-like light source and a single pixel detector

or by using flood-illumination and a camera, ToF enables the creation of highly detailed, three-dimensional representations of objects and environments. The most sensitive Time-of-Flight (ToF) imaging methods are usually deployed with single-photon detectors such as Single Photon Avalanche Diodes (SPADs) and a Time-Correlated Single Photon Counting (TCSPC) module for determining the arrival time of the return photons through TCSPC [39, 40, 41]. The primary physical parameter being assessed is the group delay (determined by the group velocity of light), rather than the phase delay (linked to the phase velocity). Therefore, unlike phase-imaging techniques, ToF is incoherent and more robust to vibrations and perturbations. Yet, they suffer from restricted resolution attributable to electronic timing jitter, resulting in depth or distance estimation uncertainties on the order of 0.1-1 mm [42]. Therefore, they are not typically considered to be suitable for microscopy.

It is possible to retain the benefits of incoherent measurements while still achieving micron-scale resolution suitable for microscopy. One such technique known from quantum optics, **Hong-Ou-Mandel (HOM)** interference [43], was first demonstrated by Hong, Ou, and Mandel in 1987. It occurs when two identical photons are incident at the two input ports of a 50:50 Beam-Splitter (BS). The photons must be identical or indistinguishable in all degrees of freedom (wavelength, polarization, space, and time). Only when they are perfectly identical will they bunch together and exit through the same output port of the BS. This photon bunching leads to a dip in the photon coincidence measurement, which can be leveraged for sensing applications. HOM interference finds applications in quantum information processing and sensing, particularly in precise time-delay measurements [44, 45]. This technique relies on single-photon detectors and is entirely insensitive to phase. Additionally, researchers have demonstrated that resolution can be further enhanced using a dual-wavelength approach [46]. Instead of a single photon, a frequency-entangled photon pair source is used with a large frequency separation. This setup introduces a beating in the coincidence measurement, which can be exploited for even more precise time-delay measurements. This behaviour, as illustrated in Fig. 2.3 and Fig. 2.5, is analogous to the response observed with classical fields, which exhibit the same pattern. The wavelength of this beating will be determined by the frequency difference between the two photons pairs. While these quantum methods offer high robustness, they typically rely on the use of correlated and indistinguishable photon pairs [47].

A classical analog to quantum $g^{(2)}$ imaging can be created using pseudo-thermal light to measure intensity correlations in images, rather than relying on single-photon detection. This technique, known as **intensity correlation imaging**, has been successfully demonstrated in point-scanning reflection configurations [48]. While similar approaches have been explored in prior studies [49, 50], these typically focus on spatial correlations by measuring the relationship between different pixels, requiring spatial coherence for a fixed phase relationship.

3.2 Methodology

Our method relies on temporal intensity correlations from a thermal source measured at a single pixel, allowing us to bypass the need for both spatial and temporal coherence required in the methods discussed in the previous chapter. Additionally, it overcomes the limitations of ToF techniques imposed by the slow Instrument Response Function (IRF) of the TCSPC by extracting ToF information from intensity correlations in an interferometer. This section details the methodology for the ToF microscopy technique, along with the associated requirements and processing methods. We begin with the single-wavelength approach and then progress to the dual-wavelength setup, which enhances depth imaging precision. This approach offers significant potential for high axial resolution, nanoscale imaging across various applications.

Single Wavelength

The experimental setup used in this study is based on a Mach-Zehnder (MZ) interferometer, as shown in Fig. 3.2. The sample is imaged in transmission, allowing for optical thickness measurements of translucent samples. The choice of light source is flexible, though we ultimately opted for a broadband super-continuum laser (Fianium SuperK). The advantage of this light source is the ability to select different wavelengths and bandwidths (coherence lengths) simply by swapping different filters at the input or output of the interferometer. In the Mach-Zehnder (MZ) interferometer light is split into two arms: the sample and reference arm. In the sample arm, the transmitted light is collected using either a 40x or 20x microscope objective, depending on the required magnification. Both objectives require the same 200 mm tube lens, making it easy to swap them as needed.

For imaging, two different detector technologies were employed: a low-pixel count, high-speed SPAD camera (MPD SPAD array, 64x32 pixels, 100 kfps) and a high-pixel count, low-cost CMOS camera (Basler ace acA720-520um, 720x540 pixels, up to 525 fps). The SPAD camera was chosen for its short acquisition times, while the CMOS camera provided higher spatial resolution at a lower cost. In the reference arm, we included a motorized translation stage (Thorlabs PT1/M-Z9, 25 mm range) to scan the optical delay between the two arms.

As previously discussed in Section 2.3, $g^{(2)}$ imaging requires a phase-randomized or thermalized source to eliminate coherent interference fringes with classical light sources. To achieve this, two options are considered: (1) using a rotating diffuser to introduce a constantly changing speckle pattern, or (2) using a piezo stage to induce spatially invariant phase fluctuations. One important distinction is that the rotating diffuser randomizes both the phase and the intensity,

which could degrade the measurement due to the connection of the interferometer intensity balance and the visibility. Furthermore, it produces a non-uniform averaged wavefront, which can complicate measurements of small, precise thicknesses, if not properly characterized. Thus, for high-precision measurements, the piezo stage is preferred. It provides better control over the phase randomization process while still maintaining a flat wavefront on average.

The data acquisition process follows from the requirements of calculating the expectation value or ensemble average of intensities, as outlined in the $g^{(2)}$ equation Eq. (2.18). This necessitates measuring a large number of intensity images with random phases. The procedure for gathering information about the optical thicknesses (material thickness $\times$ refractive index) of the sample involves scanning the optical delay across the 0-delay overlap in the interferometer. At each delay position, hundreds of frames are captured while phase scrambling is applied. The

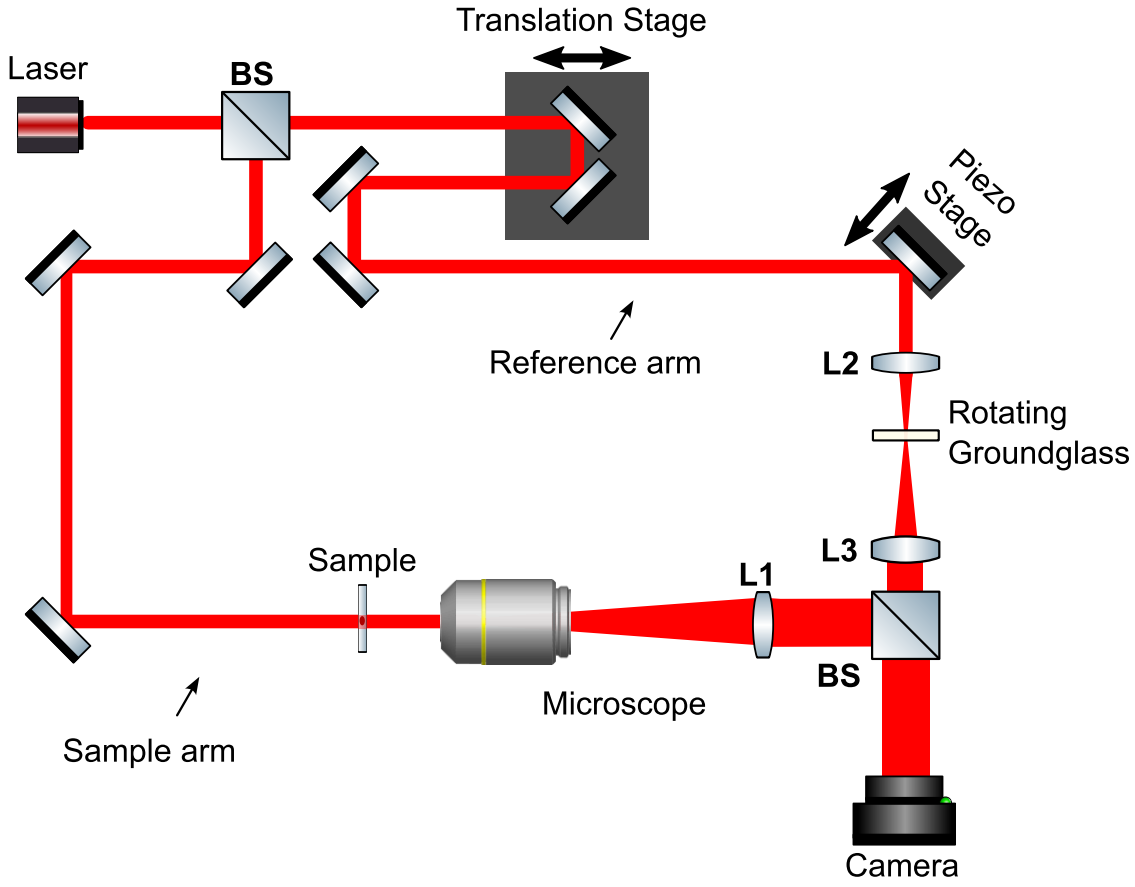

Figure 3.2: **Single Wavelength $g^{(2)}$ Microscopy:** Schematic of the experimental setup. A single output is used to measure the autocorrelation function $g^{(2)}$. For scrambling, either a rotating ground glass diffuser or a piezo stage can be employed. BS: Beamsplitter, L1: 100 mm, L2: 50 mm, L3: 150 mm.

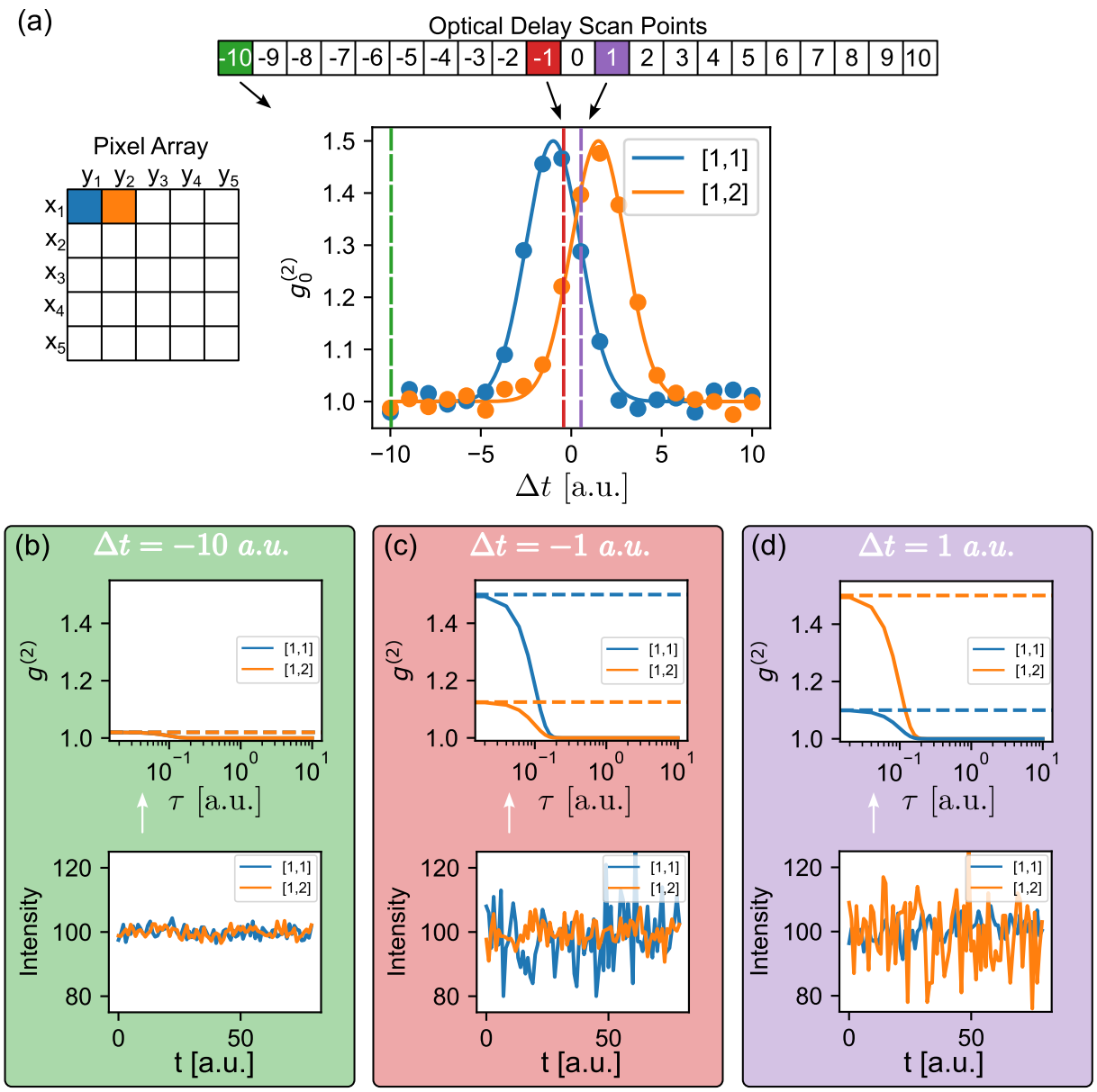

Figure 3.3: **ToF Measurement Procedure:** Demonstration of Time-of-Flight (ToF) difference measurement between two pixels, [1,1] (blue) and [1,2] (orange). We show how you go from (a) Shows the intensity traces from both pixels, with three specific optical delay positions highlighted in green, red, and purple. (b)-(d) Display the corresponding $g^{(2)}$ correlation functions as a function of computational temporal shift τ, along with the respective time traces for each interferometer optical delay position.

exposure time for each frame must be short enough to ensure that the phase shift remains negligible during the exposure of a single frame. Consequently, each frame will exhibit a different random phase due to variations between exposures. To mitigate any phase noise, we can minimize the exposure time and acquire additional frames if necessary. For each optical delay we repeat this process. The intensity as a function of acquisition time is measured for each pixel,

and the second-order correlation function is computed. The $g^{(2)}$ value at zero delay, or the decorrelation magnitude, serves as the primary value for each scan point and pixel. By analysing how this value changes with optical delay, a Gaussian peak is observed. The width of this peak is determined by the laser light's bandwidth, with a higher bandwidth resulting in a narrower peak and, thus, higher depth resolution. For our laser light bandwidth which using 10 nm bandpass filter is 28.6 μm using equation Eq. (2.4). A Gaussian fit is then applied to extract the peak centre, where the relative shift of this centre corresponds to the optical path length of a sample at that pixel. Repeating this process across all pixels generates a depth map of the sample. A schematic of the process routine is given in Fig. 3.3.

Dual Wavelength

The accuracy of Time-of-Flight (ToF) measurements, particularly the precision with which the $g^{(2)}$ peak position is determined is directly dictating the achievable axial resolution of the imaging system. In the single-wavelength experiments, the width of the $g^{(2)}$ curve is determined by the coherence length of the light source, which is inversely proportional to its bandwidth as described in Eq. (2.3). For higher resolution, it's essential to use a broadband source. Moreover, exploring the spectral domain has shown to offer enhanced resolution in various studies [29, 51, 52].

In addition to broadening the bandwidth, resolution can alternatively be increased by introducing a second wavelength band. This similarly expands the spectral domain, although it does not need to provide the full spectrum between the two bands. As discussed in Section 2.3, the addition of a second band creates a beating at a synthetic wavelength (Λ) in the second-order correlation function, in contrast to the traditional beat note observed in coherent interferometry. In coherent interferometry, the two bands interfere and produce a beating in time t [53]. This synthetic wavelength, shown in Fig. 2.5(d), arises from the interaction between the two wavelengths in both arms of the interferometer within the $g^{(2)}$ measurement and create a beating with interferometer delay Δt. This fast beating allows for high precision depth measurements without being affected by the phase instabilities that typically impact standard interferometric techniques. For example, using $\lambda_1 = 405$ nm and $\lambda_2 = 980$ nm, the generated Λ is approximately 690 nm and is calculated by:

$$\Lambda = \frac{\lambda_1 \lambda_2}{|\lambda_1 - \lambda_2|} \tag{3.1}$$

To extract the ToF information, we scan the delay stage to measure the $g^{(2)}(0)$ value across 25 optical delay points, acquiring several hundred intensity images at each step. As illustrated in Fig. 3.4, dispersion is compensated for by incorporating identical optics in both arms and then aligning the images on two detection cameras, ensuring that both wavelengths travel along

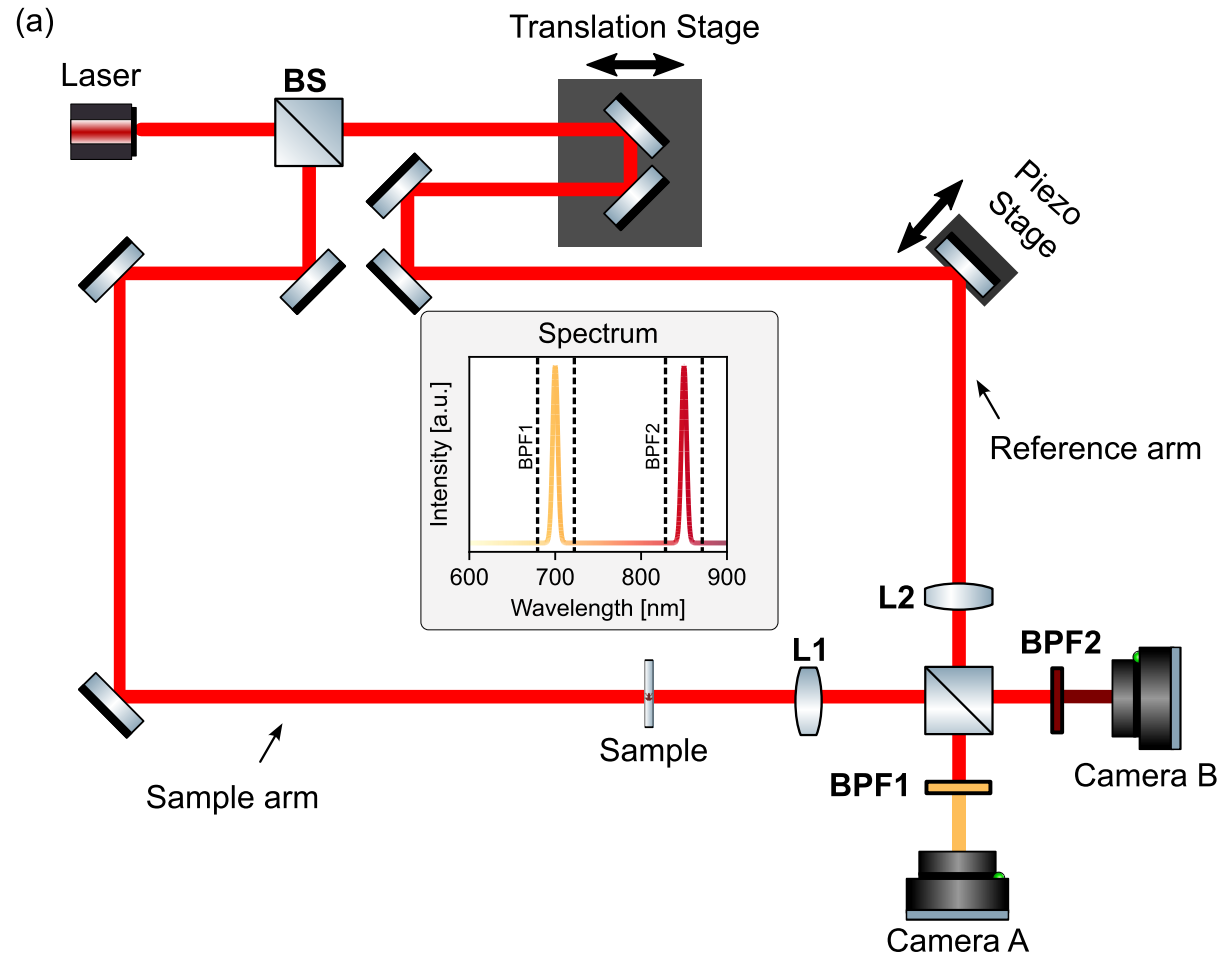

Figure 3.4: **Dual Wavelength $g^{(2)}$ Microscopy:** (a) Schematic of the experimental setup. We measure each wavelength at the respective port by filtering with bandpass filters. BS: Beamsplitter, BPF: Bandpass Filter, L1: 100 mm, L2: 50 mm, L3: 150 mm. (b) The laser spectrum, showing two distinct wavelength bands with specific bandwidths

identical optical paths. A random central pixel is selected, and the temporal shift (or phase shift of the synthetic wave) is determined for all other pixels. This method is highly effective for measuring small features, improving sensitivity. Notably, the data collected from the dual-wavelength measurements can also be used to perform a single-wavelength analysis, offering added flexibility and robustness. Hence to handle ambiguities introduced by phase wrapping (i.e., ToF differences larger than $\Lambda/2$), a combined single and dual-wavelength approach is employed.

Fisher Information Analysis

To evaluate the sensitivity of our method, we conduct a basic Fisher information analysis, given in Fig. 3.5. Given that we measure intensities at the output of the interferometer, the noise distribution follows Poisson statistics at each detector when the system is shot-noise limited. However, at classical light levels, the Poisson distribution converges to a Gaussian distribution as the photon number increases. For simplicity, we restrict our Fisher information analysis to the autocorrelation case, where we consider the square of an intensity that's normal distributed. This necessitates determining the Probability Density Function (PDF) of $Y = X^2$, where $X \sim \mathcal{N}(\mu, \sigma^2)$. Here $\mathcal{N}$ denotes a normal distribution, with μ representing the mean and the σ the standard deviation.

The square of a normally distributed variable follows a chi-squared distribution [54, 55]. More precisely, since $\mu \neq 0$, the resulting distribution is non-central chi-squared with one degree of freedom. Consequently, the distribution is given by:

$$X^2 = \sigma^2 \chi_1^2 \left(\gamma = \left(\frac{\mu}{\sigma} \right)^2 \right), \tag{3.2}$$

where the non-central chi-squared distribution, denoted as $\chi_k^2(\gamma)$, has a PDF defined as:

$$\chi^2(x, k, \gamma) = \frac{1}{2} \exp\left(-\frac{\gamma + x}{2} \right) \left(\frac{x}{\gamma} \right)^{(k-2)/4} I_{(k-2)/2} \left(\sqrt{\gamma x} \right), \tag{3.3}$$

with I_ν representing the modified Bessel function of first order of degree ν.

The $g^{(2)}$-function, as defined in Eq. (2.18), is normalized by the mean expectation value squared. This leads to the following expression:

$$\frac{\tilde{X}^2}{\mu^2} = \frac{\sigma^2}{\mu^2} \chi_1^2 \left(\gamma = \left(\frac{\mu}{\sigma} \right)^2 \right). \tag{3.4}$$

To simplify our analysis, we empirically estimate the distribution parameter γ from the data, which fluctuates across measurements but typically hovers around $\gamma \approx 0.02$. Rather than focusing on the absolute value of the Fisher Information (FI), our main goal is to compare how FI varies between different measurement modalities. This approach allows us to fix γ and focus on the relative changes in sensitivity across different setups.

We compare the following measurement scenarios: (a) a single central wavelength at 800 nm

with a bandwidth of 10 nm; (b) a single central wavelength at 800 nm with a bandwidth of 200 nm; and (c) two distinct wavelength bands centred at 700 nm and 900 nm, each with a bandwidth of 10 nm. For the simulations, we assumed the derived $g^{(2)}$-functions from Section 2.3, with the coherence length l_c calculated assuming a Gaussian-distributed spectrum.

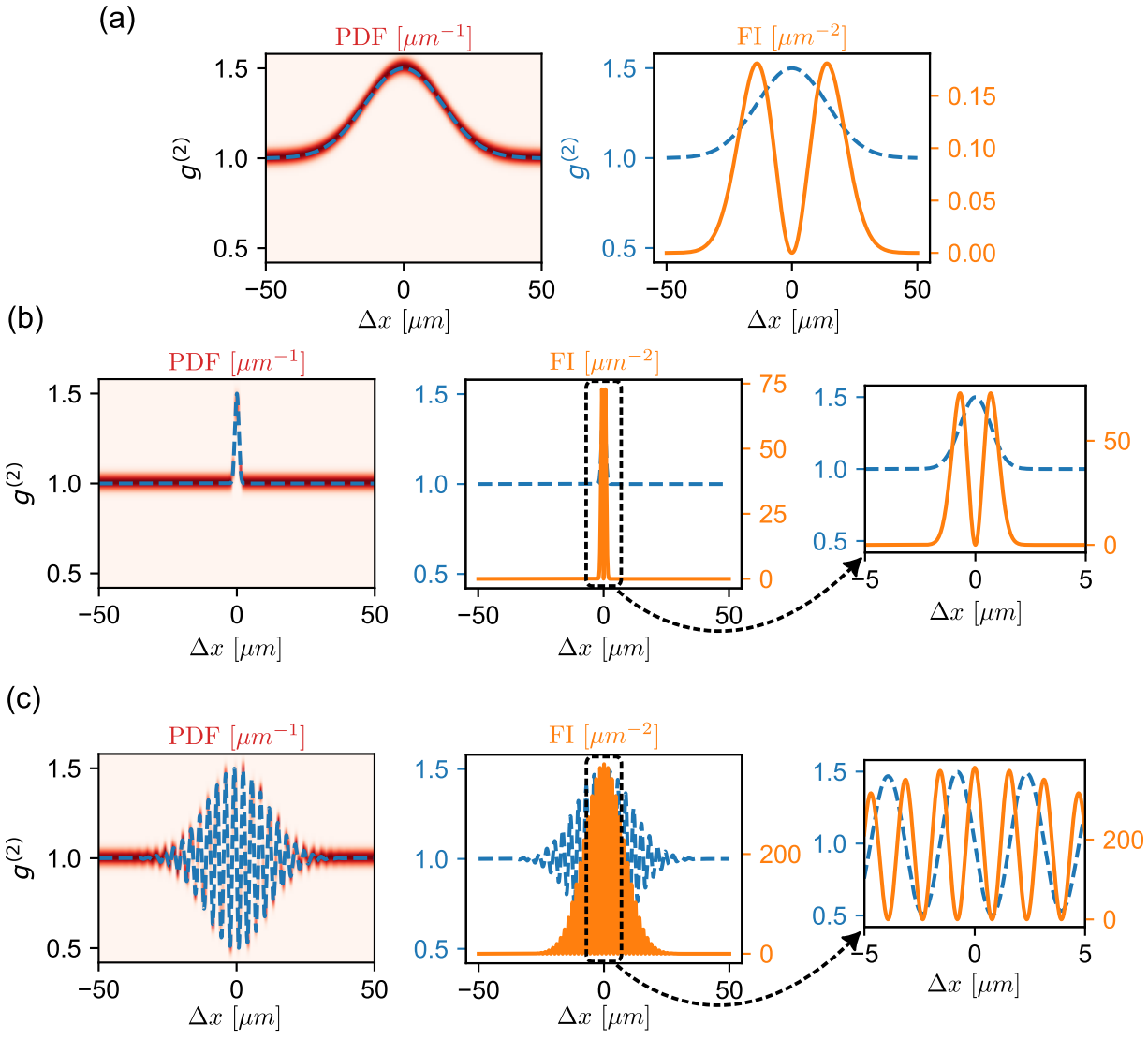

Figure 3.5: **Fisher Information Analysis:** This figure presents the FI analysis for three distinct cases: (a) Single wavelength with narrow bandwidth (800 nm ± 5 nm); (b) Single wavelength with large bandwidth (800 nm ± 100 nm); (c) Dual wavelength with 700 nm ± 5 nm and 900 nm ± 5 nm. The leftmost plots display the PDF map in red and the $g^{(2)}$ function in dotted blue. The second plot from the left shows the FI in orange on the right sided y-axis, overlaid with the $g^{(2)}$ function.

The Fisher information was computed using the simplified formula:

$$I_{\text{Fisher}} = \int \left(\frac{\partial}{\partial \theta} \ln(f(x,\theta)) \right)^2 f(x,\theta)\, dx, \tag{3.5}$$

where θ represents the expected $g^{(2)}$-value, and $f(x, \theta)$ is the PDF. For each optical delay position, the expected $g^{(2)}$-value was used to generate the corresponding PDF, and FI was then calculated for each scan position.

The results, illustrated in Fig. 3.5, indicate that the maximum FI is located at the points of maximum gradient, which is expected. For case (a), we observe two peaks in the FI with a maximum value of 0.018. In case (b), where the bandwidth is increased, the sensitivity improves as the peaks narrow, leading to steeper gradients. This results in a maximum FI of 70 at the slopes. Interestingly, in case (c), where two distinct wavelength bands are used, we observe a significant increase in FI compared to the continuous spectrum case, with a maximum value of 300—a roughly threefold increase in FI. Moreover, in case (c), we see multiple peaks due to the beating between the two wavelengths, leading to a much higher cumulative Fisher information over the entire scan compared to case (b).

This analysis demonstrates that broadening the spectrum increases sensitivity and resolution, with the FI analysis highlighting the advantages of the dual-wavelength approach over a continuous spectrum.

Signal-to-Noise Ratio

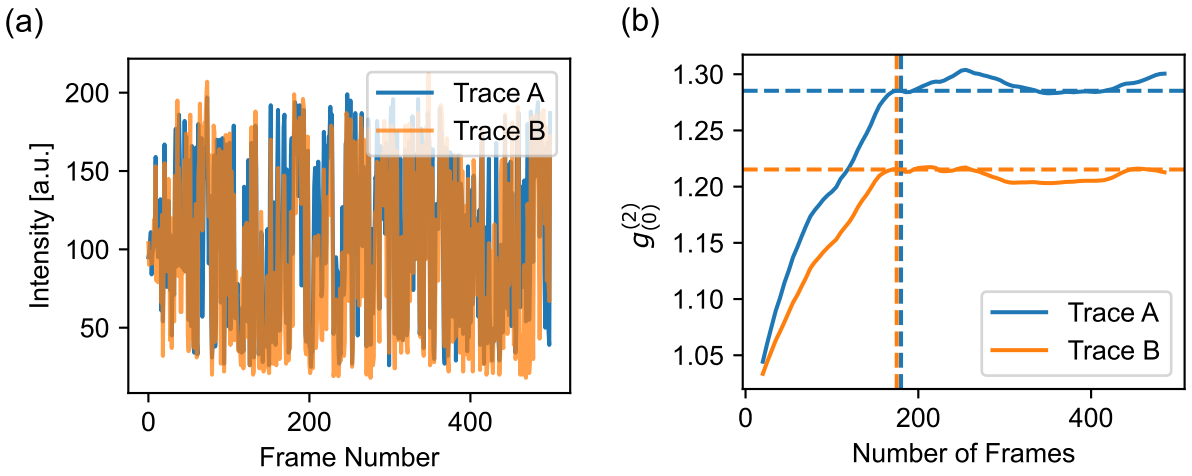

Figure 3.6: **SNR Analysis:** (a) Sample time traces for two different maximum correlations, $g_0^{(2)} = 1.22$ (blue) and $g_0^{(2)} = 1.3$ (green). (b) Plot of $g_0^{(2)}$ as a function of the number of frames used in the correlation calculations.

As observed in the FI analysis, the sensitivity of the measurement is directly related to the maximum $g^{(2)}$ value or visibility. One critical aspect to examine is how the number of frames influences the maximum $g^{(2)}$ value. We want to determine if increasing the number of frames would lead to higher $g^{(2)}$ values, or if there is a point where the measurement stabilizes, indicating

no further benefit from additional frames.

To investigate this, we analysed two points in our measurement with different maximum $g^{(2)}$ values. The results, shown in Fig. 3.6, reveal that while the $g^{(2)}$ value increases with the number of frames, it plateaus after approximately 200 frames. Interestingly, both curves, despite starting with different maximum values, exhibit the same behaviour, suggesting that a systematic error or noise is present, rather than statistical error. If the limiting factor were purely statistical, we would expect the signal to enhance and the $g^{(2)}$ to increase continuously with more frames. However, the plateau indicates that after around 200 frames, further sensitivity improvements are unlikely unless the system is addressed at a fundamental level—for example, through adjustments to power balance, polarization, or spatial overlap.

Sample Preparation

For the experiments and to demonstrate the methods capabilities, we need to use samples that exhibit changes in optical path lengths at different points in space. While we utilized pre-made samples for some experiments, we also prepared some ourselves. In this section, we introduce these custom samples and explain the preparation process.

For an air bubble sample to show big ToF changes, we used a simple method to create a fixed specimen. A drop of superglue was placed on a glass slide, and air was injected into it with a fine needle, forming bubbles of various sizes. The glue's viscosity preserved the shape and distribution of the bubbles. A standard cover slip (125 µm) was placed over the sample, and after the glue hardened, the bubbles were fixed in place, providing a stable sample for imaging. This method enabled the selection of individual bubbles of varying size for analysis, well-suited to our experimental setup.

For a red blood cell sample to demonstrate the method at a cellular level, we sourced defibrinated horse blood from Fisher Scientific, chosen for its cost-effectiveness and since it lacks fibre it prevents clotting, ensuring a stable sample throughout preparation and imaging.

We used the thin smear technique to create a monolayer of cells, ideal for clear imaging, as illustrated in Fig. 3.7. A small drop of blood was placed near the frosted end of a clean slide, and a second slide was angled at 45° to the first. The blood spread along the edge of the angled slide, which was then swiftly moved across the first to create an even smear. This method minimized cell overlap, improving visualization under the microscope.

After air-drying, the slide was mounted in the microscope holder, ready for imaging. The thin smear technique provided reliable, high-quality red blood cell samples for our experiments.

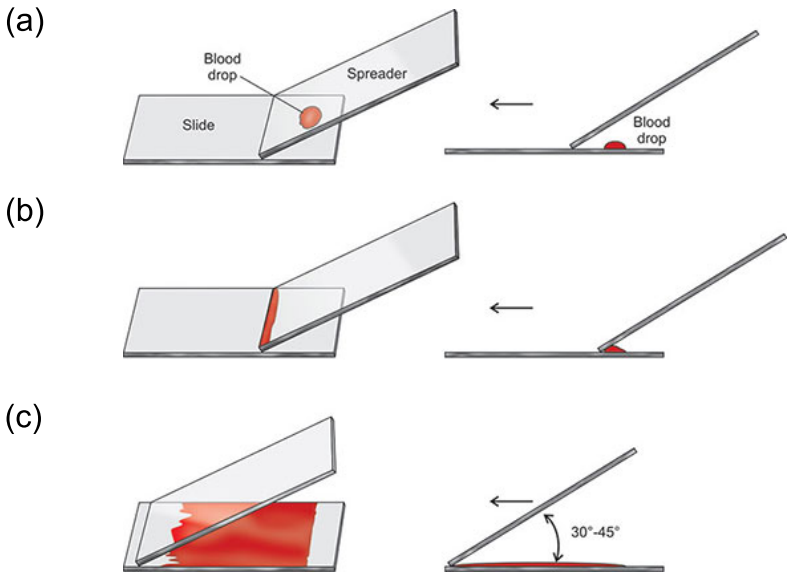

Figure 3.7: **Blood Smear Technique**: (a) A drop of blood is placed on one end of the slide. (b) Another slide is moved backward to make contact with the blood. (c) The blood is then smeared forward while maintaining a 45° angle. Figure adapted from [56].

3.3 Results

Single Wavelength Intensity Correlation Imaging

Here we present the results using a the single-wavelength setup with a central wavelength of around 780 nm and 10 nm bandwidth, focusing on the two different camera models. All results in this section were done using the auto-correlation $g^{(2)}$ as given in Eq. (2.22), as we only had one SPAD detector. First, I describe the results obtained with the MPD SPAD camera, combined with a rotating diffuser as a phase randomizer. The sample used for this experiment was an air bubble, prepared as described in the previous section. Air bubbles provide a simple sample with a clear, large optical delay step, which makes them ideal for demonstrating the performance of the system.

As shown in Fig. 3.8(a), the air bubble is clearly visible in the depth map with an optical delay of approximately 40 µm. Notably, there is a gradient in the depth across the bubble, as anticipated from the spherical shape. At the edges of the bubble, there is significant scattered light, which manifests as extreme values in the depth map. The simple intensity image is given in Fig. 3.8(b) where the airbubble boundaries can be seen.

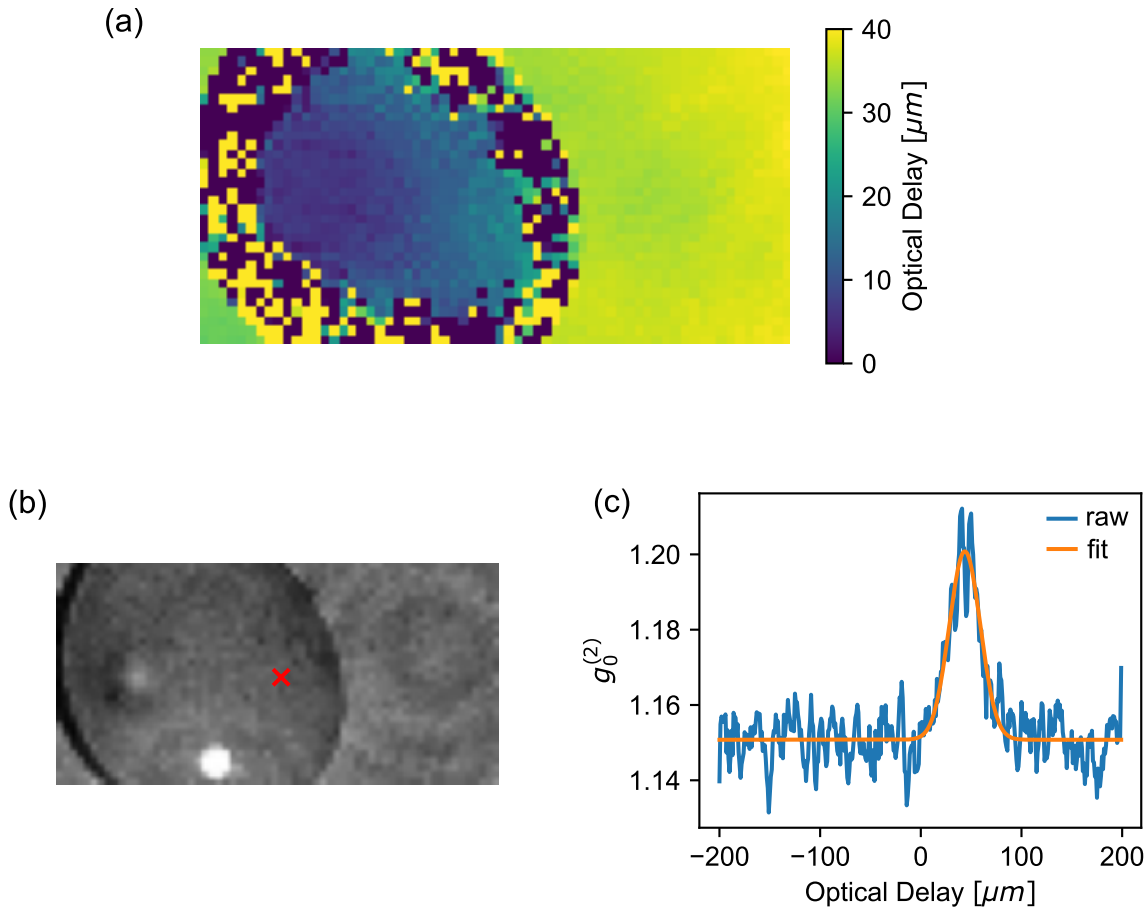

Figure 3.8: **Airbubble Micrograph:** (a) Depth image of an airbubble in glue measured in transmission. (b) Corresponding intensity image (c) $g^{(2)}$ measurements (blue) and fit (orange) used to extract the ToF information for the pixel marked with a red "x" in the intensity image. The offset is attributed to noise.

The refractive index of the glue used is estimated to be around 1.5, while the air inside the bubble is assumed to have a refractive index of approximately 1. Multiplying the optical delay by the refractive index difference, $\Delta n = 0.5$, gives an estimated physical size of the bubble of about 80 µm. For bubbles that remain nearly spherical, this depth measurement correlates well with the observed x-y dimensions of the bubble, which is roughly 120 µm. However, for larger bubbles, the assumption of spherical symmetry no longer holds, leading to some deviations in the depth map. Overall, these results confirm the ability of the single-wavelength method for measuring large optical delay steps, and the data matches the theoretical predictions within expected uncertainties. The use of a rotating diffuser further demonstrated that this technique is independent of spatial correlations.

The second set of results also using the rotating diffuser and SPAD camera focuses on imaging a Convallaria majalis cell, commonly known as lily of the valley. This plant sample is frequently

used in microscopy due to its well-defined internal cell structure, which makes it an excellent imaging target. In this case, we used a commercially prepared slide, though no specifications were provided regarding the thickness of the cell sample or the contact medium used during its preparation. As a result, these factors might introduce some variability in the measurements, and the results should be interpreted accordingly.

Despite these uncertainties(diffraction, scattering and non-uniform background), the depth image shown in Fig. 3.9(a) clearly reveals the structure of the Convallaria cell. The cell wall thickness was measured to be in the range of 10 µm to 20 µm, which aligns well with expected values for biological samples, typically ranging between 1 µm to 20 µm depending on the specific tissue. While the measurement is noisy with numerous outliers in the depth image, it still demonstrates the system's ability to resolve fine cellular details, although scattering at the cell edges poses challenges for achieving optimal clarity.

The previous results demonstrated the technique using a low-pixel SPAD camera with quick acquisition times; however, to measure smaller structures, a higher-pixel camera with a smaller pixel pitch is necessary. Therefore, we employed a slower CMOS camera to showcase the technique on a single cell allowing for a lateral diffraction limited resolution of $\sim 0.5\,\mu$m. Figure 3.10 presents the results, where we investigate red blood cells (RBCs) as the primary sample. The RBCs were prepared as described in Section 3.2.5. We employed a 40x magnification system and isolated a specific wavelength range using a bandpass filter centred at 810 nm with a 10 nm bandwidth.

In Figure 3.10(d), an intensity image of the RBC is shown, where the cell's outline is visible, though with relatively low contrast. This standard intensity image helps establish a reference for further analysis. Figure 3.10b focuses on a single pixel and presents the $g_a^{(2)}$ correlation peak (green), with its corresponding Gaussian fit (blue), demonstrating the ToF through the RBC at that pixel. The calculated depth map, shown in Figure 3.10(a), visualizes the cellular structure and distinctive concave disc shape typical of RBCs. Finally, Figure 3.10(c) offers a radial profile of the RBC, obtained by converting the 2D depth map into polar coordinates, providing further insight into the cell's shape and depth distribution.

These measurements resulted in an estimation of the RBC's diameter at approximately 5.5–6 μm and an effective optical thickness of 2.2 μm, where the optical thickness is defined as the product of the refractive index difference between the RBC and the surrounding medium, multiplied by the physical thickness of the cell. This value arises due to the difference in refractive indices between the RBC and the surrounding air, which influences how light travels through the sample in transmission mode.

The RBC diameter measurement aligns closely with existing literature on equine red blood

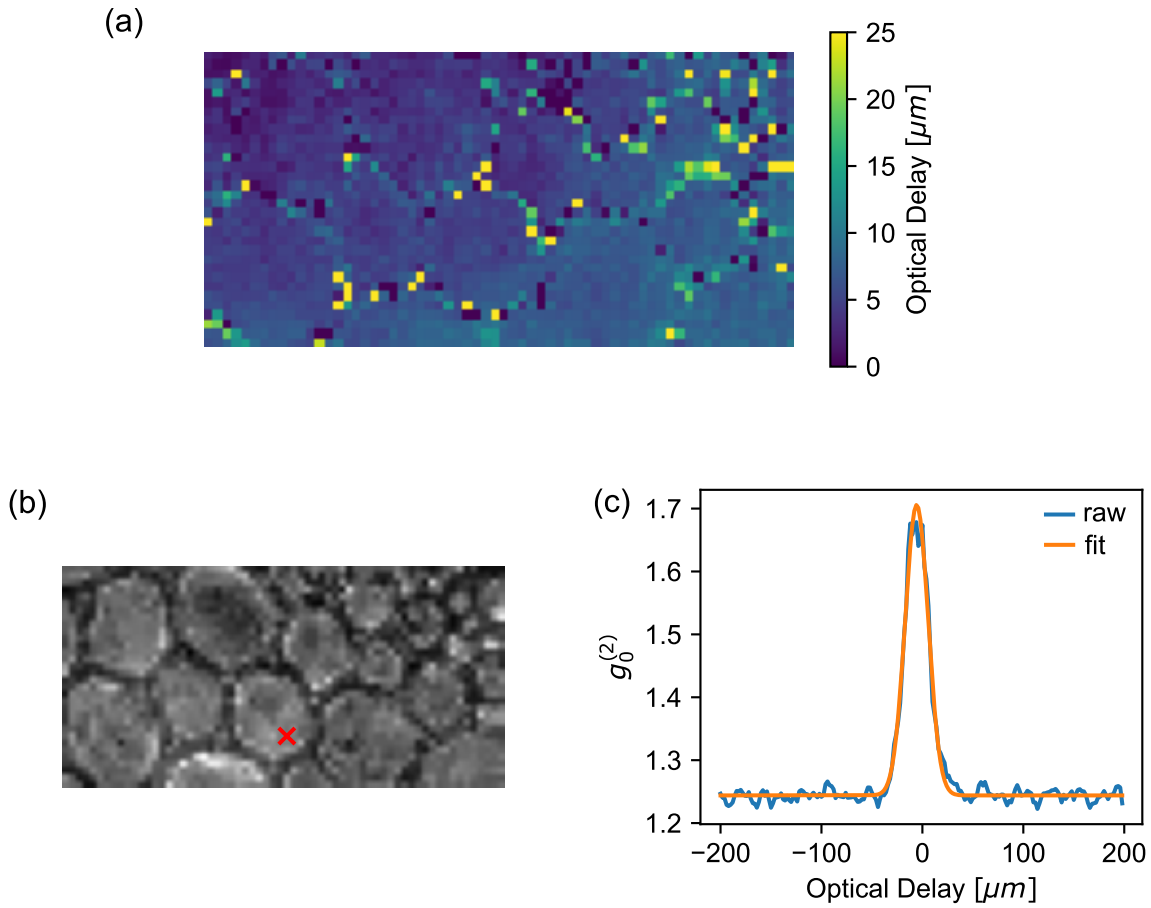

Figure 3.9: **Convallaria Cells Micrograph:** (a) Depth image of a Convallaria cell sample measured in transmission. Despite significant scattering, a non-uniform background, and noise, the structure in the depth is still visible and roughly matches the expected results, highlighting the limitations of this technique. (b) Corresponding intensity image. (c) The $g^{(2)}$ curve used to extract the ToF information for the pixel marked with a red "x" in the intensity image.

cells [57]. However, literature on RBC thickness focuses primarily on human samples, where thickness values range from 1.7 to 3.2 microns, with refractive indices ranging from 1.38 to 1.65 [58, 59, 60, 61, 62, 63, 64, 34]. Based on these variations, human RBCs can exhibit effective material thicknesses (optical thickness/refractive index) between 0.65 and 2.08 microns, which provides a useful reference range when considering the equine blood results.

This analysis demonstrates the capacity of our single-wavelength ToF microscope to effectively characterize biological samples such as RBCs, capturing both their structural dimensions and optical properties.

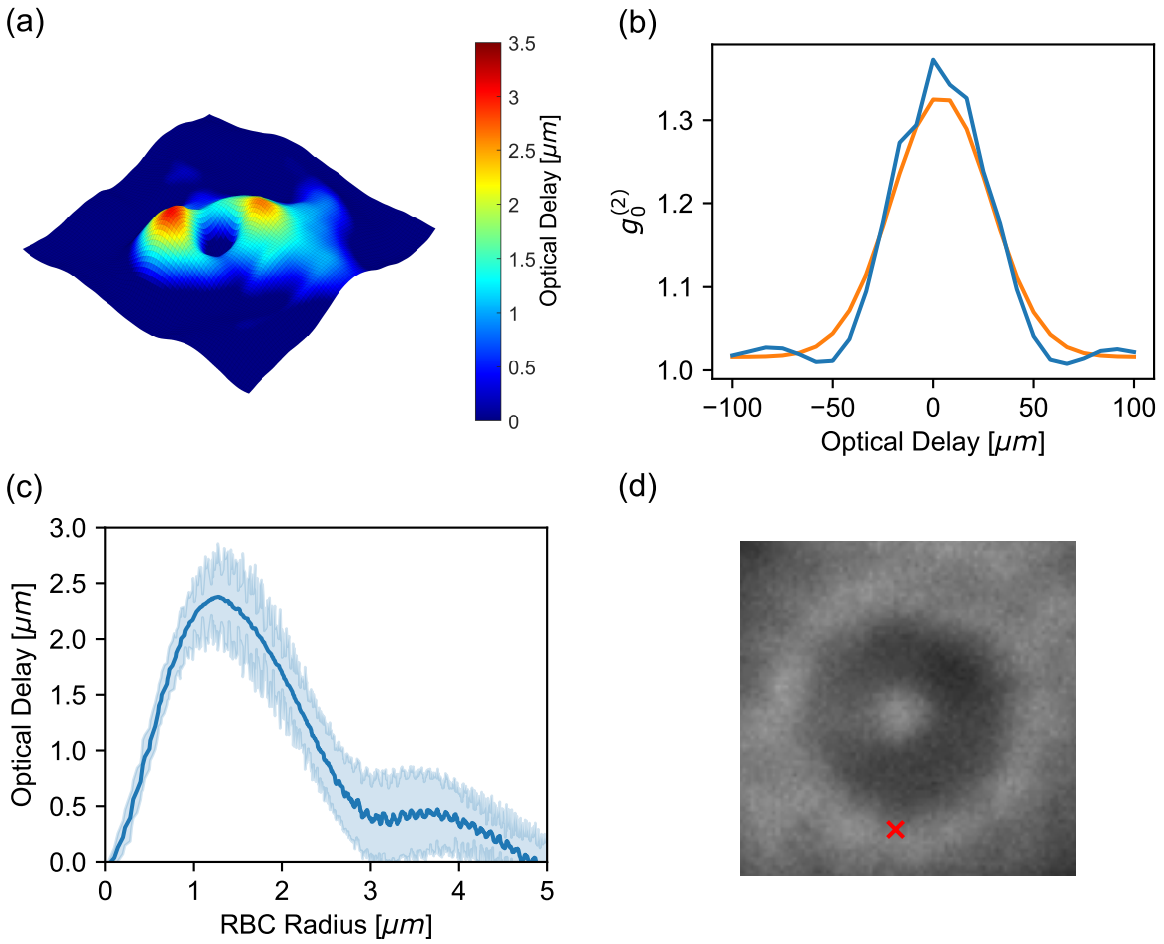

Figure 3.10: **Red Blood Cell Micrograph:** Example of single wavelength micron-scale measurement of red blood cells (RBCs). a) 3D depth image of RBC b) Measurement of the $g^{(2)_a}$ dip (green) and corresponding Gaussian fit (blue) for one pixel. c) The radial profile from the centre of RBC. d) Intensity image.

Dual Wavelength Intensity Correlation Imaging

In this section, we present our result using dual-wavelength intensity correlation imaging. The aim is to showcase the benefits of using two wavelength bands to enhance the axial resolution in time-of-flight (ToF) measurements, specifically for nanoscale structures.

Figure 3.11 shows the high-resolution results for a dual-wavelength measurement of a 10-layer graphene sample placed on a glass substrate. The setup involved filtering the supercontinuum white light source using two bandpass filters: one centred at 700 nm with a 10 nm bandwidth and the other at 850 nm with a 10 nm bandwidth. These filters were placed at ports A and B of our setup, respectively. The resulting interference between these two bands generates a synthetic wavelength of 3.97 μm, which can be observed as the beat pattern in the cross-correlation function $g_x^{(2)}$ shown in Fig. 3.11(d). This synthetic wavelength enhances the resolution of our depth

measurements beyond what is achievable with the single-wavelength method, as the sensitivity is now determined by the beating frequency rather than the coherence length (bandwidth). A single wavelength with the same bandwidth would not only provide lower resolution, as shown in the FI analysis, but it would also be technically more challenging, as the entire spectrum must be provided and accounted for in terms of dispersion rather than just two bands.

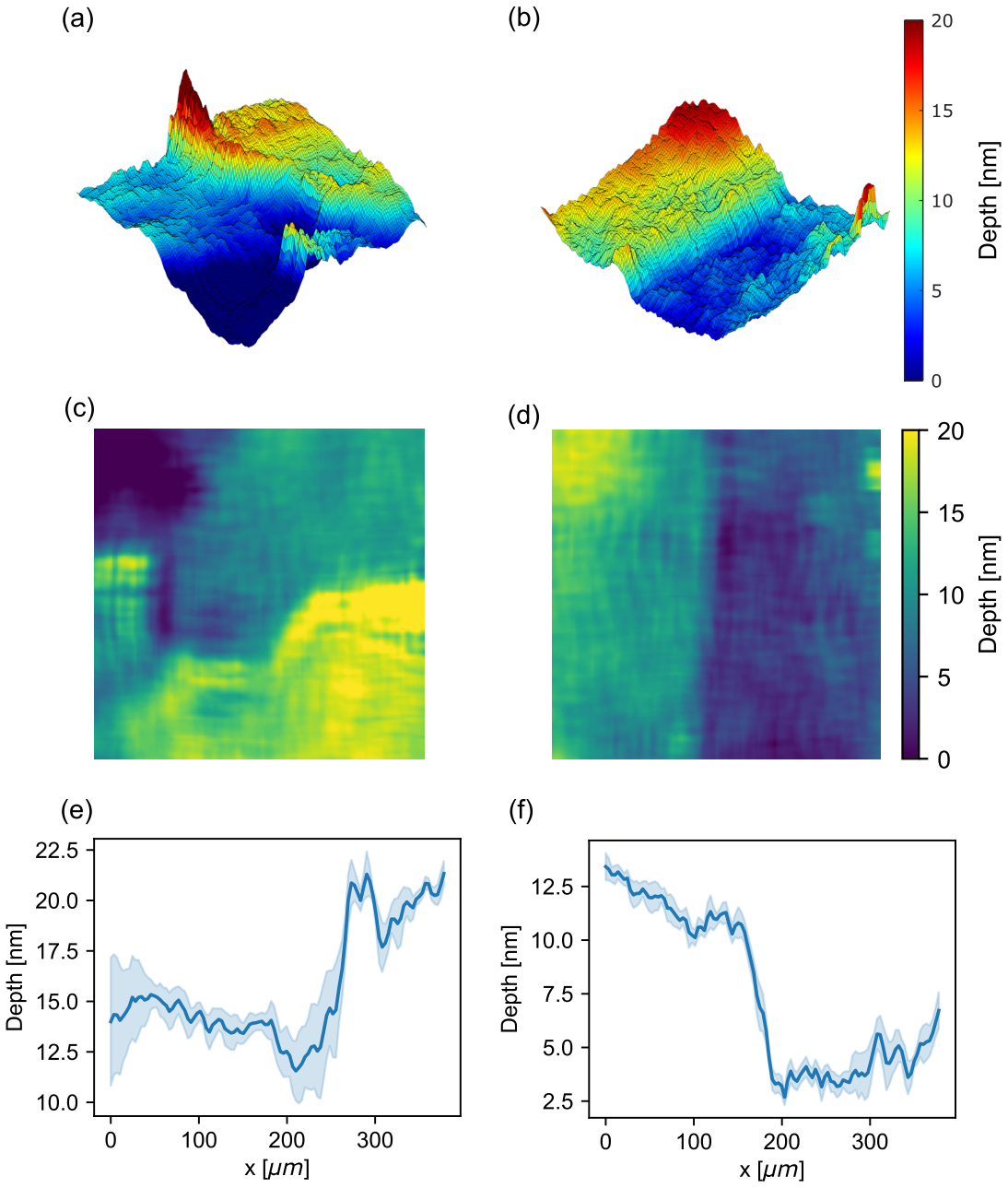

Figure 3.11: **Graphene Depth Measurement:** Example of a dual wavelength nanoscale measurement on a graphene layer sample. (a) and (b)Depth images of two areas (I and II) of the graphene layer visualised in 3D, showing a clear step. (c) and (d) show the same data as in (a) and (b), now visualised in 2D (e)-(f) A 1-D cutout from the depth map averaged over 20 pixels normal to the graphene interface.

To achieve nanometre-scale axial resolution, it's critical to minimize optical component dispersion, especially when there is a large separation between the two wavelength bands. Dispersion can shift the zero optical delay of one wavelength relative to the other, degrading the measurement accuracy. To mitigate this, we carefully matched the dispersion in both arms of the interferometer by using identical imaging optics for both the sample and reference arms. Specifically, we replaced the microscope objective with two achromatic 50 mm lenses in both arms, allowing us to image an approximate 300x300 μm area of the graphene layer onto the camera with minimal dispersion. This lens configuration reduces the lateral resolution to the pixel limit of 3.5 μm.

Figures 3.11(c) and (d) show the depth images from two different regions of the graphene sample. These depth images were generated from the $g_x^{(2)}$ cross-correlation traces and reveal the presence of nanometre-scale features, particularly a clear step at the boundary of the graphene layer. The graphene layer itself has an approximate thickness of $d_g = 5$ nm and a refractive index of $n_g = 3$ [65]. Based on these values, the effective optical thickness, calculated as $(n_g - n_{air}) \cdot d$, is approximately 10 nm, which matches well with the depth obtained from our ToF measurements.

Figures 3.11(e) and (f) provide a more quantitative view of these depth images by presenting 1D line cuts normal to the graphene interface, further highlighting the nanoscale steps observed. Additionally, Figures 3.11(a) and (b) show 3D visualizations of the same data, emphasizing the detailed topography of the graphene layer, with clear delineation of the steps at the boundaries. This experiment demonstrates the effectiveness of dual-wavelength ToF microscopy for resolving nanoscale features in materials like graphene, with resolution improvements due to the synthetic wavelength created by the two optical bands.

3.4 Future Works

Although we did not pursue this approach in our current work due to the lack of required equipment and time constraints, we have developed the theory and models for two distinct methods: one that combines single-wavelength and dual-wavelength techniques for single-shot measurements, and another that measures the dual-wavelength $g^{(2)}$ in the frequency domain using a swept-source.

Combined Single and Dual Wavelength Single-Shot Measurement

In this section, we introduce a novel method that integrates single-wavelength and dual-wavelength approaches to achieve single-shot measurements, drastically reducing acquisition time by only measuring a single optical delay. This method utilizes the existing dual-wavelength setup without requiring additional components, using auto-correlation and cross-correlation $g^{(2)}$ to simultaneously capture single- and dual-wavelength data.

One requirement is that we position the system within the coherent window, allowing for single-shot acquisition. The g^2 autocorrelation yields the single-wavelength peak, while cross-correlation captures the dual-wavelength peak. The single-wavelength data offers a preliminary estimate of the optical delay, similar to [66], which is then refined by the dual-wavelength data to achieve significantly higher resolution. Using only the dual-wavelength data would introduce range ambiguity due to the periodic nature of the signal; thus, combining both approaches helps to unwrap this phase. The key advantage of this approach is the elimination of mechanical scanning, significantly improving stability and acquisition speed. However, the measurement range remains constrained by the coherence length, with phase ambiguity beyond π still a concern. Proper bandwidth and beating frequency selection are crucial. Addressing these challenges may require analyzing intensity fluctuation statistics, while careful wavelength and bandwidth choices ensure the precision needed for accurate phase unwrapping.

Frequency Domain Synthetic Wavelength

Here, we discuss the potential of moving from time-domain scanning to frequency-domain scanning while still capitalizing on the underlying benefits of dual-wavelength $g^{(2)}$.

Starting from Eq. (2.28), where we observe a beating pattern in the g^2 correlation when using two wavelength bands, the frequency of this beating depends on both the time delay δt and the wavelength separation $\Delta\omega$. In the experimental approach discussed so far, we focused on fixing

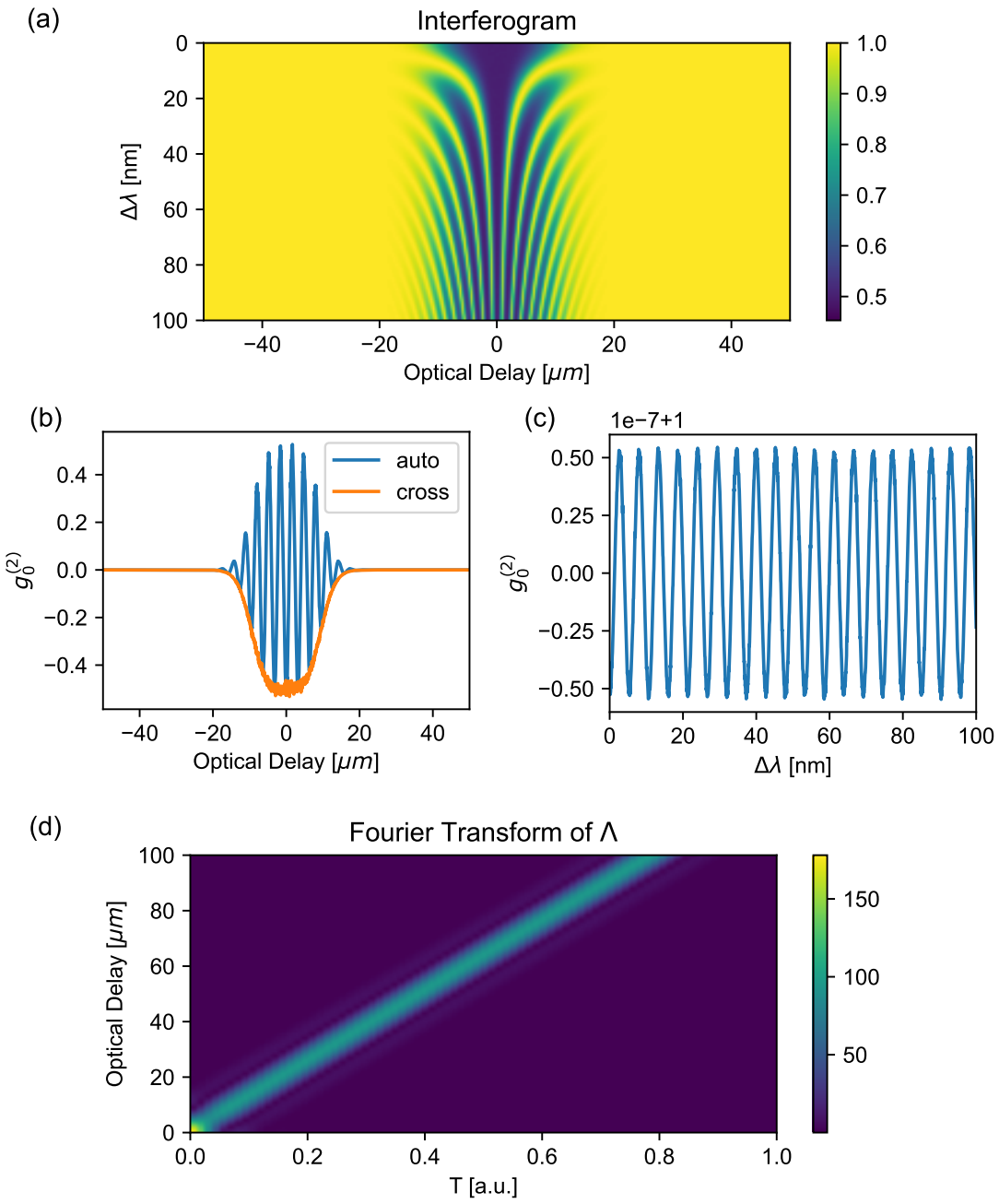

Figure 3.12: **Frequency Domain Dual Wavelength Concept:** Illustration of the conceptual link between time and frequency domains in synthetic wavelength generation. (a) A 2D interferogram as a function of frequency and time for a dual-laser system with a common finite coherence length. (b) A cutout of a single $\Delta\lambda$, showing the beating in the cross-correlation and the envelope in the auto-correlation. (c) A cutout of a single optical delay as a function of $\Delta\lambda$, revealing periodic beating. (d) The Fourier transform of $\Delta\lambda$ for different optical delays, showing a one-to-one mapping between optical delay and beating frequency in the frequency domain.

the wavelength separation and scanning the optical delay, Δt, to observe this beating, with its position shifting across pixels based on the delay.

However, the method proposed here suggests reversing the process: fix the optical delay and scan the dual-wavelength separation. This would produce an equivalent beating, but now in the frequency domain. In this configuration, the optical delay would define the frequency of the beating, and this delay would vary pixel-to-pixel across the image.

There are two potential experimental implementations. The first involves using a tunable laser paired with a fixed, short-coherence laser. Since the coherence length is dominated by the shorter-wavelength laser, the second laser can be adjusted in frequency. The second option uses a broad-band laser source and a spectrometer, where the wavelength bands are separated at the output ports. With this setup, the g^2 correlation can be calculated for different wavelength separations.

By combining spectral and temporal data, we generate a 2D interferogram (see Fig. 3.12(a), where vertical slices show the frequency domain beating that varies with the optical delay (as illustrated in Fig. 3.12(c). Horizontal slices yield a result analogous to the dual-wavelength case, showing a beating with a coherent envelope, which intensifies as wavelength separation increases.

The key insight here is that the frequency domain approach allows for a fixed optical delay, avoiding the need for mechanical scanning. This stability can enhance the precision of the experiment, although it comes with its own trade-offs. The resolution of this method depends on the bandwidth of the scanned wavelength range. A larger bandwidth provides higher resolution but also demands finer time-domain features. In essence, there is a reciprocal relationship between time and frequency domain scanning—higher frequency resolution requires a broader bandwidth, just as high temporal resolution would require more finely spaced optical delay scans.

The main challenge is selecting the appropriate equipment to balance this trade-off. For example, achieving high resolution demands a wide bandwidth, which is difficult with conventional tunable lasers. A more feasible solution could involve using a grating or supercontinuum source, though this may reduce the frequency resolution. Thus, one must carefully weigh the trade-off between frequency range and resolution depending on the application.

Ultimately, while this approach might not offer specific advantages over time-domain scanning (for the same spectral bandwidth) beyond eliminating mechanical delays, its non-mechanical nature could offer improved stability. For these reasons, it stands as an interesting alternative for future experimentation, though it requires careful consideration of the experimental trade-offs.

3.5 Conclusion

In this study, we have introduced a novel Time-of-Flight (ToF) microscopy technique that leverages intensity correlation measurements within a phase-randomized interferometer. This approach, which focuses on the g^2 dip position, serves as a classical analogue to the more complex quantum Hong-Ou-Mandel (HOM) microscopy [45, 44], providing a practical yet high-resolution imaging solution.

Our single-wavelength ToF microscopy offers significant advantages in its simplicity and ease of implementation, utilizing just a single laser source and a conventional camera without the need for complex components.

The dual-wavelength approach, on the other hand, significantly enhances the sensitivity and resolution of our system. By utilizing two wavelengths, we create a synthetic wavelength that improves depth resolution to the nanometre scale. This technique is especially powerful for imaging nanoscale structures, such as graphene layers, where precise resolution is crucial. Remarkably, the dual-wavelength method can be implemented with basic, cost-effective components—low-quality lasers of different wavelengths and conventional imaging sensors. This affordability and accessibility make our method a practical option for high-resolution imaging.

Compared to existing techniques, our approach is notably robust and straightforward, distinguished by its ease of use and freedom from the typical complexities of more advanced systems. Furthermore, by incorporating a rotating diffuser in some of the experiments, we demonstrate that our technique does not rely on either spatial or temporal coherence. Compared to existing ToF microscopy techniques, our approach introduces notable advancements in simplicity, accessibility, and robustness. By leveraging intensity correlation measurements, we provide a classical analogue to quantum Hong-Ou-Mandel microscopy, achieving high axial resolution. However, it is important to critically evaluate the utility of the $g^{(2)}$ technique compared to conventional methods. For stable samples, traditional phase-based techniques or methods based on First-Order Correlation ($g^{(1)}$), such as SLIM, offer superior performance in terms of speed (up to 15 fps) and precision (sub-nanometre axial resolution). These methods are both faster and more accurate, making them better suited for applications where stability is not a limiting factor. In contrast, the $g^{(2)}$ technique demonstrates its unique advantages primarily in scenarios involving incoherent or rapidly moving samples (where the sample dynamics are faster than the acquisition time of First-Order Correlation ($g^{(1)}$) techniques). It is also particularly effective in noisy environments, where the inherent robustness of second-order correlations allows for reliable imaging under challenging conditions. While the dual-wavelength approach enhances axial resolution to the nanometre scale and is accessible with low-cost components, it still relies on stable laser sources to achieve optimal performance and depends on the sample dispersion. Despite these

limitations, our method offers a unique balance of affordability, robustness, and high resolution, making it a compelling option for specific imaging scenarios where conventional techniques fall short.

Looking ahead, there are exciting opportunities for further development. These limitations, such as acquisition speed and dependency on laser stability, underscore the importance of future developments like faster cameras and chip-level integration of g^2 calculations. The introduction of faster, higher-resolution cameras could substantially improve acquisition speed and data quality [67]. Moreover, integrating g^2 calculations directly onto chip-level processing units could significantly reduce both processing times and data transfer rates, enhancing the technique's efficiency and suitability for real-time applications [68].

In summary, our ToF microscopy technique offers a promising, low-cost, high-resolution imaging solution with considerable potential. It is particularly effective in high-noise environments or when imaging incoherent samples. By combining the simplicity of single-wavelength imaging with the advanced precision of dual-wavelength setups, this method provides a versatile tool for a broad range of scientific and industrial applications, balancing practicality with cutting-edge performance.

Chapter 4.

Synthetic Wavelength Imaging through Scattering Media

In this chapter, we discuss how we can combine Synthetic-Wavelength Holography with the principle of Second-Order Correlation ($g^{(2)}$) to provide a highly robust measurement technique that achieves imaging through scattering media (ITSM). The advantage of this approach is that it provides Synthetic-Wavelength Holograms (SWHs) without relying on optical holography, making it robust against phase noise. This method excels in dynamic scattering scenarios and performs better in low signal-to-noise ratio (SNR) conditions, as it allows for longer acquisition times due to its increased stability as compared to holographic detection methods. The experiment has been conducted in collaboration with Florian Willomitzer and Patrick Cornwall at the University of Arizona. The iterative optimization of the reconstruction algorithm has been formalized by Areeba Fatima at the University of Glasgow.

4.1 Scattering-based Imaging

Non-Line-of-Sight (NLOS) imaging [69] refers to the visualization of objects hidden from direct view, such as those located around corners. A related concept is Imaging Through Scattering Media (ITSM), which applies to scenarios where an object is embedded between two planes of scattering. ITSM can also be extended to cases involving continuous scattering across multiple layers, such as in volume-scattering media. Both techniques share the same underlying principle: reconstructing hidden objects by analysing the scattered light that has been reflected from surfaces or diffused through the media. By analysing the scattered light—whether it is from a wall, scatterer, or within volume-scattering media—using time, frequency, or spatial data, researchers can reconstruct these hidden scenes. Since NLOS imaging has been extensively studied in the literature, the rest of this subsection will present techniques specifically developed for NLOS imaging. These methods can be directly applied to ITSM. When referring to NLOS, it should be understood that ITSM is also being referenced. At the core of NLOS & ITSM is the transient light transport process, where light pulses reflect from a hidden scene to a visible surface, and are then captured by a sensor. By solving the inverse problem — reconstructing the hidden scene from indirect measurements and noisy data— these techniques achieve impressive reconstructions, even in complex environments. Emerging at the intersection of advanced optics, computational imaging, and signal processing, NLOS imaging holds transformative potential across diverse fields

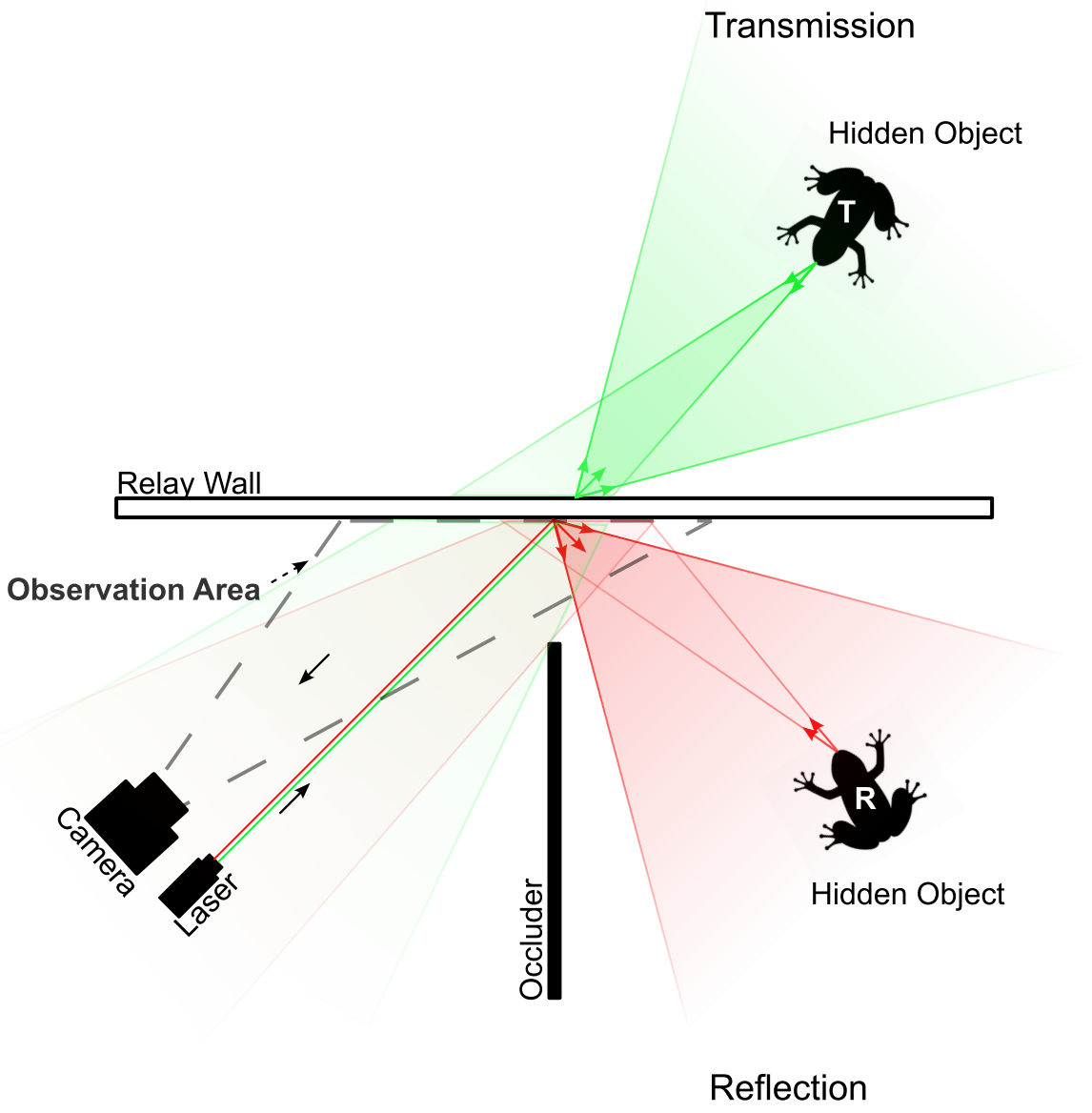

Figure 4.1: **Non-line-of-Sight Imaging vs. Imaging through Scattering:** Schematic of the imaging procedure. The observer directs a laser onto a relay wall, where the light scatters into the hidden area containing the unseen object. This can occur via transmission through a diffuser (imaging through scattering) or reflection from a scattering wall (NLOS imaging). The backscattered light is then collected by a camera and computationally reconstructed to reveal the hidden object.

such as remote sensing, surveillance, and medical imaging. In autonomous driving, it could enable vehicles to detect hazards around corners, enhancing safety. In the defence sector, NLOS imaging offers improved situational awareness in obscured areas. Medical imaging could benefit from visualizing regions inside the body that are inaccessible with traditional methods. In search-and-rescue operations, it could assist in locating individuals trapped behind obstacles or debris, providing critical information about their condition and location. As technology evolves,

NLOS imaging is poised to become a vital tool in industries ranging from archaeology to industrial monitoring. Over time, researchers have explored various modalities to advance the application of NLOS imaging, employing a wide range of techniques to improve its capabilities. These include using optical visible light, acoustic waves [69], millimetre waves [70], and infrared thermal imaging [71]. Initially, some methods focus solely on localization, detection, or classification, providing sufficient information for certain applications, while having the potential to be employed for real-time operation without the need for full scene reconstruction [72, 73, 74]. Broadly, current strategies for imaging predominantly rely on scanning methodologies using optical light, typically requiring either high temporal resolution measurements or an exploration of spatial correlations. Various techniques have been developed to solve the NLOS inverse problem. These techniques can be broadly categorized based on their reliance on time-of-flight (ToF) data, frequency analysis, or data-driven methods [75]. Each approach brings specific strengths depending on the hardware setup and application. These are some of the well known technique used for NLOS imaging.

ToF or Transient Imaging Methods

Time-of-Flight (ToF) NLOS imaging techniques reconstruct hidden surfaces by illuminating a scene with temporally modulated light and capturing the response with fast detectors positioned at multiple spatial locations on an intermediary surface, such as a wall or floor. These methods achieve centimetre-scale lateral resolution within a working volume of several m^3, and some systems enable near real-time reconstructions, although their efficiency is limited by the need to raster-scan large areas. ToF NLOS imaging typically employs time-resolved detectors, such as SPADs [76, 77], to measure photon flux relative to a light pulse, producing transient images that illustrate light paths, including both direct and indirect reflections. While direct light is typically gated out due to its lack of useful information, the focus remains on the indirect light that reflects off a visible surface, then a hidden surface, before returning to the detector.

Confocal Backprojection Method

The image formation model for confocal non-line-of-sight (NLOS) systems, where both the laser source and detector are positioned at the same point, is articulated through a time-of-flight equation that correlates photon arrival times with the distances travelled. This model includes factors such as reflectance, surface normals, and the intricate interactions of light with the hidden scene. Specifically, the model for time-resolved indirect light transport in a confocal NLOS system—where both the laser illumination and subsequent detection occur at the same visible surface point (x', y')—can be formulated as [78, 75]

$$\tau(x', y', t) = \iiint_{\Omega} \frac{1}{r^2} \rho(x, y, z)\, g(x', y', x, y, z)\, \delta\left(2\sqrt{(x'-x)^2 + (y'-y)^2 + z^2} - tc\right) dx\, dy\, dz, \tag{4.1}$$

where ρ represents the reflectance at a specific point in the hidden scene, and the Dirac delta function δ relates the time of flight t to the distance function $r = \sqrt{(x'-x)^2 + (y'-y)^2 + z^2} = \frac{tc}{2}$. Here c is the speed of light and x, y, z the spatial coordinates of the hidden volume. The sampling happens in on z-plane ($z = 0$) in x', y'. The impulse response of the system is embedded in the Dirac delta function δ. The function g encompasses various time-independent attenuation effects, influenced by hidden surface normals, the reflectance characteristics of the hidden scene, and the visibility of a hidden point from the sampling location (x', y'), among other factors. Although this model is inherently non-linear due to the complexities involved in light transport—such as multiple scattering events, occlusions, and the attenuation of light as it interacts with different materials—it can be approximated by a linear model that simplifies calculations, assuming isotropic scattering and the absence of occlusions. The problem can be discretized to a linear transform of equations :

$$\tau = A\rho, \tag{4.2}$$

where A is the operator describing the light transport in the NLOS scene. In the general non-confocal image formation model, ρ spans three spatial dimensions, while τ incorporates two spatial dimensions and one temporal dimension, significantly increasing the computational complexity of matrix A. Although the confocal approach simplifies certain aspects, it comes with limitations, particularly the challenges posed by direct reflections, which can saturate sensitive detectors. These issues are drastically reduced for a non-confocal setup.

The back-projection method has long been the standard approach in confocal setups, approximating ρ using the inverse of the light transport matrix multiplied by the transient images ($A^T\tau$), often combined with digital filters for enhanced reconstruction [79, 80, 81]. This technique adopts a "reverse light path" approach, projecting detected light backward to estimate hidden object positions, akin to tomography in medical imaging. By measuring the time-of-flight of light across multiple reflections, it enables 3D reconstruction of concealed scenes. The confocal back-projection method closely resembles strategies for solving large-scale inverse problems. While linearized models simplify inversion for easier reconstruction, more complex models capture finer details but require greater computational resources, with a complexity of $O(N^5)$, where N represents the number of discretized elements along one spatial dimension of the hidden scene. This method often encounters ill-posed problems, known as the missing cone problem, necessitating statistical priors for estimation. Despite its straightforward nature, back-projection is

susceptible to noise and may yield limited resolution in complex or diffuse environments, making it computationally intensive, especially for high-resolution imaging or larger areas.

Light-Cone Transform

Another class of methods proposed for NLOS imaging involves linear inverse methods, which aim to solve the convex optimization problem of estimating ρ from τ. While iterative optimization techniques have been suggested, they often incur high computational costs, resulting in slow performance. The introduction of the light-cone transform offers a closed-form solution to the linear inverse problem, efficiently addressing the exact linear inverse with a computational complexity of $O(N^3 \log N)$ [82, 83]. The method models light propagation as travelling along a cone-shaped path from the visible surface to the hidden object and back, transforming the inverse problem of NLOS imaging into a deconvolution problem. This transformation further streamlines the reconstruction process, converting the 3D space-time measurement data into a transformed space, thereby improving computational efficiency. This approach assumes a smoothness prior on the reconstructed volume, achieving near real-time processing speeds [84].

Occlusion-based NLOS imaging model

Up until this point, the model has been simplified by setting $g = 1$ in the image formation model, thereby rendering the problem linear. However, with the occlusion-based algorithm, this constraint is lifted, allowing the non-linear problem to be addressed directly. The proposed light transport representation now integrates inverse methods that decompose the global illumination components of a transient image into hidden albedos, surface normals, and visibility terms, effectively modelling partial occlusions in complex scenes. It is often formed as a visibility term V that indicates the occlusion relationship between two spatial points. Importantly, this occlusion term can be unified into the optical transport matrix A, thereby reducing the condition number and facilitating reconstruction. Simulations demonstrate that this factorization approach improves the robustness and quality of NLOS imaging, particularly in scenarios involving partial occlusions. Experimental data support these findings, although they also highlight that the non-convex nature of the factored light transport model can introduce ambiguities in the reconstructions [85, 86, 87]. Nevertheless, the factored light transport representation requires $O(N^5)$ memory to store the visibility terms, making it significantly more memory-intensive than other matrix-free NLOS algorithms.

Phasor-Field Virtual Wave Optics Method

Phasor-field virtual optics [88, 89] offers a wave-based approach to non-line-of-sight (NLOS) imaging, contrasting with traditional geometric optics models. Based on the wave equation:

$$\nabla^2\Psi - \frac{1}{v^2}\frac{\partial^2\Psi}{\partial t^2} = 0 \tag{4.3}$$

This method uses wave optics to process light transport from occluded environments. Central to this technique is the phasor field, a virtual wave field that encodes light's spatial and temporal information as it propagates through a scene. By treating the transient image as a virtual wave field and applying the Rayleigh-Sommerfeld diffraction integral, hidden scenes can be reconstructed through wave propagation. The method is more robust than previous models, as it handles complex scenarios involving multiple scattering, non-Lambertian surfaces, occlusions, and larger depth ranges, making it suitable for real-world imaging. Moreover, this framework enables virtual imaging systems that mimic traditional line-of-sight techniques such as photography and transient imaging. The phasor-field approach has demonstrated improved image quality and robustness to noise, working well with shorter exposure times and varying lighting conditions.

f-k Migration

Borrowed from seismic imaging [90], the f-k migration technique provides a wave-based approach to solving the confocal NLOS reconstruction problem, offering several advantages over previous discussed methods such as filtered back-projection and light cone transform. The essence of f-k migration lies in using Fourier transforms and interpolation to migrate from the frequency domain, f, to the wave number domain k_z, enabling the transformation of the measured field $\Psi(x, y, z = 0, t)$ into $\Psi(x, y, z, t = 0)$. One of its key strengths lies in its ability to produce high-quality reconstructions in scenes with varying reflectance functions, such as diffuse and specular surfaces, even in noisy environments. This robustness is demonstrated through both simulated and experimental data collected with a prototype NLOS system [82, 91]. However, there are inherent limitations to the technique. While f-k migration is an exact solution to the wave equation, its current implementations do not consider phase information, focusing solely on amplitude measurements. This omission introduces reconstruction errors, as seen in specific experimental results. Additionally, the highly oscillatory nature of the wave field poses challenges for modelling visible light frequencies at the scales used in NLOS imaging. Another limitation stems from the approximation nature of the technique when dealing with microscopic surface geometries, such as those responsible for diffuse and specular reflections. Although f-k migration performs well compared to state-of-the-art methods, it remains an approximate solution to the NLOS problem.

Resolution

Time-of-flight (ToF) based non-line-of-sight (NLOS) imaging techniques adhere to fundamental resolution limits defined by the area on the visible surface and the precision with which pulses can be measured. Analogous to the numerical aperture of an optical system, the scanning area determines the lateral resolution, while the temporal resolution imposes limits on the axial resolution, similar to the wavelength limitations of conventional systems. These resolutions can be expressed as [78]:

$$\begin{aligned} \Delta x &\geq \frac{c \times \sqrt{w^2 + z^2}}{2w} \,\text{FWHM}, \\ \Delta y &\geq \frac{c \times \sqrt{w^2 + z^2}}{2w} \,\text{FWHM}, \\ \Delta z &\geq \frac{c \times \text{FWHM}}{2}. \end{aligned} \tag{4.4}$$

Here, FWHM represents the temporal response of the system, and the scanning area is of size $2w \times 2w$.

Steady-State Techniques

An alternative approach to time-of-flight methods in NLOS imaging utilizes steady-state techniques that exploit correlations in the scattered optical fields, rather than temporal data. Most of them are based on spatial or angular correlation using the memory effect to do NLOS imaging. The memory effect is defined as a range within one degree of freedom where the speckle pattern stays the same [92, 93]. These methods provide significantly higher lateral resolution down to the micron level and can operate with smaller detection surface areas; however, these advantages come with the trade-off of a highly restricted angular field of view (FoV), determined by the angular decorrelation of scattered light. This decorrelation increases with the thickness of the scatterer. This angular memory effect not only limits the field of view but also constrains the maximum size of measurable objects, which cannot exceed the respective working volume. Leveraging the angular memory effect, researchers have demonstrated the ability to track moving objects with precision [94]. This effect has also been applied to NLOS imaging, either by scanning the angle of the illumination laser [95] or using randomized illumination sources to recover hidden scenes [96].

Another type of speckle memory effect is the spectral memory effect, where the speckle pattern remains unchanged for small shifts in the laser wavelength. This phenomenon forms the foundation of the approach discussed in the next section: Synthetic Wavelength Holography.

Passive Methods

In addition to methods that utilize active illumination, there are also passive techniques that do not require it. The methods do not necessitate time-resolved imaging systems and just capture a static light field. However, the associated inverse problems are significantly more ill-posed compared to those encountered in active imaging, leading to the necessity of restrictive assumptions. This technique is particularly ill-posed, making it challenging to achieve high-quality reconstructions using conventional cameras alone. Existing research addresses this issue by reducing the condition number of the transport matrix A through the introduction of additional constraints, thereby enhancing imaging quality. Reconstruction typically occurs under three common constraints: partial occluders [97], coherence [98], and polarization [99].

Deep Learning Methods

Machine learning, particularly deep learning, has significantly advanced NLOS imaging through learning-based approaches. Convolutional neural networks (CNNs) and other machine learning algorithms are trained on extensive datasets of NLOS data to predict hidden scenes from indirect light measurements. By effectively modelling the light transport function, these models can accurately reconstruct hidden objects, even in complex or dynamic environments.

A key advantage of learning-based methods lies in their ability to process intricate and noisy datasets where traditional algorithms often struggle. Once trained, a CNN can reconstruct a scene from NLOS data much more rapidly than conventional methods. However, these models necessitate large amounts of training data, and their performance may decline when confronted with novel scenarios or scenes that differ from those in their training set, which poses challenges in generalization.

Current state-of-the-art research can be categorized into two types: models that are end-to-end, simply learning a mapping [100, 101, 73, 102, 103, 104], and more advanced models that are physics-inspired or grounded in physical laws [105, 106, 107].

Synthetic Wavelength Holography

SWH, which leverages the spectral memory effect, facilitates 3D imaging in both Line-of-Sight (LOS) and Non-Line-of-Sight (NLOS) scenarios. By exploiting spectral correlations between closely spaced optical wavelengths, this technique enables precise imaging through computational reconstruction, making it adaptable to challenging conditions such as scattering media,

rough surfaces, and hidden objects.

The fundamental principle of SWH involves utilizing two wavelengths, λ_1 and λ_2, to create a synthetic wavelength (Λ), defined by the same equation as in Chapter 3:

$$\Lambda = \frac{\lambda_1 \lambda_2}{|\lambda_1 - \lambda_2|} \tag{3.1}$$

In Line-of-Sight (LOS) imaging or imaging in direct view, SWH enables high-resolution 3D surface reconstructions with sub-millimetre precision. The key advantage of using a synthetic wavelength instead of an optical wavelength is its unperturbed reflection from rough surfaces, where optical wavelengths typically scatter. This phase randomization due to surface roughness presents challenges for traditional interferometry. As a result, SWH can achieve micron-scale axial and spatial resolution at video frame rates, making it particularly advantageous in fields like computer vision and biomedical imaging [108, 109].

In NLOS imaging, the light scatters off a visible surface, functioning as a virtual source/detector (VSD). By collecting light at the VSD, the system can capture scattered light from hidden objects, allowing for the reconstruction of both shape and position with high spatial resolution using simple wave propagation methods, also achieving sub-millimetre precision [110, 111]. The same concept, utilizing SWH, can be applied to ITSM.

The quality of object reconstruction in synthetic holography hinges on the optical path changes induced by scatterers. As detailed in [110], the Rayleigh quarter wavelength criterion remains applicable at synthetic wavelengths. This criterion posits that speckle formation occurs when the maximum path length variation Ψ, combined with geometric factors, exceeds one-quarter of the wavelength. Leading to the criterion:

$$\Psi < \frac{\Lambda}{4} \tag{4.5}$$

Thus, this criterion establishes a soft lower limit for the required synthetic wavelength, while adherence to Abbe's diffraction limit [112] indicates that increasing the synthetic wavelength reduces resolution. Therefore, an optimal synthetic wavelength must strike a balance between Signal-to-Noise Ratio (SNR) and resolution, as comprehensively analysed in the results section of this chapter

Currently, techniques employing SWL have primarily relied on holographic methods for generating the SWH. However, this approach undermines the robustness of SWL, as it remains sensitive to phase coherence and stability during acquisition. Consequently, many existing imaging techniques based on SWH are hindered by issues related to phase noise, scattering, and instabilities inherent to holographic methods. Our findings reveal a connection between synthetic

wavelength holograms and the beat frequencies observed in our $g^{(2)}$ correlation measurements, prompting the development of a new approach that eliminates the dependence on phase stability and traditional holographic techniques.

4.2 Methods

$g^{(2)}$ Synthetic Wavelength Hologram Generation

Principle

To generate the Synthetic-Wavelength (SWL), we rely on the Second-Order Correlation ($g^{(2)}$) correlation function. The beating phenomenon described in Eq. (2.28) directly corresponds to the SWL, enabling its use in subsequent analysis. To create a large SWL necessary for ITSM imaging, a very small wavelength separation of our dual-wavelength laser source is required (< 0.1 nm). However, separating the two wavelengths at each port with such a small separation between the bands is both challenging and impractical. This necessitates the use of the second configuration derived in Section 2.3, which involves simultaneously detecting both wavelengths with a single camera, as expressed in Eq. (2.31). However, this approach comes at the cost of reduced visibility; specifically, the autocorrelation terms introduce an additional offset, resulting in a maximum visibility of 0.25, compared to 0.5 for the filtered case.

As with all other $g^{(2)}$ methods discussed in this thesis, it is essential to incorporate phase fluctuations to obtain a temporal average of the intensity product. This can be accomplished by capturing multiple intensity frames while manually varying the phase.

For this application, we can make several assumptions. Given the need for stable, long-coherent lasers for large SWL, we can first assume an effectively infinite coherence length, denoted as $g^{(1)}_{(\Delta t)} = g^{(1)}_{(0)}$. This simplification is crucial, as it reduces the equation to fewer unknowns. Consequently, our $g^{(2)}$ measurement equation simplifies to:

$$g^{(2)}_{\Lambda}(\Delta t) = 1 + \frac{1}{8}|g^{(1)}_{(0,I)}|^2 + \frac{1}{8}|g^{(1)}_{(0,II)}|^2 + \frac{1}{4}|g^{(1)}_{(0,I)}||g^{(1)}_{(0,II)}|\cos(\Delta\omega\Delta t). \tag{4.6}$$

Since this equation applies to a single pixel, we introduce a new index i for the pixels. The coherence terms $|g^{(1)}_{(0,I,i)}|^2$ will carry this index, and we introduce a phase term for the relative phase difference between each pixel, Φ_i. Additionally, we denote α_i and β_i for $\frac{1}{4}|g^{(1)}_{(0,I,i)}|^2$ and $\frac{1}{4}|g^{(1)}_{(0,II,i)}|^2$, respectively. Thus, we have:

$$g_{\Lambda}^{(2)}(\Delta t) = \left[1 + \frac{1}{2}\alpha_i + \frac{1}{2}\beta_i + \sqrt{\alpha_i \beta_i}|\cos(\Delta\omega\Delta t + \Phi_i)\right]. \tag{4.7}$$

This equation bears a strong resemblance to the intensity equation of an interferometer, making it an analogy in the $g^{(2)}$ domain. For the experiment, we must fully characterize this beating, which involves measuring the hologram (SWH). To extract comprehensive information, we utilize phase steps, analogous to the I/Q-demodulation technique.

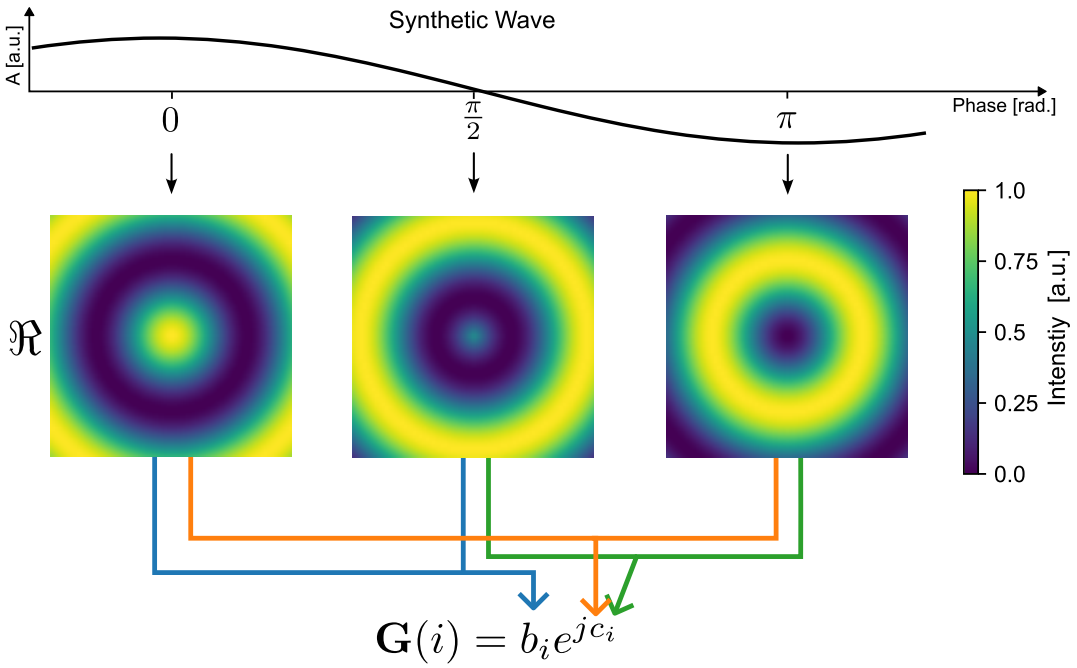

Figure 4.2: $g^{(2)}$ **Hologram Generation:** This section outlines the procedure for generating a hologram of the synthetic wavelength (SWL) from $g^{(2)}$ measurements by employing three phase steps: 0, $\frac{\pi}{2}$, and π. The resulting hologram represents the direct measurements obtained from $g^{(2)}$, reflecting the real part of the field. A: Amplitude

For a sinusoidal signal of known frequency $\Delta\omega$, we can express this as:

$$\mathrm{s}(\Delta t\Delta\omega) = a + b\sin(\Delta t\Delta\omega + c). \tag{4.8}$$

The technique is illustrated in Fig. 4.2, showing how three phase steps $(0, +\pi/2, +\pi)$ can be used to recover three unknowns. This approach is based on fundamental holography techniques, which employ the corresponding equations to achieve this recovery.

$$
\begin{aligned}
a &= \frac{\mathrm{s}(0) + \mathrm{s}(\pi)}{2}, \\
b &= \sqrt{\mathrm{s}(0)^2 + \mathrm{s}(\pi/2)^2}, \\
c &= \arctan\left[\mathrm{s}(0) - a, \mathrm{s}(\pi/2) - a\right].
\end{aligned}
\tag{4.9}
$$

This allows us to relate these parameters back to our physical terms, incorporating the pixel index:

$$
\begin{aligned}
a_i &= 1 + \frac{1}{2}\alpha_i + \frac{1}{2}\beta_i, \\
b_i &= \sqrt{\alpha_i \beta_i}, \\
c_i &= \Phi_i.
\end{aligned}
\tag{4.10}
$$

Currently, this technique requires three measurements corresponding to three different phase shifts. However, we can make additional assumptions to reduce this time. First, since the wavelengths are very closely spaced, we can assume they exhibit similar characteristics in terms of absorption and polarization rotation. Second, if both wavelengths have the same intensity entering the interferometer, we can conclude that they also share the same visibility, hence $\alpha_i = \beta_i$. Given this, the equations simplify to:

$$
\begin{aligned}
a_i &= 1 + \alpha_i, \\
b_i &= \alpha_i, \\
c_i &= \Phi_i.
\end{aligned}
\tag{4.11}
$$

This results in a direct correlation between a_i and b_i. Consequently, if we ensure that the inputs from the two lasers are identical, we only need two phase shifts $(0, \pi/2)$ to solve the two unknowns. Moreover, it may be possible to apply this technique in a single shot by using the distribution across the entire image as an estimate for an average α_i value, which can then be scaled by the intensity image—expected to be the primary factor influencing visibility changes (variations in α_i). Furthermore, since the field generally propagates after the object, continuity in the phase hologram should be maintained, allowing for the application of generic unwrapping

techniques.

Additionally, we could not only conduct $g^{(2)}$ analysis but also delve deeper into the statistics of the fluctuations. For a flat phase change induced by the piezo, spatial correlations in the fluctuations could also be utilized to predict the phase. These single-shot methodologies remain untested at this stage; however, it is crucial to note that they are probabilistic rather than deterministic, unlike the multiple phase step approaches. They may also be most effective in simpler cases where the number of scattering events is limited, rather than in scenarios involving extensive bulk scattering.

To reconstruct the hologram, we use the values gathered to construct the synthetic wavelength hologram, denoted as **G**:

$$\mathbf{G}(i) = b_i e^{jc_i}. \tag{4.12}$$

Experimental Setup

The experimental setup is based on a Mach-Zehnder interferometer, consisting of a reference and a sample path, as shown in Fig. 4.5(a) for the transmission and Fig. 4.5(f) for the reflection setup. To create a hologram with a long synthetic wavelength, a highly precise and stable separation between the two continuous-wave laser sources is crucial. For this reason, the Toptica DFB Pro 855 nm laser system was selected, which features two independent laser heads. These heads are intensity- and temperature-controlled, minimizing fluctuations, and are tunable by a few nanometres thermally or up to 50 GHz via electronic tuning.

A fibre beamsplitter (Thorlabs TW850R5A2) was used at the input of the Mach-Zehnder interferometer. This choice was motivated by the fact that both laser heads are fibre-coupled, and using a polarization-maintaining, single-mode fibre beamsplitter ensures that both wavelengths remain fully aligned in terms of space and polarization when exiting the fibre into the scene. For the reference arm, one output of the fibre splitter was directed into a large beam collimator (Thorlabs F810APC). To facilitate the $g^{(2)}$ process, a phase scrambling mechanism was added to the interferometer. The collimator was mounted on a piezo translation stage (Thorlabs NF15AP25), which allowed small shifts to be introduced into the interferometer delay at kHz rates, providing the required phase randomization.

The second output of the fibre beamsplitter was directed toward the scene. Depending on the setup, the fibre was either pointed directly at the diffuser with a diverging beam or a collimator was used to illuminate the scatterer with a single spot. Additionally, the fibre was repositioned

either in front of or behind the object depending on whether the transmission or reflection setup was used. The speckled light from the camera-side diffuser was collected by a 50 mm lens and imaged onto the camera. Before reaching the camera, however, the light was recombined with the reference beam at a 50:50 free-space beamsplitter (BS033), producing interference on the camera.

A critical aspect of the setup was ensuring that the speckle size was not significantly smaller than the camera's pixel size. An iris was placed in the imaging setup to increase speckle size when necessary by filtering in k-space. However, increasing the speckle size also reduced the amount of light collected, as it required a smaller aperture.

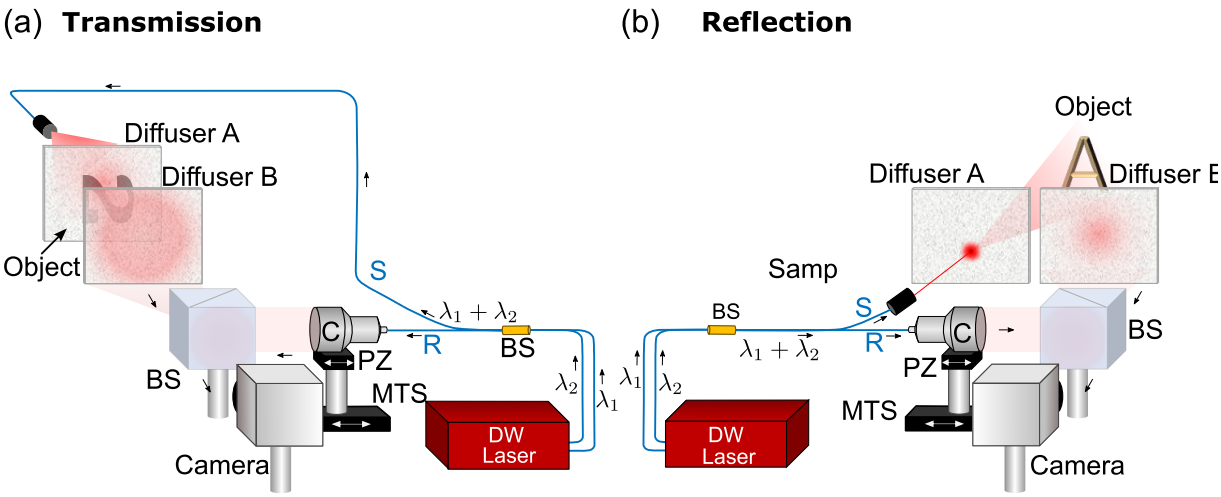

Figure 4.3: **ITSM Experimental Setup:** Schematic of the ITSM procedure: (a) Capturing multiple intensity images of a hidden object illuminated by a dual-wavelength laser and interfered with a randomized reference signal in transmission. (b) The same process in reflection. BS: Beamsplitter, DW: Dual Wavelength, MTS: Mechanical Translation Stage, PZ: Piezo Translation Stage, R: Reference Arm, S: Sample Arm.

To capture synthetic wavelength hologram G effectively, we used a Basler acA720-520um camera, operating at a frame rate of approximately 500 Hz with a resolution of 720x540 pixels and a pixel size of 6.9 μm $\times$ 6.9 μm. A high frame rate was essential due to the large number of frames required for $g^{(2)}$ measurements, and the faster camera significantly reduced the acquisition time. To efficiently capture the phase-randomized frames, a measurement procedure was developed. The camera and piezo stage were controlled by a microcontroller connected to the computer via serial communication. A randomized phase-stepping sequence, generated with a fixed-seed random number generator and a maximum step size, was loaded onto the microcontroller. The microcontroller is moving the piezo stage by applying a voltage to it. Once the piezo moved, the microcontroller triggers the camera and waits for it to acquire the frame. After receiving the ready signal from the camera, the microcontroller sends the next voltage step to the piezo. The controlling computer provided the microcontroller with the number of frames needed

and controlled the acquisition start and stop. During acquisition, the computer simultaneously loaded frames from the camera buffer, ensuring that the piezo did not move during frame capture and that multiple cameras, if used, remained synchronized. There is one important technical detail that needs to be highlighted. Since we needed to measure a hologram at a fixed plane or z-position, this was straightforward for a single diffuser. However, for volume scatterers with a broad k-spectrum, a smaller aperture was required to limit the field of view. While this increased the depth of field, it degraded the hologram by measuring over a larger z-space. One solution was to add a thin, scattering layer on the surface of the volume scatterer, or even sand down the surface, to create a more defined scattering plane, allowing for more accurate hologram calculations.

Computational Reconstruction

To reconstruct the hidden object from our synthetic wavelength hologram G, we propagate the field G using established wave propagation techniques. After conducting preliminary tests, we employ the Angular Spectrum Method (ASM) for this purpose [113]. The ASM numerically backpropagates the hologram to the stand-off distance where the object is located. The amplitude of this backpropagated field reveals the object's shape and reflectivity. Additionally, propagating to different standoff distances allows us to extract depth information, providing a more complete 3D representation of the hidden scene.

For our experimental setup, we approximate free space propagation conditions through the medium. In this approximation, the optical field computed from $g^{(2)}$ correlations, denoted as $G_m(x, y, z)$, is modelled as the propagated field of the object plane field $G(x, y, 0)$, where x and y are the transverse coordinates and z is the propagation distance. In the general form of the ASM, the field G_m can be expressed as:

$$G(x, y, z) = \iint df_x\, df_y \left[\hat{G}(f_x, f_y, 0) \exp(iz\alpha)\right] \exp[i2\pi(f_x x + f_y y)], \tag{4.13}$$

where $\hat{G}(f_x, f_y, 0)$ is the Fourier transform of $G(x, y, 0)$, and α is defined as:

$$\alpha = \sqrt{\left(\frac{2\pi}{\lambda}\right)^2 - 4\pi^2(f_x^2 + f_y^2)}. \tag{4.14}$$

The optical field evolution described by Eq. (4.13) can be interpreted as a sequence of three operations on the source field: a Fourier transform, multiplication with the transfer function $\exp(iz\alpha)$, and finally an inverse Fourier transform. In matrix operator form, the measured field

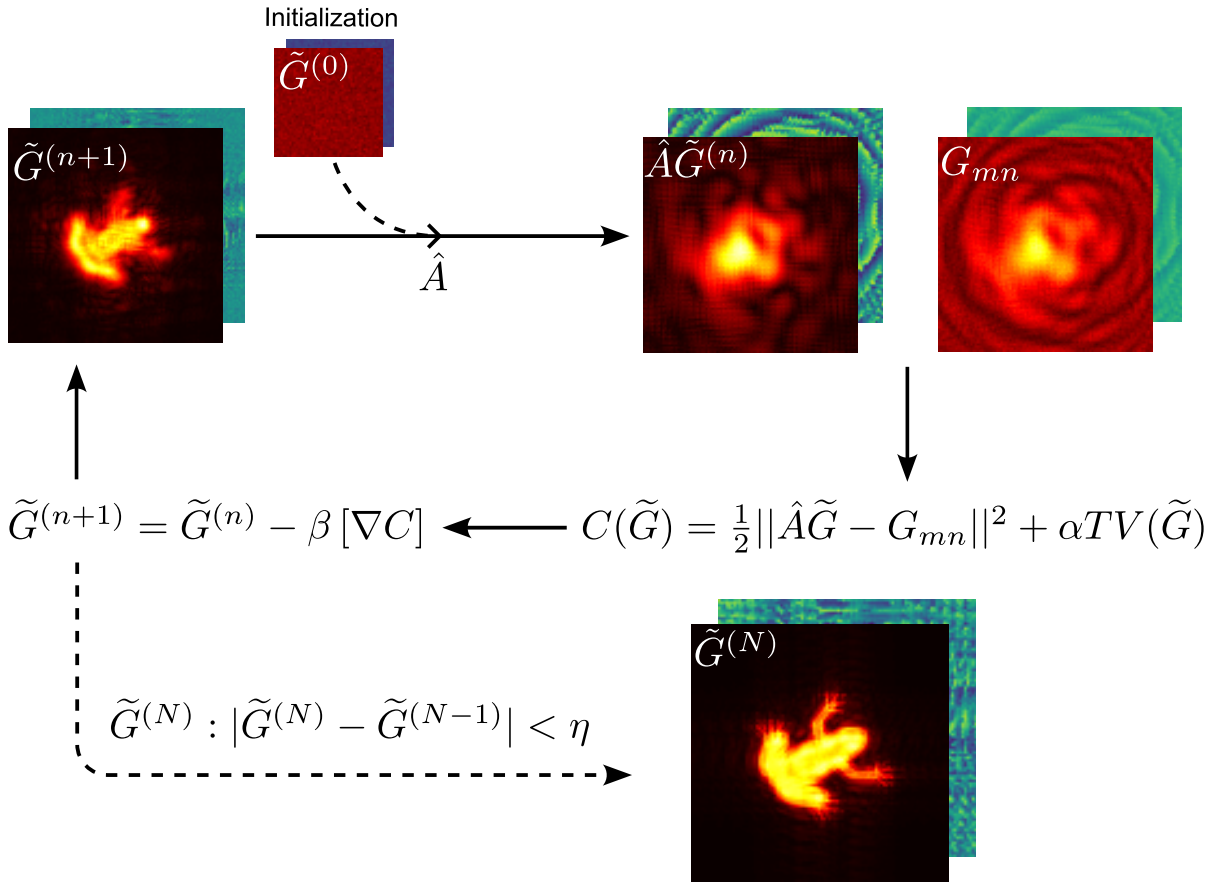

Figure 4.4: **Iterative Computational Reconstruction**: Schematic illustrating the flow of the algorithm. Starting with an initial random guess, $\hat{A}$ is applied, and the cost function C is computed. This updates the guess iteratively using a learning rate β. The process continues until the update falls below a predefined tolerance η, at which point the iteration stops. The final field, $\widetilde{G}^{(N)}$, reveals the hidden object (a frog).

G_m is given by:

$$G_m = \mathcal{F}^{-1}\left[\hat{H}\left[\mathcal{F}\{G(x,y,0)\}\right]\right] + \epsilon = \hat{A}G + \epsilon, \tag{4.15}$$

where ϵ represents measurement noise, $\mathcal{F}$ and $\mathcal{F}^{-1}$ are the 2D Fourier transform and its inverse, respectively, and $\hat{H}$ is the transfer function operator. The simplest approach is to apply this directly to our measured field G_m to recover the object. However, this leads to numerous artefacts and degradation due to the presence of noise. Thus, we develop an iterative algorithm to address this issue [114]. The goal of this algorithm is to retrieve the object field $G(x, y, 0)$ by finding the optimal solution $\hat{G}$ that minimizes the cost function:

$$\hat{G} = \arg\min_{\widetilde{G}} C(\widetilde{G}), \tag{4.16}$$

where

$$C(\widetilde{G}) = \frac{1}{2}||\hat{A}\widetilde{G} - G_m||^2 + \alpha TV(\widetilde{G}, \widetilde{G}^*). \tag{4.17}$$

Here, the first term is the data fidelity term, ensuring similarity with the measurements, while the second term is the Total-Variation (TV) regularizer weighted by a constant, α.

The iterative solution for retrieving $G(x, y, 0)$ via gradient descent updates the guess $\widetilde{E}_i$ at each iteration with learning rate β:

$$\widetilde{G}^{(n+1)} = \widetilde{G}^{(n)} - \beta \left[\nabla_{\widetilde{G}^*} C(\widetilde{G}, \widetilde{G}^*)\right]_{\widetilde{G}=\widetilde{G}^{(n)}}, \tag{4.18}$$

with the cost function gradient given by:

$$\nabla_{\widetilde{G}} C(\widetilde{G}) = \hat{A}^\dagger(\hat{A}\widetilde{G} - G_m) - \alpha\nabla\left(\frac{\nabla\widetilde{G}}{|\nabla\widetilde{G}|}\right), \tag{4.19}$$

where $\hat{A}^\dagger$ is the adjoint operator of $\hat{A}$, defined as:

$$\hat{A}^\dagger = \mathcal{F}^{-1}\hat{H}^*\mathcal{F}. \tag{4.20}$$

Additionally, we can employ a multispectral approach for particularly challenging cases where significant scattering occurs. For reconstructions using N synthetic wavelengths, we can rewrite the cost function in the form:

$$C(\widetilde{E}) = \frac{1}{2}\sum_{n=1}^{N} ||\hat{A}_{\lambda n}\widetilde{G} - G_{mn}||^2 + \alpha TV(\widetilde{G}, \widetilde{G}^*), \tag{4.21}$$

where the subscript λn (with $n = 1, 2, 3, ..$) refers to the different synthetic wavelength values defining the transfer function $\hat{H}$. The first N terms represent the data fidelity for the measurements G_{mn} corresponding to each synthetic wavelength, yielding a fused reconstruction.

4.3 Results

Point-Source Backpropagation through a Ground Glass Diffuser

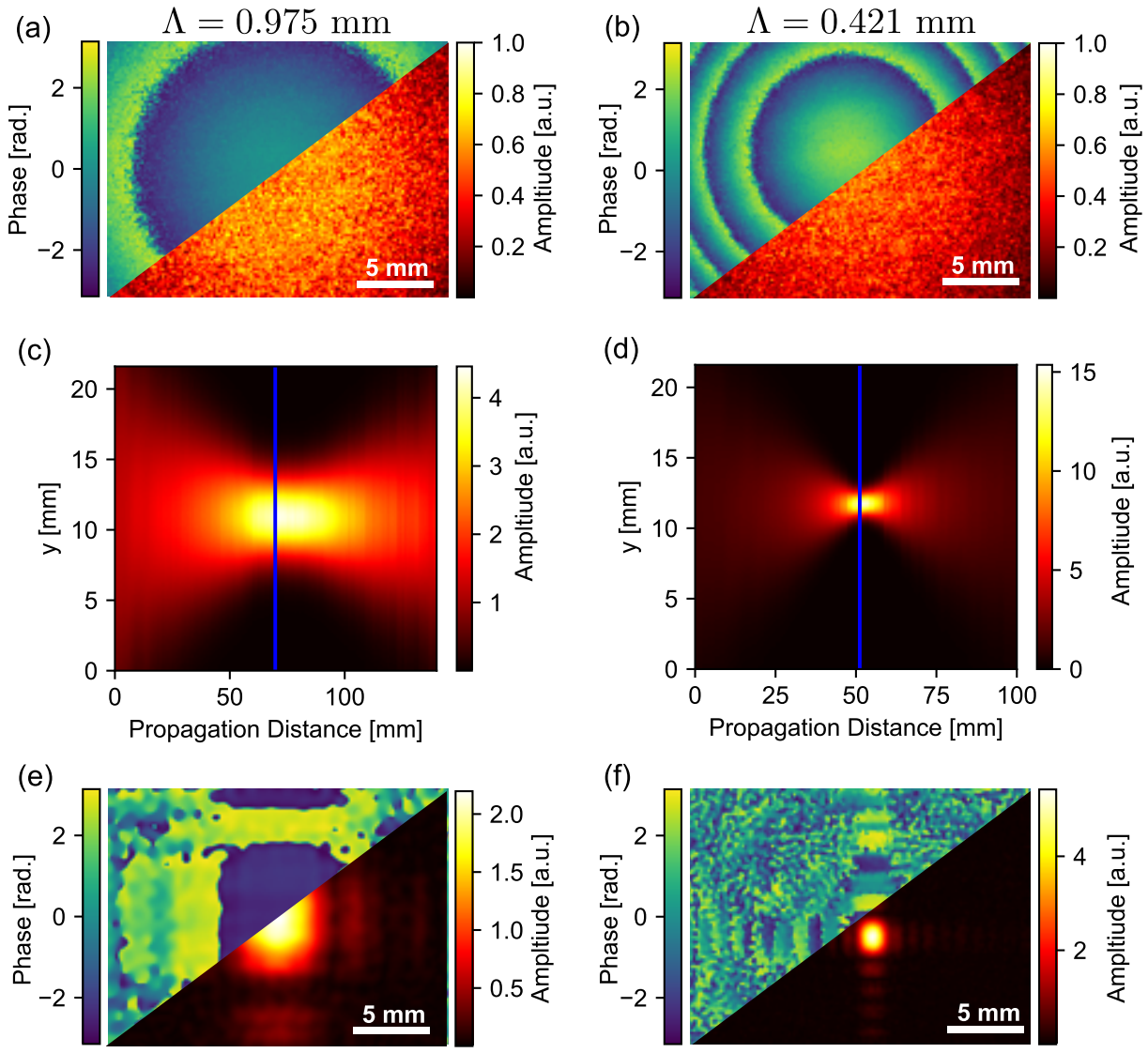

Figure 4.5: **Single Diffuser Point-Source Backpropagation**: Reconstructed field of a point source hidden behind a single ground glass diffuser. (a)-(b) Display the field with the left colormap representing the phase and the right colormap showing the amplitude. (c)-(d) A 2D cutout of the 3D propagated field, revealing a waist at the point source location (indicated in blue). (e)-(f) Show the phase and amplitude in the plane of the point source. (a), (c) & (e) use a synthetic wavelength of 0.975 mm, while (b), (d) & (f) use a synthetic wavelength of 0.421 mm.

To demonstrate the capabilities of our imaging system, evaluate its resolution limits, and show that the SWH can be interpreted as a physical wave, we begin by using a single ground-glass diffuser with a grit of 120 as the scatterer. Our experimental setup involves placing a

fiber tip at a distance of 60 cm behind the diffuser, allowing light to diverge from the fiber tip and illuminate the diffuser surface. We measure the hologram formed at the diffuser plane and subsequently backpropagate the field to a standoff distance, which is not necessarily the physical distance. The standoff distance is chosen such that the backpropagated hologram creates the sharpest image. This empirical finding is characteristic for synthetic wavelength imaging, as corroborated in [110].

This investigation is conducted with two distinct synthetic wavelengths, $\Lambda_1 = 0.975\,\text{mm}$ and $\Lambda_2 = 0.421\,\text{mm}$. As shown in Fig. 4.5(a) and (b), the measured fields for Λ_1 and Λ_2 are presented, where the blue-green colour represents the phase, and the red-yellow colour denotes the amplitude. To further illustrate the propagation of the fields through space, we represent the fields in the x-z dimension in Fig. 4.5(c) and (d), which exhibit behaviour consistent with that of a Gaussian beam. The fields at the stand-off distance are depicted in (e) and (f), demonstrating two distinct beam waists. As expected, a larger beam waist corresponds to the larger synthetic wavelength, Λ_1. The question arises: Is this beam waist limited by Abbe's diffraction limit as it would be for a physical wave?

The resolution of our system is fundamentally constrained by the diffraction limit, which is defined as: [112]

$$\delta_{x,y} = \frac{\Lambda}{2\text{NA}} \tag{4.22}$$

Relating to our exact optical geometries in our setup visualized in Fig. 4.6(a). The numerical aperture (NA) is defined as:

$$\text{NA} = n\sin(\alpha) \approx n\tan(\alpha) = \frac{r}{\text{z}}, \tag{4.23}$$

where the approximation $\sin(\alpha) \approx \tan(\alpha)$ is valid for small numerical apertures but becomes inaccurate for larger NAs. Thus, we express the NA more generally as:

$$\text{NA} = \frac{r}{\sqrt{r^2 + (\text{z})^2}}. \tag{4.24}$$

In our setup, the diffuser acts as an entrance pupil, limiting the possible values of k_x and k_y, which subsequently affects the NA. This results in a resolution term derived from our experimental configuration:

$$\delta_x = \frac{\Lambda\sqrt{r^2 + (\text{z})^2}}{2r}, \tag{4.25}$$

indicating that the final reconstruction resolution depends on the synthetic wavelength and the distance between the diffuser and the object. We measured the holograms of three different wavelengths at five distinct standoff distances, comparing the results to theoretical predictions. These results are presented in Fig. 4.6(b), demonstrating that the synthetic wavelengths adhere to the Abbe diffraction limit, analogous to physical waves. However, deviations were observed at shorter standoff distances due to errors in the defined NA, as the fiber tip does not function as a point source. Instead, its limited diverging angle restricts the NA, rather than the size of the image on the relay wall.

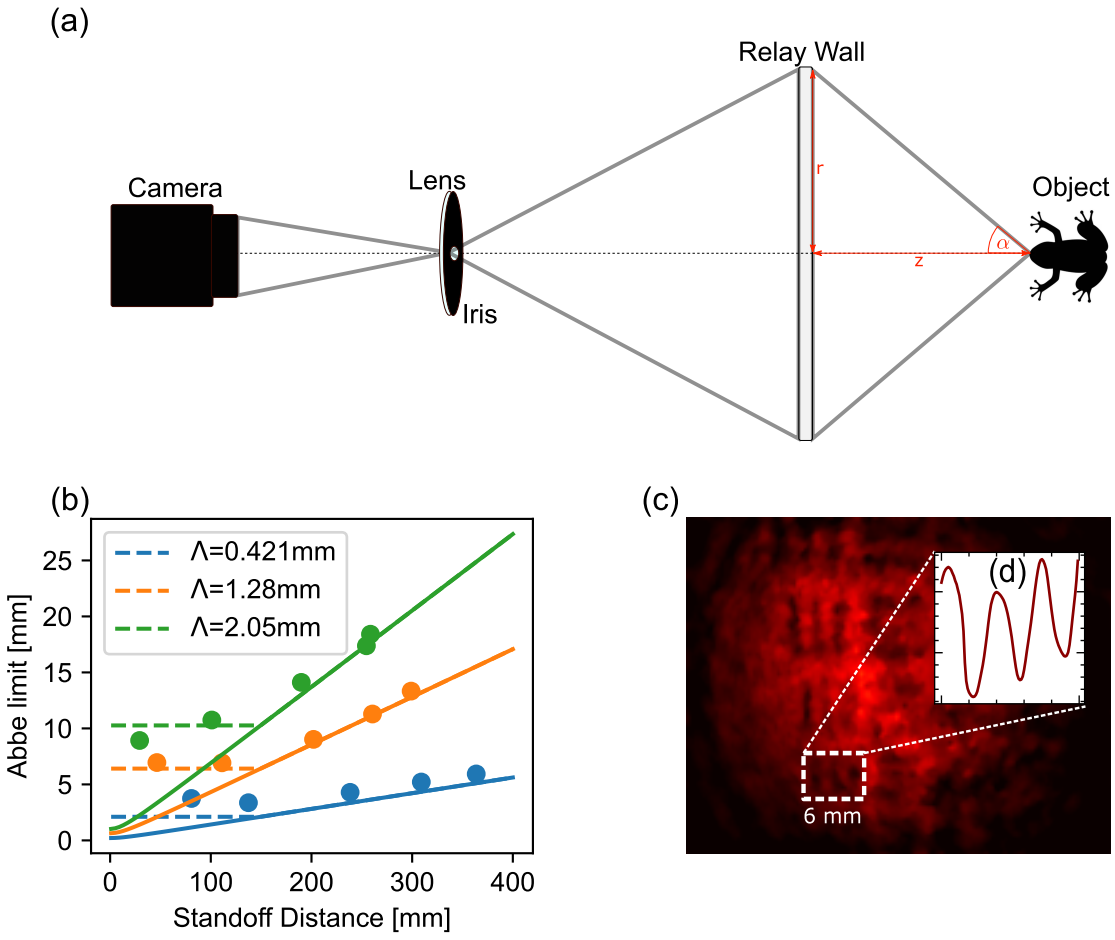

Figure 4.6: **Theoretical Diffraction Limit & Validation:** (a) The geometrical beam paths in the imaging setup. (b) The imaging size on the relay limits the NA in the first approximation. Measured diffraction disc size (dots) for an optical fibre and theoretical Abbe limit (line) as a function of numerical backpropagation distance. The dotted line in the plateau is due to the non-point-source-like properties of the fibre tip, which limits the NA due to restricted divergence. (c) Resolution limits at a USAF target, with an inset showing a 1D cutout.

Furthermore, to validate our theoretical resolution with an object experimentally, we utilize a United State Air Force (USAF) target, imaging different groups. The lowest resolution achieved corresponds to the USAF target group number -1, element 6, yielding a resolution power of 0.56

mm (0.891 lp/mm). The diffraction limit at a 15 mm standoff distance with a synthetic wavelength of 0.421 mm is approximately 0.3 mm, aligning reasonably well with our measurements.

Imaging of an Embedded Object within two Diffusers

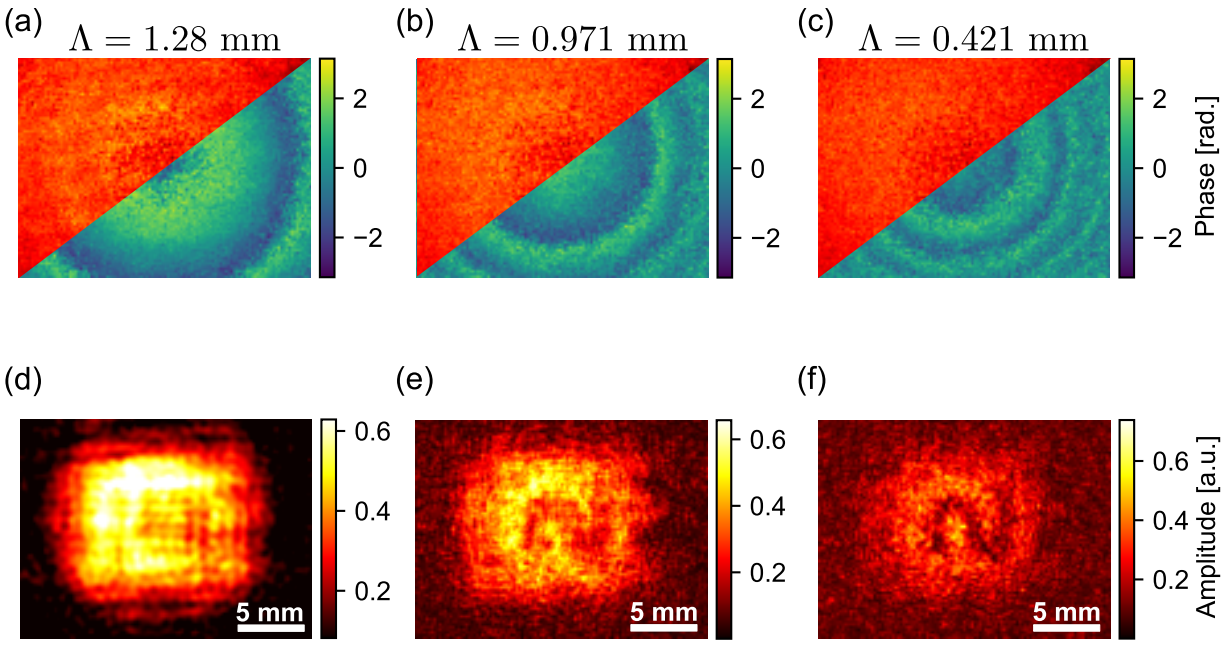

Figure 4.7: **Object Embedded Between Two Diffusers (Transmission)**: Reconstructed object using three different synthetic wavelengths (SWLs): $\Lambda = 0.421$ mm, 0.971 mm, and 1.28 mm. (a)-(c) Display the intensity (red-yellow) and phase (green-blue) for the synthetic wavelength hologram (SWH) measured at the face of the diffuser. The reconstructed objects are shown in (d)-(f). As expected, the large SWL exhibits minimal speckle artifacts but lacks the resolution necessary to reveal any significant details. In contrast, the shorter SWLs offer better resolution, though this comes at the cost of a lower signal-to-noise ratio (SNR) due to the presence of speckle artifacts.

Moving on to a more relevant case of ITSM, we investigate the scenario where two diffusers obscure the object: one on the illuminating side and one on the imaging side. First, we analyse the case where we measure an object sandwiched between two diffusers in transmission mode by back-illuminating the setup.

This configuration, shown in Fig. 4.5(a), consists of a transmission mode setup. An impinging laser beam is first scattered by a 220-grit diffuser, illuminates the object (which acts as a mask for the light field), and the transmitted light is then scattered again by a second 120-grit diffuser. We retrieved the SWH from three phase-steps with 1000 frames each. As the object, we used a USAF target, selecting (Group -2, Element 2) as our target. We compare three different synthetic

wavelengths: $\Lambda_1 = 0.421\,\text{mm}$, $\Lambda_2 = 0.971\,\text{mm}$, and $\Lambda_3 = 1.28\,\text{mm}$. The measured SWHs are shown in Fig. 4.7(a)-(c). As observed, the amplitude remains mostly constant, while the phase carries the most information, displaying higher frequency fringes for smaller SWLs. As expected, the resolution increases with smaller SWLs, but speckle artefacts also become more pronounced. For Λ_3, the object is not recoverable due to the diffraction limit ($\delta_x \sim 1.5\,\text{mm}$). Λ_1 reveals sharper features of the object compared to Λ_2, but the noise increases significantly. This suggests that the choice of SWL is critical for achieving high-quality object reconstruction.

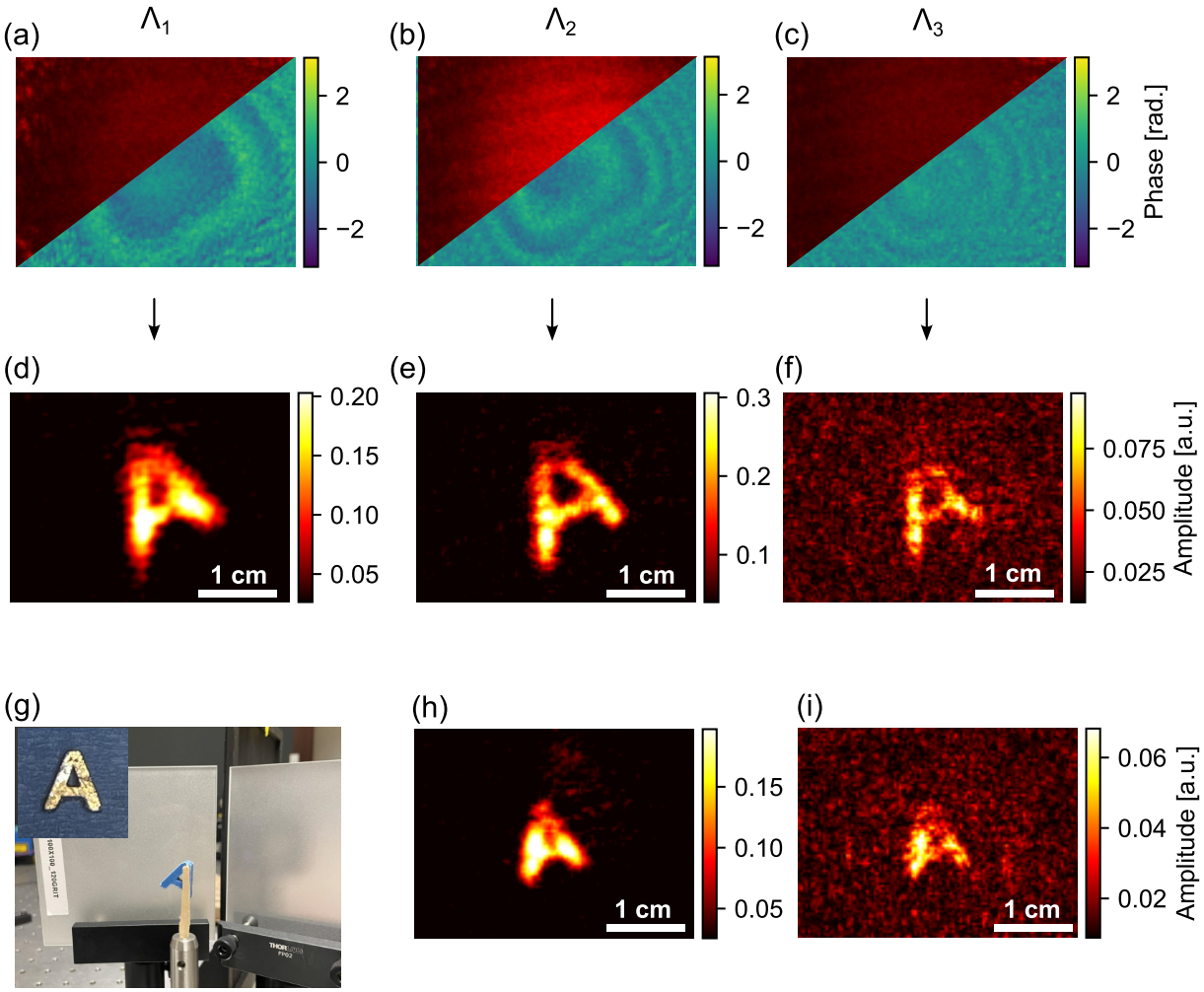

Figure 4.8: **Object Hidden Behind a Diffuser (Reflection)**: Reconstruction of an object hidden behind a diffuser in reflection. Two object sizes were used: An "A" with 11 mm (A11) and 15 mm (A15). For object A15, we present reconstructions using three different synthetic wavelengths ($\Lambda_1 = 0.421\,\text{mm}$, $\Lambda_2 = 0.971\,\text{mm}$, and $\Lambda_3 = 1.28\,\text{mm}$) in (d)-(f) with the corresponding SWHs in (a-c). For object A11, reconstructions using two different SWLs (Λ_2,Λ_3) are shown in (h)-(i), as the largest SWL did not yield any visible reconstruction. An image of the imaging setup is given in (g) with an inset of the gold leaf covered object.

Furthermore, we demonstrated a second configuration in which the experiment was conducted in reflection mode. This setup, shown in Fig. 4.5(b), involves light being scattered by the

first diffuser, then backscattered or reflected by the object, followed by a third round of scattering before the light reaches the camera. Since the USAF target acts as a mask, we needed an object that backscatters or reflects light. Therefore, we 3D-printed the letter "A" in various sizes. To enhance the backscattered signal, we coated the 3D-printed object with a reflective surface, applying a layer of gold leaf to the object's surface, as shown in Fig. 4.8(g). Again, we tested three different SWLs ($\Lambda_1, \Lambda_2, \Lambda_3$). We tested a larger "A" size of approximately 15 mm and a smaller size of roughly 11 mm. The measured SWHs for the larger "A" are shown in Fig. 4.8(a)-(c), and the reconstructions are displayed in Fig. 4.8(d)-(f). More detailed features are observed with smaller SWLs. We observe minimal speckle artefacts for Λ_1 and Λ_2, while Λ_3 introduces significant noise. Thus, Λ_2 is the preferred choice for this object. However, when attempting to reconstruct the smaller "A" (see Fig. 4.8(h)-(i)), Λ_2 is unable to resolve all the features, making Λ_3 the better choice, despite the increased noise, for fully resolving the object.

Comparing the transmission and reflection measurements, a noticeable difference in reconstruction quality emerges. Although the diffraction limit is fundamentally the same, the noise level is distinctly lower in the reflection case. One reason for this is that the object in the reflection setup is more sparse; we primarily collect light reflected from the object itself. In the transmission case, we observe a larger field, as the object merely masks a portion of it. The sparse field in the reflection case simplifies backpropagation and yields a cleaner propagated field.

Imaging through Volume Scatterer

Imaging through two diffusers typically involves scattering across two discrete planes. However, in this work, we extend the applicability of our technique to imaging through volume scatterers (VS), where scattering occurs continuously throughout the volume. These volume scatterers are prepared by mixing epoxy resin with varying concentrations of TiO_2, depending on the desired scattering strength, and then allowing the mixture to cure overnight [115, 116]. For our experiments, we used two bulk scatterers: one with a thickness of 1.5 cm (VS I) containing a lower concentration of TiO_2, and the second with a thickness of 0.8 cm (VS II), which had a higher concentration of TiO_2. A visual depiction of the setup is provided in Fig.4.9(a). To create a precise reference plane for measuring the hologram, a sheet of paper was glued onto VS I as a projection surface.

In the first configuration, VS I is placed in front of the camera, obscuring an object behind it. The object is directly illuminated from the back, as shown in Fig.4.9(b). The selected object is a 15x15 mm 3D-printed letter "G" as depicted in Fig.4.9(a). Given the scattering strength and the object size, we determined an appropriate synthetic wavelength based on Eq. (4.5) and the diffraction limit, which required selecting a synthetic wavelength larger than that used for the

two-diffuser case.

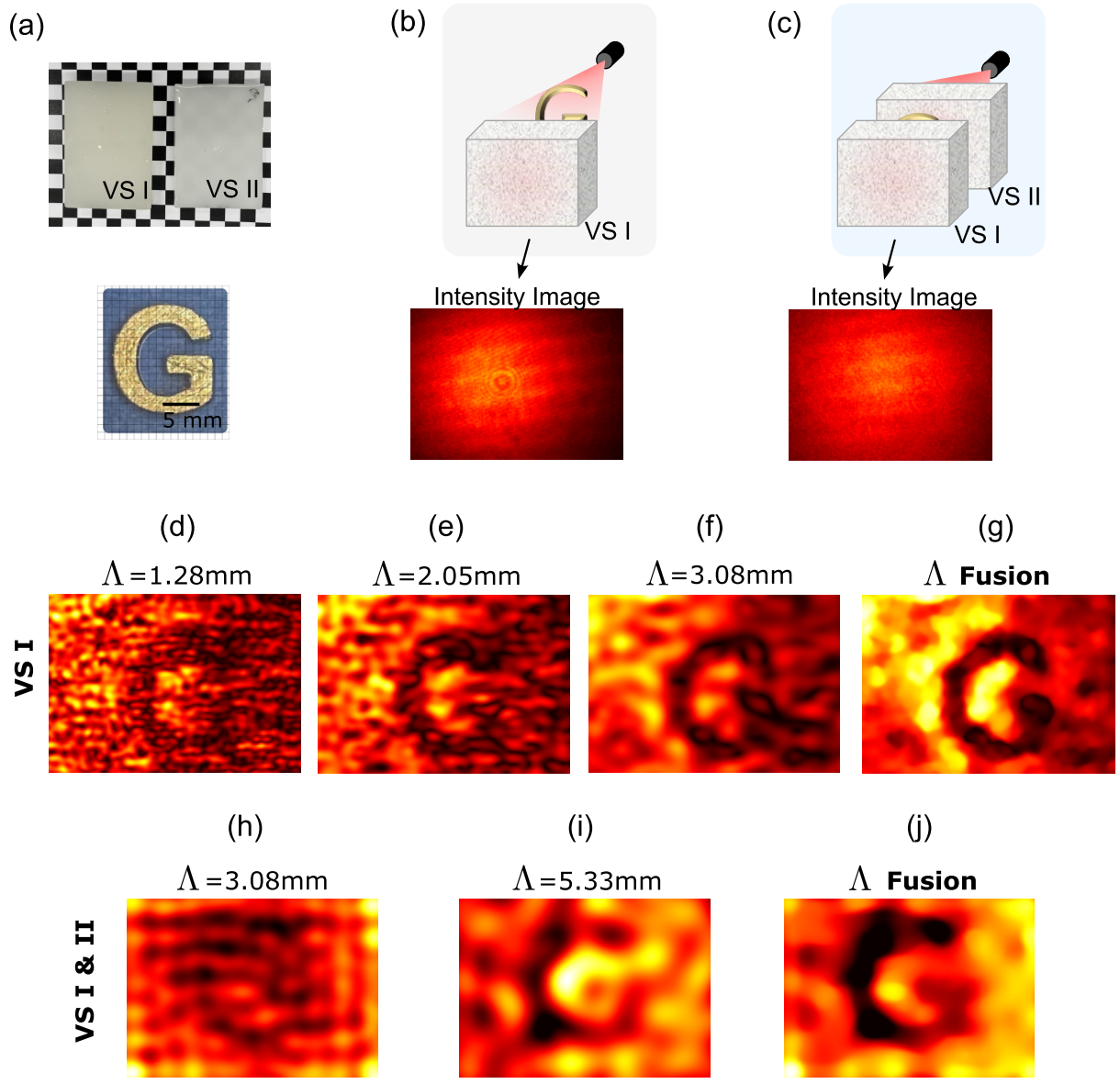

Figure 4.9: **Imaging through volume scatterer**: (a) Image of the two volume scatterers (VS I & VS II) placed directly on top of a chequerboard to visualize the extent of scattering and a photo of the hidden object: a 3D printed letter G. (b) Schematic of the experimental configuration with a single layer of volume scatterer and the corresponding intensity image. (c) Experimental configuration schematic for the case of the target sandwiched between volume scatterers. For a single VS: (d-f) Amplitude of the backpropagated hologram when imaging is done using synthetic wavelengths of $\Lambda = 1.28$mm, $\Lambda = 2.05$mm, and $\Lambda = 3.08$mm, respectively.(i) Amplitude of the reconstructed field via optimization, using data from the three synthetic wavelengths. For two VS: (h, i) Amplitude of the backpropagated hologram when imaging is done using synthetic wavelengths of $\Lambda = 3.08$mm and $\Lambda = 5.33$mm, respectively. (j) Amplitude of the field reconstructed via optimization using data from the two synthetic wavelengths.

We reconstructed the SWH using three different synthetic wavelengths: $\Lambda = 1.28$ mm, 2.05 mm, and 3.08 mm. Figs.4.9(d)-(f) display the backpropagated reconstructions at the standoff distance for each respective synthetic wavelength. As observed in previous studies, reconstructions with smaller synthetic wavelengths reveal sharper object features, but these come at the cost of increased speckle artefacts. Conversely, larger synthetic wavelengths produce smoother images, albeit with less detail. Due to the significant thickness of VS I, even at the largest wavelength, the reconstructions from numerical backpropagation are heavily affected by scattering, as shown in Fig.4.9(f).

To improve the reconstructions, we applied convex optimization techniques (discussed in section 4.2.2), combining data from all three synthetic wavelengths. This approach aims to integrate the fine detail from shorter wavelengths with the improved signal-to-noise ratio (SNR) provided by larger wavelengths. The result of this optimization is shown in Fig.4.9(g), where the fused reconstruction clearly demonstrates sharper object features compared to simple numerical backpropagation.

In the second configuration, we tackle a more challenging scenario where the object is embedded between two scattering layers: VS I in front of the camera and VS II on the illumination side, as illustrated in Fig.4.9(c). Before reaching the object, the illuminating light is already dispersed by VS II, resulting in increased scattering. To counter this, longer synthetic wavelengths are required. The reconstructions using numerical backpropagation for two different synthetic wavelengths are shown in Figs.4.9(h)-(i). As expected, sharper features are obtained with smaller wavelengths, while larger wavelengths yield coarser features. A comparison between the single-scatterer case (Fig.4.9(f)) and the two-scatterer case (Fig.4.9(h)) reveals that the increased scattering makes the reconstruction significantly more challenging.

Even at larger synthetic wavelengths, the object features in the two-layer case become progressively less resolved, indicating that we are approaching the resolution limit. However, combining the data from multiple synthetic wavelengths through optimization (Fig.4.9(j)) still provides a more refined reconstruction, demonstrating the robustness of our algorithmic approach in retrieving object information under severe scattering conditions.

In conclusion, our results emphasize that the choice of synthetic wavelength is critical for achieving high-quality reconstructions. It is advisable to use the smallest possible wavelength that remains robust against the scattering in the system. Additionally, our multispectral approach demonstrates that combining data from multiple wavelengths can mitigate some of the limitations posed by scattering, allowing for a balance between resolution and robustness.

Imaging through a Dynamically Changing Medium

We have demonstrated that this technique is applicable in strong scattering scenarios; however, our previous experiments were limited to static cases. Imaging through dynamic scattering media is crucial across many real-world applications, including medical diagnostics (e.g. imaging through biological tissues) and remote sensing through turbulent atmospheric conditions. In such scenarios, continuous changes in the scattering medium disrupt conventional imaging techniques, which rely on a static interaction between light and the medium and must acquire data faster than the decorrelation time of the dynamic medium. These changes introduce unpredictable distortions, making clear image capture particularly difficult.

We demonstrate that our technique remains applicable in dynamic scattering scenarios due to its inherent robustness to phase noise. In fact, we can exploit the phase randomization induced by the dynamic scattering in our $g^{(2)}$ SWH hologram generation. This unexpectedly enhances our method and simplifies the experimental setup, as we no longer need to use the piezo stage for phase randomization. The dynamic phase randomization caused by the scattering process itself acts as a natural scrambler, eliminating the need for additional components. Furthermore, rapid changes in the medium, which typically hinder other methods due to insufficient light capture, pose no issue for us. Our acquisition time can be arbitrarily long, far exceeding the decorrelation time, without degrading image quality.

To demonstrate these capabilities, we mimicked dynamic scattering in our experimental setup. Using a similar transmission setup to the static two-diffuser case described in Section 4.3.2, we removed the piezo stage from the reference arm and instead mounted the imaging-side diffuser on a lateral motion stage. The whole diffuser was randomly moved between frame acquisitions, with a total movement range approximately equal to the speckle size. We used the USAF target as the object, focusing on group -2, elements 3 and 5. The resulting intensity images are shown in Fig. 4.10(b, e), and the generated SWHs are provided in Fig. 4.10(c, f). Final reconstructions from the back-propagated fields are shown in Fig. 4.10(d, g).

As shown in the reconstructions, not only was the object successfully imaged, but there was also a significant reduction in speckle artefacts compared to the static case. This reduction is attributed to the averaging effect of the phase randomization, which smooths out speckle patterns. This result highlights the robustness and utility of our method in dynamically scattering environments, where traditional methods would struggle with the rapid changes in the medium.

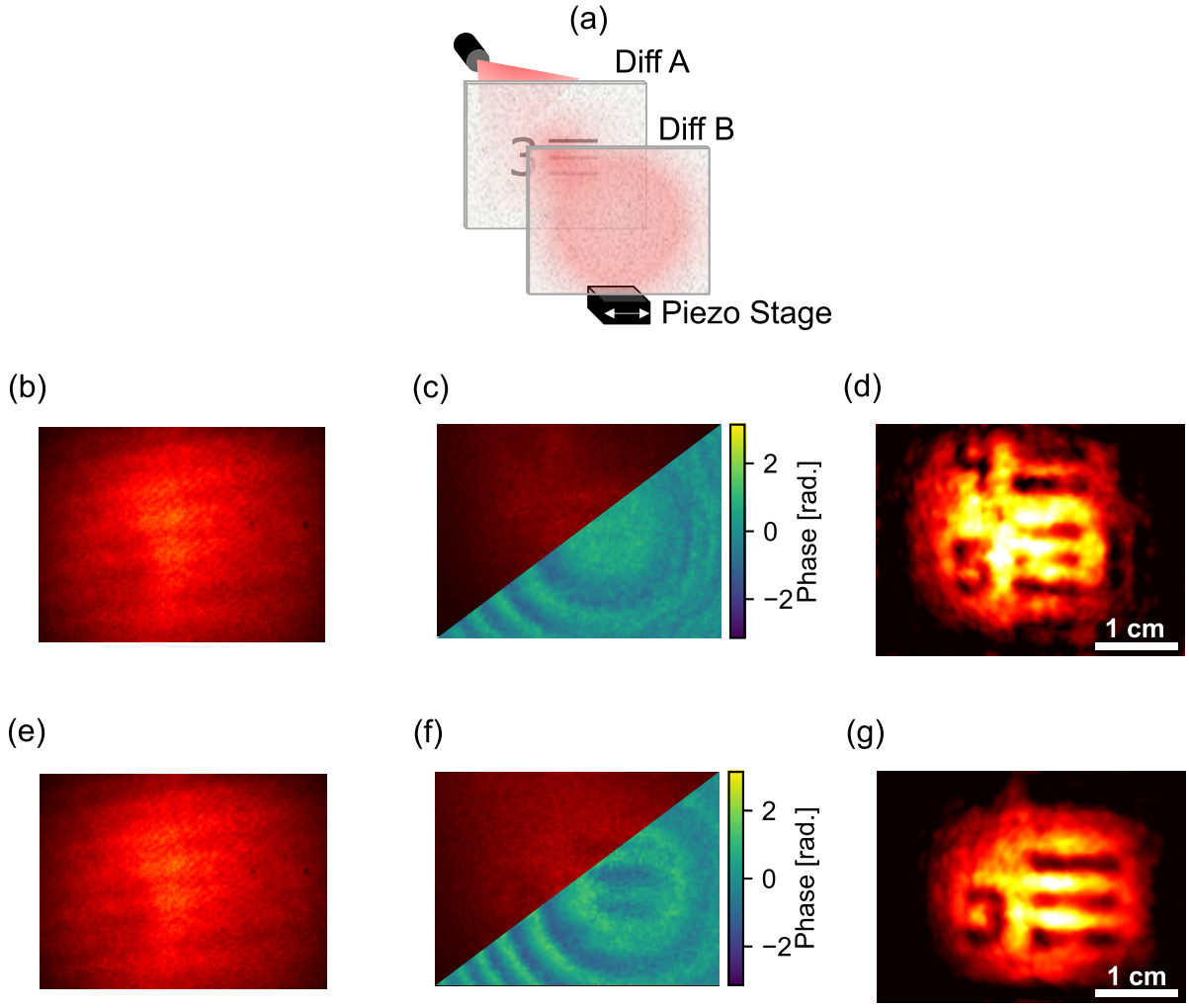

Figure 4.10: **Imaging through a dynamically changing scatterer**: (a) Schematic of the problem, where Diffuser B is randomly moved using a piezo stage. (b) & (e) Intensity images captured with a conventional camera. (c) & (f) Phase (blue-green) and amplitude (red) profiles from the SWL hologram at the surface of the diffuser. (d) & (g) Optimized amplitude of the backpropagated SWL hologram.

Optimisation Comparison

In this section, we analyse how the iterative optimization algorithm improves image reconstruction compared to basic backpropagation across three scenarios: transmission through two diffusers, reflection from two diffusers, and imaging through bulk scatterers.

In the case of two-diffuser transmission Fig. 4.11(a), the optimization yields the most significant improvements. The initial reconstruction contains substantial noise, which obscures the finer details of the object. After applying the optimization, we observe a marked reduction in

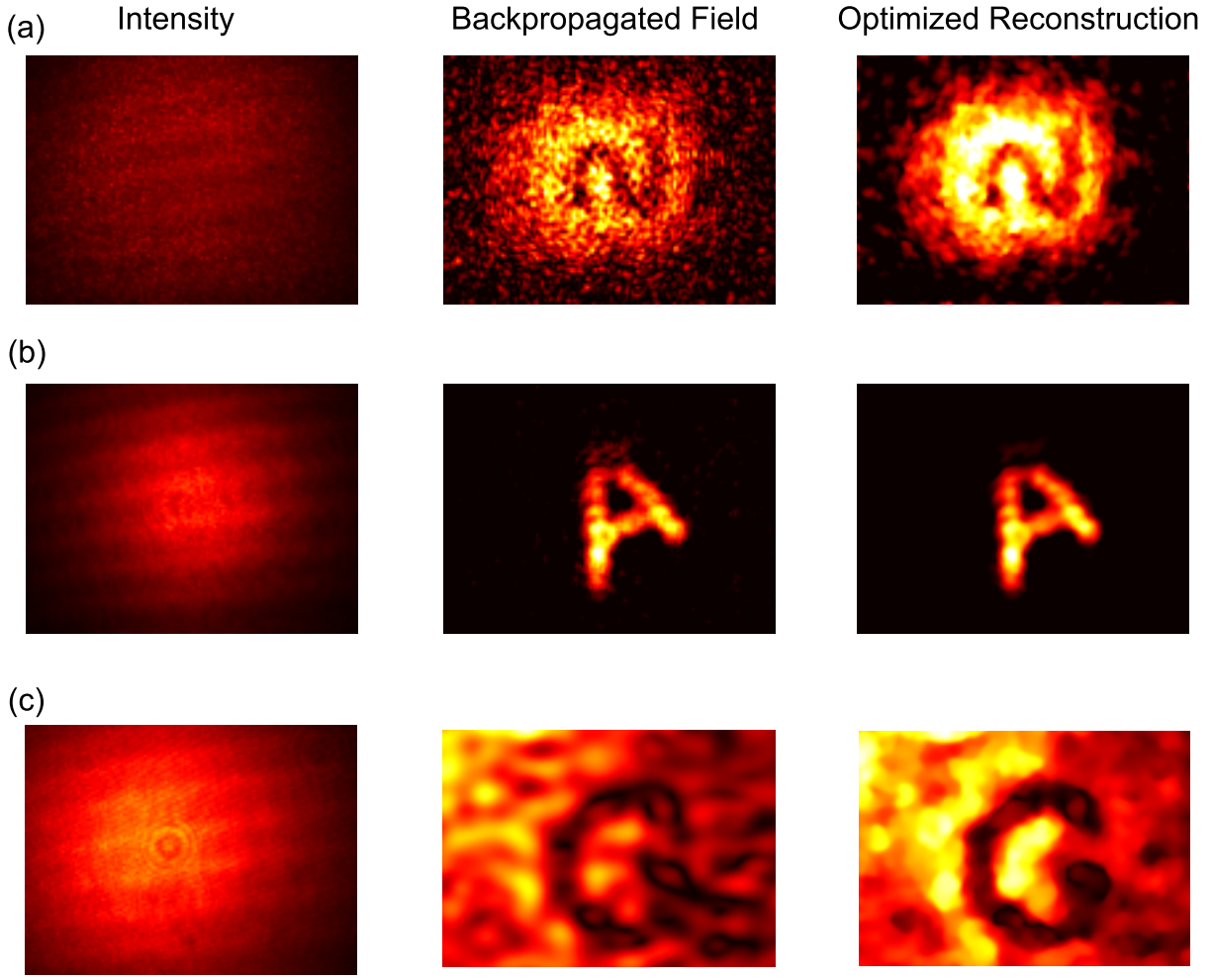

Figure 4.11: **Optimised Reconstruction Algorithm Results**: Comparison between the optimized reconstruction and basic backpropagation. (a) Shows the reconstruction for the two-diffuser transmission case, where the noise reduction and contrast enhancement are clearly visible. (b) In the reflection case, although the initial reconstruction has low noise, the optimization smooths the result but also removes parts of the object (e.g., the top of the letter "A"). (c) The optimization yields significant improvement in low SNR scenarios, such as imaging through bulk scatterers, especially when using multispectral inputs.

noise and a notable increase in contrast, making the reconstruction much clearer. For example, the previously noisy region around the number "2" is now more readable and distinct. This demonstrates the algorithm's effectiveness in situations where speckle noise is prevalent, such as in transmission through complex scattering media.

In the reflection case Fig. 4.11(b), the initial reconstruction starts with relatively low noise, so the optimization results in less noticeable improvements. While the algorithm smooths the image and slightly enhances contrast, it also leads to some loss of detail—evident in the upper

part of the letter "A" that becomes less defined. This highlights a potential trade-off between noise reduction and the preservation of fine details, particularly in scenarios with high initial signal quality.

Finally, the third case Fig. 4.11(c) involves imaging through bulk scatterers, where the signal-to-noise ratio (SNR) is low. Here, the optimization algorithm shows its greatest strength. By combining multispectral inputs, we observe a significant enhancement in both clarity and sharpness. The optimization not only reduces noise but also enhances the visibility of previously obscured features. This suggests that the algorithm is particularly well-suited for challenging low-SNR conditions, where traditional methods struggle to provide usable reconstructions.

Overall, the optimization algorithm provides substantial improvements in noise-heavy scenarios, such as transmission through diffusers or low-SNR environments, while showing more modest gains in reflection cases. Future work may explore the balance between noise reduction and detail preservation, especially in high-quality initial reconstructions.

4.4 Conclusion

In this work, we have introduced a novel method for generating synthetic wavelength holograms for ITSM, which significantly advances the field by utilizing intensity correlations to bypass the need for phase stability. This technique is particularly notable for its robustness against phase noise and background/stray light, an area where traditional methods often face limitations. Allowing this method to acquire over an extended time in the low-light conditions.

One of the standout features of our technique is its adaptability to dynamic scattering environments. Unlike conventional methods that require stable phase conditions and an acquisition time below the speckle decorrelation time, our approach leverages the phase scrambling introduced by dynamic scattering, allowing for effective light collection, fast SWH generation, and a simplified setup. This capability is particularly advantageous for biological imaging applications, where the scatterer, such as tissue or skin, inherently undergoes dynamic changes. The ability to operate effectively under these conditions positions our technique as a valuable tool for a wide range of practical imaging scenarios.

A key component of our technique's success is the use of multiple synthetic wavelengths in combination with the iterative reconstruction optimization. This multi-wavelength approach is critical for enhancing image reconstruction and detail preservation in highly scattering regime. By selecting an optimal set of synthetic wavelengths, we balance the trade-offs between scattering artefacts and resolution, achieving improved clarity and feature detection. Despite the

challenges inherent in performing quantitative analysis for unsupervised images, our qualitative results affirm the effectiveness of this method in producing high-quality reconstructions.

A critical comparison with other methods, such as holographic techniques for generating the SWH, is important for fully evaluating the strengths of our approach. While our method utilizes intensity correlations and is not phase-sensitive, it lacks direct access to the optical fields, which holographic methods provide. Holographic methods measure both the amplitude and phase of the optical field, offering advantages like the ability to compute synthetic wavelengths from multiple optical wavelength bands and the ability to propagate the optical fields and then generate synthetic wavelengths at a chosen plane. This provides greater flexibility in the SWH generation. However, these benefits come with drawbacks, such as phase noise sensitivity and higher complexity—requiring equipment like AOMs and lock-in cameras to measure the optical hologram. Moreover, simpler holographic methods, such as off-axis holography, which can capture the hologram in a single shot, require measuring fringes within a speckle of the scattered field. This limits the aperture size, reduces light collection, and consequently necessitates longer exposure times. However, most benefits of holographic methods over $g^{(2)}$ may not be as critical for the practical implementation of the technique, and I believe the drawbacks outweigh them.

However, there are several challenges that remain to be addressed. There is a growing interest towards NLOS videography [84, 117]. One significant goal is to achieve single-shot imaging, as the current requirement for multiple phase-steps can limit the technique's practicality. Additionally, the resolution is constrained by the large synthetic wavelength, which affects the level of detail in the reconstructed images. Future work will focus on overcoming these limitations by advancing towards single-shot capabilities and refining on the computational model with a wider synthetic spectrum to improve the resolution even further.

Further exploration of the method's performance in highly relevant, high-scattering, and dynamically changing scenarios, particularly in medical imaging applications, will be crucial for evaluating and improving its effectiveness. The key limitation to address is the method's ability to maintain precision and robustness in real-world, complex environments where scattering and motion are more prominent, potentially affecting signal quality and resolution. Identifying these boundaries will help refine the approach for broader, more practical use cases.

Overall, our approach represents a significant advancement in synthetic wavelength holography, offering a robust and versatile solution for imaging through complex scattering environments. The technique's ability to handle dynamic changes and its potential applications in medical imaging underscore its promise for future research and development. As we continue to refine and expand the capabilities of this method, it holds the potential to make a substantial impact in fields that require high-resolution imaging through challenging and dynamic scattering media.

Chapter 5.

Dual Comb Intensity Correlation

In previous chapters, we have discussed the limitations of our interferometric technique, particularly in imaging macroscopic objects within typical environments. These limitations are primarily due to the need for a long, mechanically scanned optical delay, which introduces challenges in terms of alignment and practicality. To overcome these obstacles, we propose utilizing a dual-comb laser system, which enables optical delay scanning without mechanical movement. This innovative approach eliminates the need for mechanical scanning and transfers the scanning to the time domain, offering greater flexibility and dynamic scanning capabilities.

In this chapter, we explore the application of dual-comb lasers for generating $g^{(2)}$ correlation measurements across various scenarios. Our method allows for high-speed, precise sensing at single points rather than traditional imaging. This transition to dual-comb sensing enhances both the speed and flexibility of our measurements, enabling the efficient extraction of information from complex scenes. The experiments described in this chapter were conducted in collaboration with Shu-Wei Huang and Neeraj Prakash at the University of Colorado Boulder.

5.1 Frequency-Comb Lasers

Single-Frequency-Comb System

The other half of the Nobel Prize that was awarded to Glauber in 2005, as described in Section 2.3, was granted to John L. Hall and Theodor W. Hänsch "for their contributions to the development of laser-based precision spectroscopy, including the optical frequency comb technique." These frequency comb lasers represent a revolutionary development in laser technology, offering a unique combination of broad spectral coverage and precise frequency control. At its core, a frequency comb consists of an optical spectrum featuring a series of discrete, equally spaced frequency lines, resembling the teeth of a comb, as illustrated in Fig. 5.1. The frequency comb is characterized by two fundamental parameters: the repetition rate f_{rep}, which determines the spacing between the comb lines, and the carrier-envelope offset frequency f_0, which defines the absolute position of the comb lines. Frequency combs can span remarkably broad spectral ranges, sometimes covering an octave (a factor of two) or more, which enables a wide array of applications. One of the most significant features of frequency combs is their ability to serve as optical frequency rulers, providing a direct and precise link between optical and microwave fre-

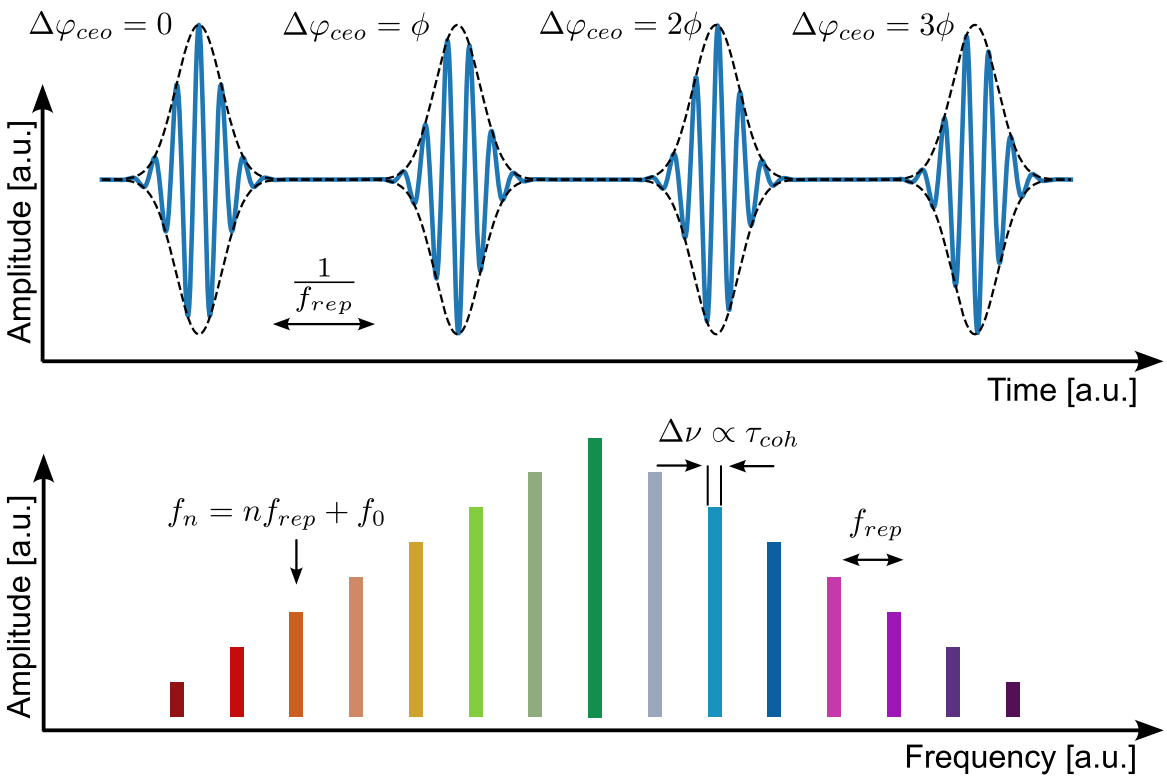

Figure 5.1: **Single Frequency Comb Laser:** Schematic representation of the frequency comb laser in both time and frequency domains. In the time domain (top), the pulses exhibit a carrier and an envelope, where the carrier-envelope phase $\Delta\varphi$ shifts between consecutive pulses. The pulse separation is defined by $1/f_{\text{rep}}$. In the frequency domain (bottom), the spectrum consists of discrete comb lines, each separated by f_{rep}, with an offset frequency f_0. The coherence time τ_{coh} of the laser is determined by the spectral linewidth $\Delta\nu$ of the individual modes.

quencies [118]. This capability has led to groundbreaking applications in metrology, including the development of optical atomic clocks that offer unparalleled accuracy in timekeeping [119]. Beyond timekeeping, frequency combs have found applications in high-precision spectroscopy, distance measurements, and telecommunications [120, 121, 122].

The distinctive spectral structure of frequency combs typically originates from mode-locked lasers producing ultrashort pulses, where the comb emerges as a Fourier transform of the periodic pulse train . Mode-locked femtosecond lasers, such as solid-state Ti:sapphire, were the first to enable self-referenced frequency combs, offering broad bandwidths. Erbium-doped and ytterbium-doped fibre lasers, which operate in the 1.5-micron telecom band and around 1 micron, respectively, provide more compact and robust alternatives with high power and stability [123]. The repetition rates typically start at 100 MHz and can go up to 10 GHz [124, 125]. Instead of mode-locking, frequency combs can also be generated by four-wave mixing in a photonic-crystal fibre by pumping with two-high power lasers [126]. In recent years, microresonator-based Kerr

combs have attracted significant attention. These systems uses the Kerr nonlinearity in high-Q microresonators to generate combs with very high repetition rates (10-1000 GHz) in a compact form [127]. Furthermore, electro-optic comb generators, which modulate a single-frequency laser to create sidebands, offer wide and agile tuning of mode spacing [128]. Each method offers distinct advantages in spectral coverage, repetition rate, and power, catering to a diverse range of scientific and technological needs.

Dual-Frequency-Comb System

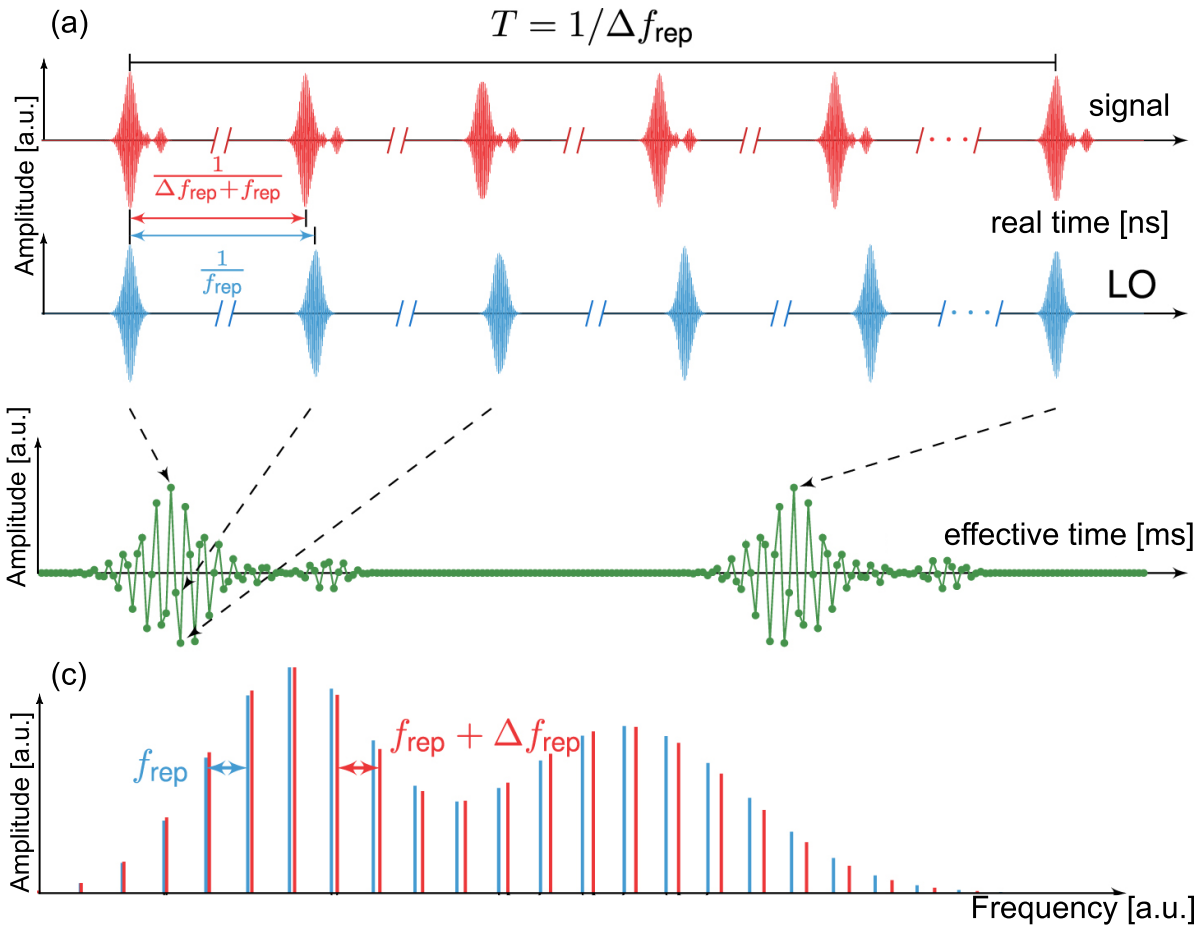

Figure 5.2: **Dual Frequency Comb Laser:** Schematic illustration of the working principles in both the time and frequency domains. (a) Time traces of two frequency combs (red and blue) with slightly different repetition rates (f_{r1} and f_{r2}), depicted in real time. (b) The resulting interferogram from the interference of the two combs, now measured in an effective time domain defined by the difference in repetition rates (f_{r1} and f_{r2}). (c) The spectra of the two combs, which exhibit different line spacings due to their differing repetition rates. Image adapted from [129]

Dual-frequency-comb systems utilize two optical frequency combs with slightly different repetition rates, which can achieve asynchronous optical sampling without mechanical motion scan-

ning, enabling high-resolution, broadband spectroscopy and metrology. As shown in Fig. 5.2, the combs are detuned by a small repetition frequency difference, Δf_{rep}, resulting in a time-domain scan at a rate of exactly Δf_{rep}. However, using two separate mode-locked and stabilized systems is bulky, costly, and complex to operate. Furthermore, mutual coherence of two combs, instead of frequency stabilities of each comb, is now the most critical factor affecting the dual-comb performance.

As a result, recent efforts have focused on developing a single cavity laser system capable of generating two mutually coherent optical frequency combs with slightly different repetition rates [130]. A universal approach to achieve stable asynchronous ultrashort pulse was proposed by introducing the concept of "multiplexing" into the field of ultrafast laser. In such a Multiplexed Mode-Locked Laser, the cavity is designed to allow the simultaneous oscillation of pulses with different characteristics in one of the propagation dimensions. In the following years, numerous single-cavity dual-comb lasers and dual-comb systems based on them have been achieved, and so far they can still be categorized into the following four categories: wavelength-multiplexed, polarization-multiplexed, direction-multiplexed, and pulseshape-multiplexed lasers corresponding to the four dimensions of light propagation [123, 131].

A dual-comb laser system is characterized by three primary parameters: the repetition rate f_{rep}, the repetition rate difference Δf_{rep}, and the spectral bandwidth $\Delta \nu_{\mathrm{comb}}$. Together, these parameters govern the scanning properties of the laser.

The maximum unambiguous scanning range is determined by the repetition rate. Specifically, we can express the maximum detectable unambiguous range, d_{max}, as a function of the repetition rate difference:

$$d_{\mathrm{max}} = \frac{c}{2\Delta f_{\mathrm{rep}}}, \tag{5.1}$$

where c is the speed of light. For a repetition rate of $f_{\mathrm{rep}} = 10\,\mathrm{MHz}$, the unambiguous range is approximately 60 meters, while for $f_{\mathrm{rep}} = 10\,\mathrm{GHz}$, it reduces to around 60 millimetres.

Dual-comb scanning refers to the scanning of the pulse trains from two dual combs over each other, translating the optical scanning process from physical time to an effective scan time. This introduces a time magnification factor m, defined as:

$$m = \frac{f_{\mathrm{rep}}}{\Delta f_{\mathrm{rep}}}, \tag{5.2}$$

where m represents the magnification from real time to effective scan time.

The sampling interval of the dual-comb laser, which defines the optical step size between successive pulses, is given by:

$$\Delta T_{\text{step}} = \frac{\Delta f_{\text{rep}}}{f_{\text{rep},1} \cdot f_{\text{rep},2}}, \tag{5.3}$$

In addition, the Nyquist sampling criterion imposes a relationship on the system, ensuring that the comb spacing satisfies the following condition:

$$\Delta \nu_{\text{comb}} < \frac{f_{\text{rep},1} \cdot f_{\text{rep},2}}{2\Delta f_{\text{rep}}}. \tag{5.4}$$

These parameters must be carefully selected based on the specific application or problem being investigated. There are inherent trade-offs between three key factors: range, resolution, and speed. Only two of these can be optimized at a time. For instance, GHz-range dual-comb lasers can achieve high resolution and speed but are limited in range, while MHz-range systems offer a larger range but require a compromise between resolution and speed.

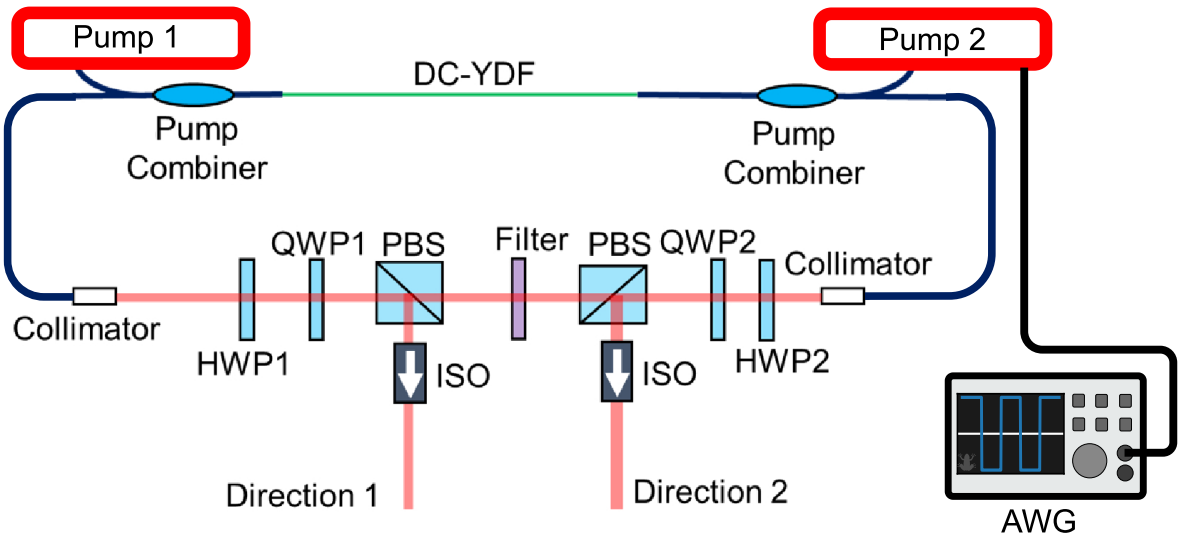

Figure 5.3: **CANDi:** Schematic of the fiber-based counter-propagating all-dispersion dual comb laser. Two pumps are used, each injecting power from opposite directions to generate the dual combs. Each comb has its own output, with optical isolators (ISO) placed to prevent back reflections. Additionally, an AWG is connected to one of the pumps to enable dynamic tuning of the laser. Key components: HWP – Half-Wave Plate, QWP – Quarter-Wave Plate, ISO – Optical Isolator, DC-YDF – Ytterbium-doped double clad fiber. Image adapted from [132]

In response to circumvent this limitations, researchers have been exploring novel approaches to dual-comb laser design. One significant advancement in this field is the **Counterpropagating All-Normal Dispersion (CANDi)** fiber laser [133]. Based on a bidirectional mode-locked oscillator in a ytterbium-doped fiber (Fig. 5.3), this system utilizes non-linear polarization rotation mode-locking to simultaneously mode-lock both directions. It demonstrates significant promise due to its cost-effectiveness, compact design, and environmental robustness. This laser is mode-locked through nonlinear polarization rotation and is bi-directionally pumped leading to a close to symmetric gain distribution. Its unique configuration ensures inherent common-mode noise rejection, significantly enhancing the system's stability without the need for complex external stabilization schemes. The all-normal dispersion cavity design contributes to high pulse energies and spectral flatness, breaking through previous energy limitations in dual-comb systems. Recent advancement in the CANDi have achieved pulse energies of up to 8 nJ for each comb [132]. This increased pulse energy opens up new possibilities for various nonlinear dual-comb applications, such as Raman spectroscopy and THz spectroscopy, which require higher peak powers. Additionally, the CANDi laser with a repetition rate of 48 MHz offers a tunable repetition rate difference 0.1 Hz to 100 Hz, providing flexibility for a wide range of applications. Recent characterizations of the CANDi have shown a relative timing jitter of 39 fs (integrated from 1 kHz to 20 MHz), primarily limited by pump Relative Intenstiy Noise (RIN). The laser produces flat, broadband spectra in both propagation directions, contributing to its versatility in spectroscopic applications. Ongoing research aims to further improve the CANDi laser's performance. Current efforts focus on reducing intensity-dependent spectral shifts, optimizing cavity symmetry, implementing narrower spectral filters, and improving pump laser RIN characteristics. These enhancements are expected to further reduce relative timing jitter and improve overall system performance [132].

The key advantage of the CANDi system, and one of its most compelling features, is its unique dynamic tuning capability, which is vital for applications requiring adaptable dual-comb sources. This feature breaks the measurement speed-time resolution trade-off, allowing to achieve higher scan rates while maintaining high resolution [134]. The dynamic tuning is possible by tuning the pump power of one of the lasers as illustrated in Fig. 5.3. The main mechanism that is coupling pump power and repetition rate is the asymmetric response of the two directions of the respective combs to pump-power directions, inherited from the non-identical centre frequency change coupled with the interactivity group delay dispersion [132, 134, 133]. Experimental results show that the dynamic Δf_{rep} modulation does not introduce excessive relative timing jitter. The maximum tuning bandwidth of the Dynamically Tuned Counterpropagating All-Normal Dispersion (DCANDi) laser is up to 10 kHz and is inherently limited by the laser response bandwidth. This combination of tunable repetition rate difference and low relative timing jitter makes the DCANDi laser an exceptionally versatile tool for applications requiring adaptable yet highly stable dual-comb sources.

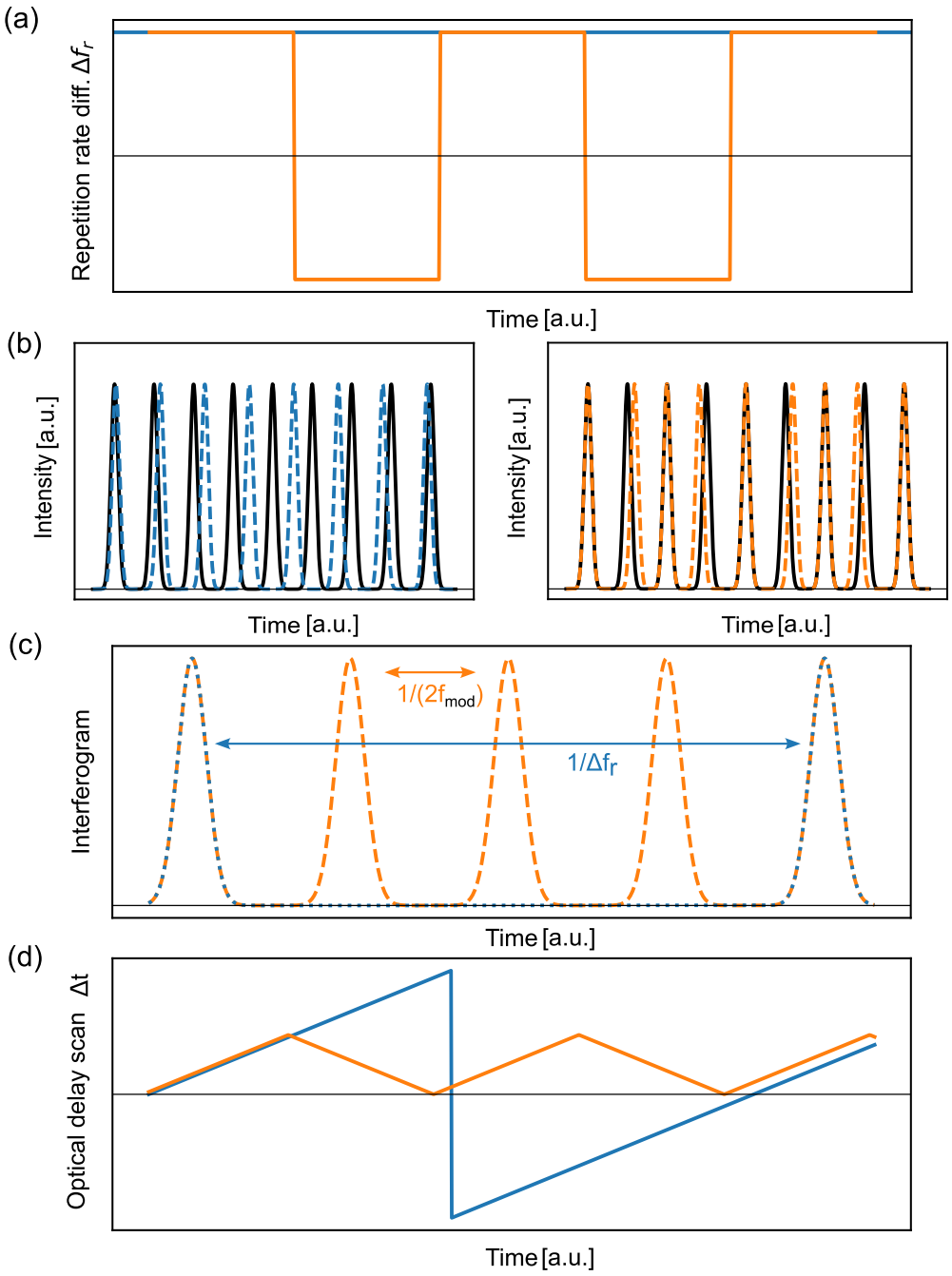

Figure 5.4: **CANDi Scanning Types:** Schematic of the linear (blue) and dynamic (orange) scan operation modes of the dual comb laser system. (a) The repetition rate difference Δf_{rep} as a function of time. In the linear case, Δf_{rep} remains constant, while in the dynamic case, it alternates between positive and negative values. (b) Time traces for the linear scan (blue) show gradual, unidirectional scanning between the two combs, whereas the dynamic scan (orange) shows bidirectional scanning, moving back and forth within the region of interest. (c) The interferogram shows that the spacing between successive interferograms (IGMs) is determined by Δf_{rep}, with the dynamic scan being modulated by the switching frequency. (d) The effective optical delay scan: the linear scan performs a complete scan, wrapping around and restarting, while the dynamic scan oscillates back and forth within the same delay region Δt.

The main way to use this capability of the DCANDi is to tune Δf_{rep} in such a manner to reverse the sign of Δf_{rep} in the negative. A negative Δf_{rep} means an effective scanning into the other direction. By setting the tuning in a symmetric and balanced manner we can scan the optical delay between the two combs back and forth over a region of interest. This method enables scan rates of up to 20 kHz, while maintaining a timing resolution as precise as $\Delta T_{\text{step}} = 0.4\,\text{fs}$ for a $\Delta f_{rep} = 1\,\text{Hz}$. A schematic comparison between linear and dynamic scanning, shown in Fig. 5.4, highlights how this approach allows rapid scanning across a small region of interest over a large range. The key point is that the scan rate is now defined as $\frac{1}{2f_{\text{mod}}}$, where f_{mod} represents the dynamic tuning modulation frequency, in contrast to the linear case where it was defined as $\frac{1}{\Delta f_r}$.

Dual Frequency Comb Laser Applications

The applications of dual-comb lasers are similar as those for single frequency combs but can be highlighted in two fields: Spectroscopy and distance measurements.

Dual-Comb Spectroscopy: Dual-comb spectroscopy utilizes two coherent frequency combs to measure a sample's spectral response on a tooth-by-tooth basis, offering rapid analysis without the size constraints or instrument limitations of traditional spectrometers. The concept involves generating a Radio Frequency (RF) spectrum by heterodyning two frequency combs with slightly different repetition rates. The resulting RF comb consists of distinguishable beats between pairs of optical comb teeth. By directing one comb through the sample, interfering the output with the second comb, and measuring the beat notes, we can deduce the transmission of each spectral band through the sample simply by Fourier-transforming the signal. This is effectively a Fourier-transform interferometer [135], with the key difference that the signals are shifted from the optical domain to the RF domain [136, 121, 137]. In spectroscopy, they enable rapid, high-resolution measurements of molecular absorption spectra, making them valuable tools for gas sensing, atmospheric monitoring, and chemical analysis.

Dual-Comb Distance Measurement (LiDAR): Dual-comb lasers can be used in high-precision distance measurement applications. The key advantage of dual-comb systems is that they enable high-precision interferometric, $g^{(2)}$, or non-linear light detection methods without the need for a mechanically scanned interferometer [138, 139]. In macroscopic imaging scenarios, such as LiDAR, traditional systems would require a mechanical translation stage several meters long to scan the delay between pulses—an impractical and cumbersome solution. By contrast, dual-comb lasers inherently handle this scanning, allowing for distance measurements with sub-micrometer precision over large ranges. This makes them highly effective for applications in aerospace, NLOS, construction, and geospatial mapping, where precise timing information from

frequency combs enables accurate ranging and 3D imaging. [140].

5.2 Methodology

As previously discussed, dual-comb systems are powerful tools for Time-of-Flight (ToF) measurements, eliminating the need for mechanically scanned interferometers. Traditionally, these systems have been used in conjunction with non-linear detection methods [138] or phase-sensitive interferometric methods [141]. In this chapter, we demonstrate that instead of using a non-linear crystal to measure the temporal overlap between the two combs, we utilize a simple beamsplitter and analyse intensity correlations ($g^{(2)}$), as discussed in Chapter 2. This novel approach provides a phase-noise-robust method for dual-comb ranging, without the need for optical non-linearity.

Experimental Setup

The proof-of-principle experiment for generating the intensity correlation or $g^{(2)}$ peak using the dual-comb laser system illustrated in Fig. 5.5 can be broken down into two main parts: the trigger setup and the sensing setup. In the laser system (configured as in [134]), two closely spaced and aligned comb outputs are generated. The two combs have a bandwidth of 30 nm, are compressed using gratings to around 180 fs and have pulse energy of around 1.7 nJ.

A small portion of the light is split off using a low reflection beam sampler, and further divided into two paths. One of these paths includes a manual translation stage with a retroreflector. The two beams are then recombined at a beamsplitter, forming a Mach-Zehnder interferometer. The interference pattern is detected on a photodiode (Thorlabs PDA10CF). We then use this signal to trigger the experiment. This could be done straight on the Interferograms (IGMs), which would lead to large electronic jitter due to noise in the Carrier-Envelope Phase (φ_{CEO}). Hence, to generate a phase-insensitive trigger signal for the experiment, we reproduce the $g^{(2)}$ measurement in an analogue way. First, we apply a low-pass filter to the RF-signal to remove aliasing caused by the laser repetition rate. The signal is then split into two paths and fed into a frequency mixer, which multiplies the frequency spectrum of both signals—this acts as the intensity product described in Eq. (2.18):

$$g^{(2)}(t_1, t_2) = \frac{\langle I_1(t_1) I_2(t_2) \rangle}{\langle I_1(t_1) \rangle \langle I_2(t_2) \rangle}. \tag{2.18}$$

A second, much lower-frequency low-pass filter is applied to eliminate fringe components,

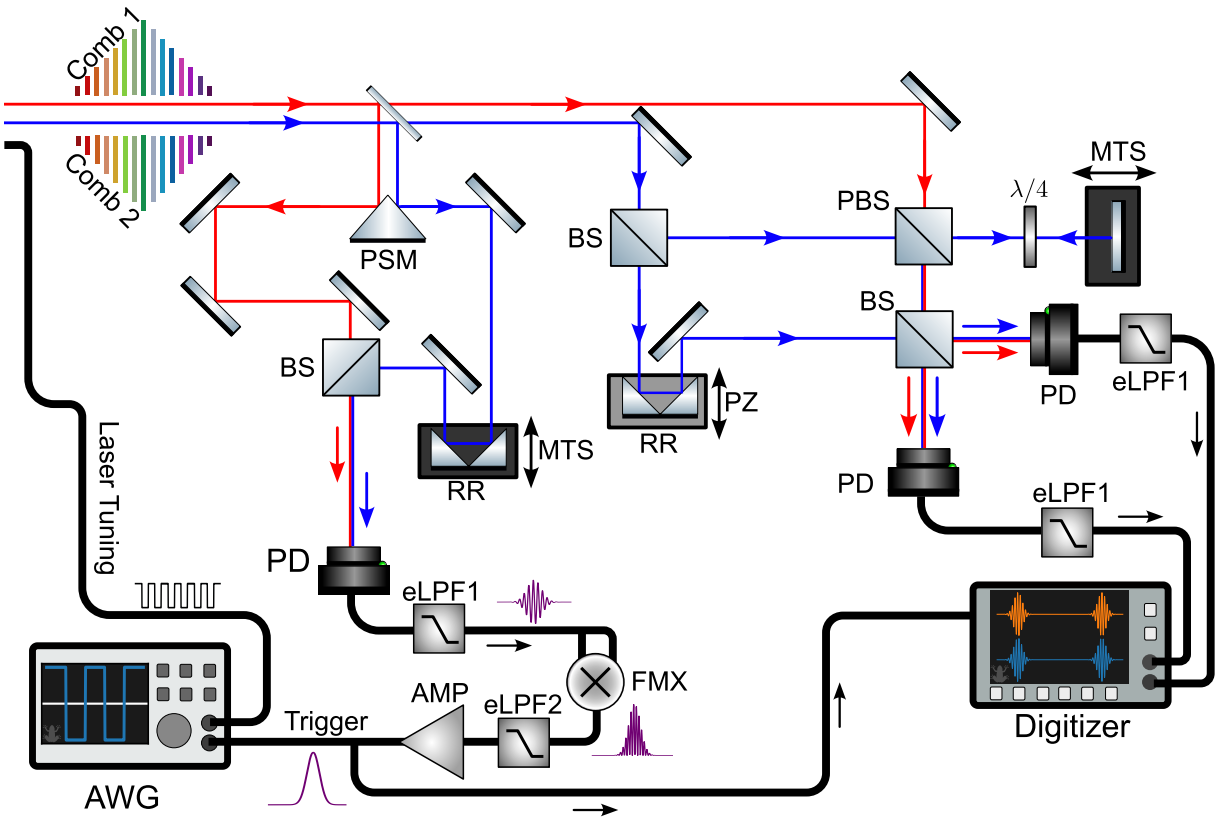

Figure 5.5: **DC Experimental Setup:** Experimental setup for generating second-order correlation measurements using a dual comb laser. The combs are first split to create a trigger signal for data acquisition, and then sent into an interferometer to measure the output signal at the beam splitter. Additionally, a reference signal option is included. For the trigger signal, the interference is detected by a photodiode (PD) and electronically processed to generate a trigger flank. Key components: eLPF – electronic low-pass filter, PD – photodiode, RR – retroreflector, FMX – frequency mixer, PZ – piezo stage, PSM – prism reflector, MTS – manual translation stage.

which acts like the ensemble average in Eq. (2.18). Finally, a digital amplifier is used to amplify the signal rising edge to +1.5 V, which is required as the minimal voltage for the electronic equipment. The signal is then send to the AWG that controls the scanning of the CANDi and to the digitizer acquiring the signal (AlazarTech ATS9371).

In the sensing setup, the light is passed through an interferometer, where it is split into a reference arm and a sample arm. The reference arm is transmitted through a polarizing beamsplitter (PBS) before arriving at the output beamsplitter (BS). In the sample arm, the light is further divided: One portion of the light, referred to as the copy signal, is first transmitted through the PBS and directed towards a mirror mounted on a Mechanical Translation Stage (MTS) to adjust its delay. Upon reflection, the signal passes through the PBS a second time and recombines with the reference arm. A $\lambda/4$ waveplate is placed between the mirror and the PBS, which converts the P-polarized light to S-polarization on the return path, ensuring the signal is reflected by the

PBS during recombination. The second portion of the sample arm is reflected by a retroreflector mounted on a piezo stage, which allows for precise control of the optical delay between the main and copy signals. All beams are then recombined at a final beamsplitter, and the outputs are detected using two photodiodes (Thorlabs APD110C). Each signal is passed through a DC block and two electronic low-pass filters before being digitized by an analogue-to-digital converter (ADC) card, which samples at a fixed rate of 200 MS/s. The advantage of using this setup, which includes the copy signal, is that it provides a timing reference crucial for the experiment. This copy signal recombines at the PBS with no losses and reaches the output beamsplitter through a single port. Consequently, the two exit ports of this beamsplitter will have the same phase for the copy signal, while the sample signal will exhibit opposing phases at the output. This phase difference means that when we perform a cross-correlation between the signals, the sample signal will produce a dip, whereas the copy signal will result in a peak, providing a clear and differential temporal reference for the measurement.

This setup enables us to generate and measure the $g^{(2)}$ peak, while maintaining control over the temporal delays and arm lengths in the interferometer.

Dual-Comb $g^{(2)}$ Calculation

Calculating the $g^{(2)}$, there is a key difference compared to our previous approaches in Chapter 3. Previously, we fixed the optical delay at one point, measured while scrambling the phase, and then calculated the $g^{(2)}$ from that position. In contrast, our current setup involves continuous scanning of the optical delay, where we only measure one pulse per scan position. This means that instead of scrambling the phase at a single optical delay point, we now vary the phase from one scan to the next. Consequently, after performing a number of scans, we can compute the $g^{(2)}$, as the phase becomes randomized between the same optical delay of successive scans.

Interestingly, we can exploit the noise in the Carrier-Envelope Phase (φ_{CEO}) of the interference fringes, as illustrated in Fig. 5.2, for our $g^{(2)}$ calculations. When we stack all the scans, we observe that the phases for a single temporal delay point are randomized, allowing us to directly apply Eq. (2.18) to derive the intensity correlation curve.

Additionally, we face another challenge: while noise in φ_{ceo} is no concern, there are many other noise sources that will become problematic in our analysis. One such source is the uncertainty in the repetition rate difference Δf_{rep} between the two dual comb lasers, which dictates the scan rate and the effective time resolution of the dual-comb system. This uncertainty can alter the system's response function and cause shifts in the measured signal timing. In the first order, the width can be neglected, as it only broadens relatively by the standard deviation of the the Δf_{rep} noise. However, the noise in timing is considerably higher, necessitating further

corrections. When we have high enough signals, we can use the interferograms to correct for timing. However, the $g^{(2)}$ method excels in situations where the signal is buried within significant noise. Therefore, a more sophisticated approach is required for timing correction in cases with insufficient SNR.

A promising strategy is to employ subsampling of the scans within a sliding window, as well as applying a condition on the maximum drift within the window. The process is as follows: we define a window and stride size across the frames (scans), then calculate the $g^{(2)}$ within this small window. Since this involves only a limited number of frames, the SNR and visibility will initially be poor. Next, we apply a smoothing filter across the optical delay (scan axis) and fit a Gaussian, starting with a reasonable fitting parameter estimations based on known values (laser bandwidth, estimated timing, maximum visibility, etc.). We then evaluate the goodness of fit and the width of the Gaussian. If the fit or width of the Gaussian exceeds an arbitrarily defined limit, we discard this trace, as the noise drift within that frame is too high (e.g. due to significant gradients in the repetition rate noise).

We slide this window across the entire array and calculate the $g^{(2)}$ from each subwindow. There are two approaches to calculate the final $g^{(2)}$ curve. Either we determine the shift for each scan using the value corresponding to the centre of the window, then readjust the frames with this correction. Or we compute the mean of all subsampled $g^{(2)}$ values. Mathematically, these methods should yield equivalent results:

$$g^{(2)}(t) = \frac{\langle I_1(t) I_2(t) \rangle}{\langle I_1(t) \rangle \langle I_2(t) \rangle} = \frac{1}{N} \frac{\sum_{i=1}^{N} I_1^i I_2^i}{\bar{I}_1 \bar{I}_2}. \tag{5.5}$$

For simplicity, we employ the second approach.

Synchronized Dynamic-Scan Routine

The dynamic scan ability in the CANDi has huge potential to reduce acquisition time of the measurement. So far the DCANDi been operated by locking the mean Δf_{rep} difference to zero with a PID controller, as has been shown in [134]. This ensures that the absolute values of Δf_{rep} before and after switching remain consistent. However, as previously reported, even a slight asymmetry can cause the region of interest to drift, and its stability is primarily dependent on the performance of the PID controller. Here we present an alternative method using an optical reference to fully stabilize the region of interest scan, as illustrated in Fig. 5.6. This method employs an AWG to generate a square wave that modulates the pump power of one laser. However, in this setup, the square waves are synchronized with a trigger signal derived from sampling both

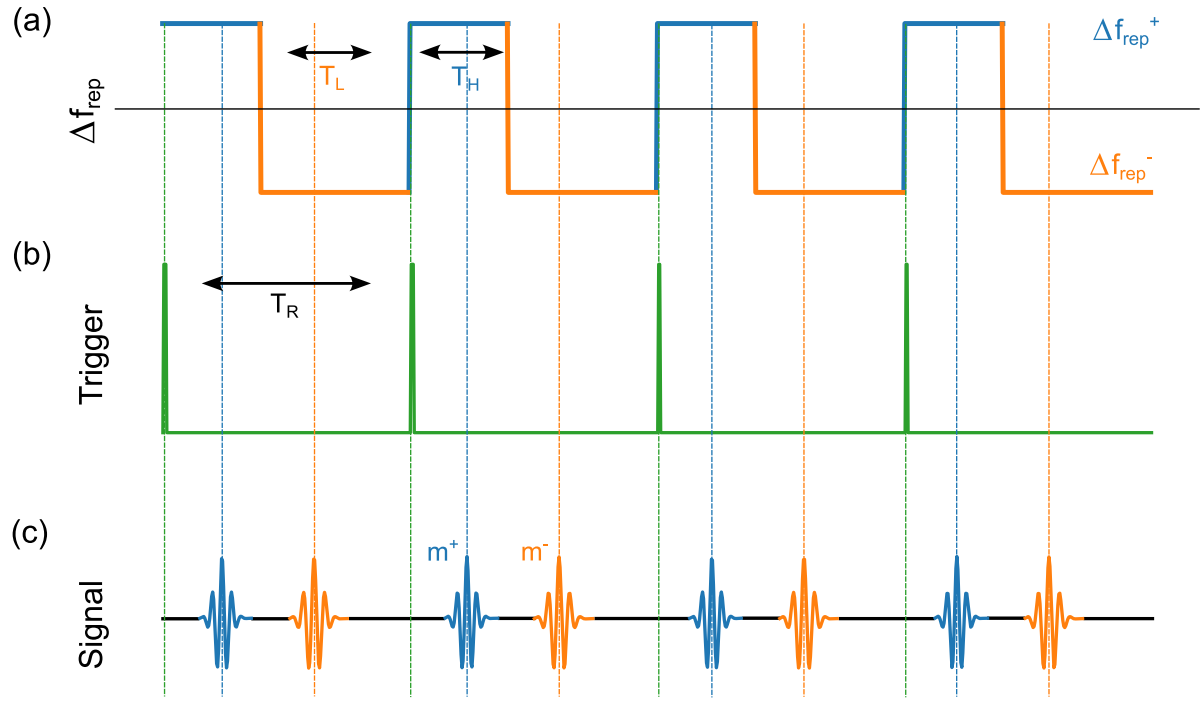

Figure 5.6: **DC Dynamic Scan Routine:** Process for dynamically scanning the laser in a drift-free manner. (a) The changes in Δf_{rep}, switching between low and high values, synchronized with the trigger signal in (b), where it holds for a fixed dwell period. (c) The resulting interferograms (IGMs), where the positive scan direction is shown in blue and the negative scan direction in orange. Each scan direction and state corresponds to a specific magnification factor.

combs, as shown in Fig. 5.5. Initially, the square wave provides a positive Δf_{rep}, scanning in the positive direction across the region of interest. The time spent scanning in the positive direction is fixed by the AWG. Subsequently, the square wave switches to a low voltage state, inverting Δf_{rep}, and scans in the negative direction. This negative scan duration is no longer predefined, as the exact magnification factors (m^+ for positive Δf_{rep} and m^- for negative) could differ slightly. Therefore, the AWG is set to hold the low state until the scan reaches the optical trigger signal again, at which point the AWG switches the square wave back to the positive state, reversing the scan direction once more.

Thus, the AWG functions as a triggered positive pulse of fixed width (T_H) with a base at the negative value. The main advantage of this approach is that the scans in both positive and negative directions cover the same real optical delays (τ_L, τ_H) rather than the same measured times (T_L, T_H). The conversion from measured time to real optical time is defined as:

$$|T_i| = |\tau_i \cdot m_i| \tag{5.6}$$

The start of the scan region is defined by the optical trigger signal, while the end is determined by $T_H = T_{\mathrm{AWG}}$ and m^+. For this technique, the following relations hold:

$$\begin{aligned} T_H(i) &= T_{\mathrm{AWG}} = \tau_i \cdot m_i^+, \\ T_L(i) &= \tau_i \cdot m_i^- = T_{\mathrm{AWG}} \frac{m_i^+}{m_i^-}, \\ T_R(i) &= T_H + T_L = \tau_i \cdot (m_i^- + m_i^+), \end{aligned} \tag{5.7}$$

which relate the measured scan times to the optical scan times.

The key concept is that, even with asymmetric switching, the laser remains locked to its intended region-of-interest (ROI). The laser scans in the positive direction for a fixed duration and in the negative direction for a time corresponding to the optical (demagnified) scan time. Although the actual times may differ for each direction, they match in terms of the physical optical scan range.

One issue arises from the potential difference in magnification factors (m^+ and m^-) for the positive and negative scan directions, leading to asymmetrical scanning. Therefore, it is necessary to correct for this discrepancy to ensure both scan directions are on the same time basis when calculating the $g^{(2)}$ using both directions. An additional reference signal might be needed to fully determine the magnification factors for each scan.

5.3 Application Potential & Findings

Beating due to Spectral Shape

An interesting, though not critical, finding is the emergence of oscillatory artefacts in the $g^{(2)}$ curve, particularly visible as oscillations at the edges of the peak in Fig. 5.7. These artefacts could arise from spectral beatings or non-linear phase effects.

Upon examining the spectra of the combs, we observed characteristic "cat ears"—peaks at both ends of the spectrum. By filtering out one of these peaks, the artefacts were significantly reduced. When both peaks were filtered, the artefacts were nearly eliminated, suggesting that the oscillations originate from the spectral beating between these "cat ears" rather than from non-linear phase contributions.

The oscillations are most prominent at the edges of the $g^{(2)}$ curve, and the beating frequency changes due to the specific spectral interactions of the combs. In Fig. 5.7, we observe two distinct

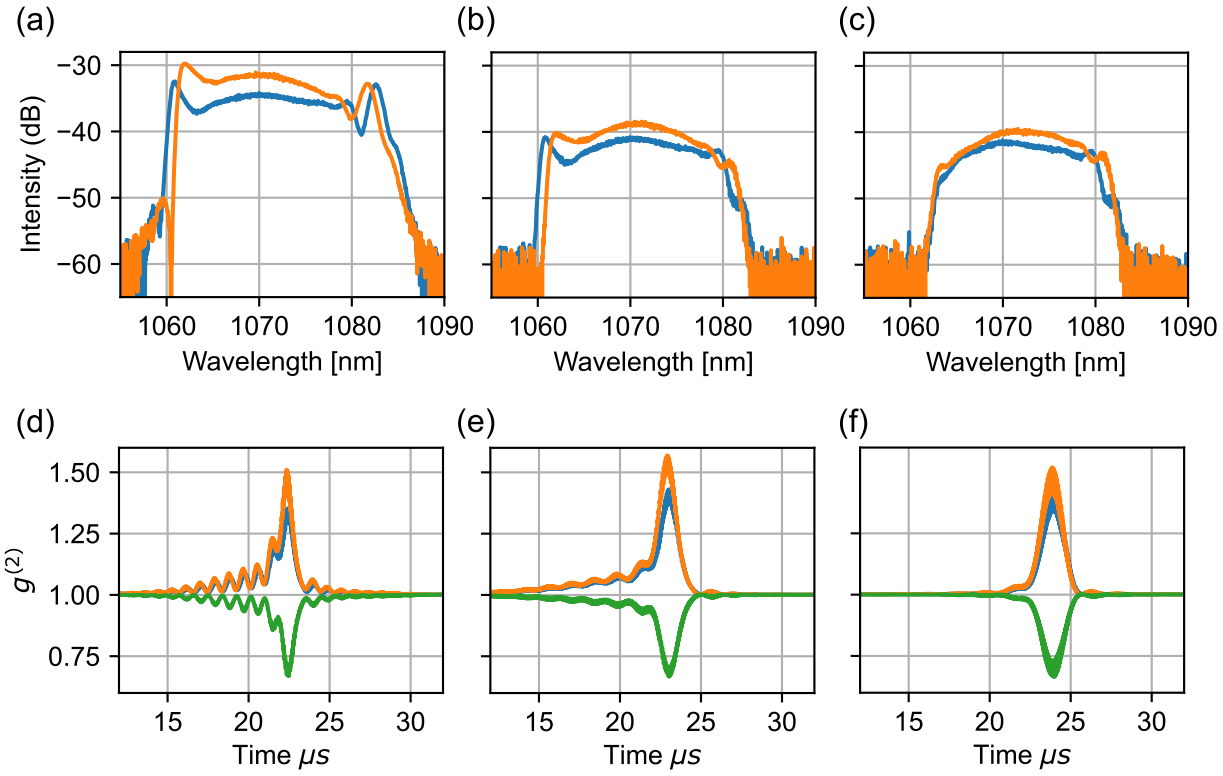

Figure 5.7: **DC Spectral Beating Artifact:** Overview of an artifact in the $g^{(2)}$ correlation function caused by frequency beating. (a)-(c) The spectra of comb 1 (blue) and comb 2 (orange), shown without filtering, with a low-pass (LP) filter, and with a band-pass (BP) filter, respectively. (d)-(f) The corresponding correlation curves, with decreasing beating artefacts as the "bunny ears" are filtered out. The auto-correlations for comb 1 and comb 2 are plotted in blue and orange, respectively, while the cross-correlation is shown in green.

peaks for each comb. For comb 1 (orange), these peaks occur at 1061.75 nm and 1081.50 nm, while for comb 2 (blue), the peaks are at 1060.75 nm and 1082.50 nm. The spectral beating between these peaks—particularly the interaction between the left "ear" of comb 1 and the right "ear" of comb 2, and vice versa—yields a theoretical beating wavelength of approximately 54.5 µm. The observed oscillations in the unfiltered case have a period of around 0.87 µs in magnified time. When converting this into physical time by dividing by the magnification factor $m = 48 \times 10^5$ and further converting to physical distance, the resulting wavelength is approximately 54.2 µm, which aligns well with the predicted beating of the "cat ears".

When filtering only one of the peaks, the artefacts are still present but exhibit reduced amplitude and frequency. This reduction occurs because the remaining "cat ear" is now beating with the central part of the spectrum, which is closer in wavelength, producing a shorter synthetic wavelength.

The artefacts are particularly prominent near the edges of the $g^{(2)}$ curve. It can be explained

by relating with the case of a pulsed laser with finite bandwidth (continuous spectrum) and two continuous-wave (CW) lasers at different wavelengths (the "cat ears") injected into a Mach-Zehnder interferometer, using the equations derived in Section 2.3. The CW lasers have a much longer coherence length than the pulsed laser, causing the beatings between the CW components to be most visible beyond the coherence length of the pulse. Furthermore, this effect broadens the $g^{(2)}$ curve, as observed.

Therefore, to clean up the $g^{(2)}$ signal and eliminate these artefacts, it is necessary to filter out the "cat ears" from the spectrum.

Linear & Dynamic Scan Example

In Fig. 5.8, we compare a single scan acquired over 125 ms for both the linear and dynamic scanning methods. It is evident that the signal in the linear scan is much sparser, whereas the dynamic scanning method produces significantly more signal. The linear scan was acquired one IGM at a time by measuring for 125 µs for each trigger. For the linear scan with $\Delta f_{\text{rep}} = 10$ Hz, the acquisition time is 50 s when collecting 500 frames to obtain the $g^{(2)}$-peak shown in Fig. 5.8(c). In contrast, for the dynamic scan, with a pulse width of $T_H = 100$ µs, the scan rate is approximately 10 kHz. Acquiring 500 frames to generate the $g^{(2)}$-peak in Fig. 5.8 takes only 50 ms.

Comparing the two curves shows that they are of equal quality and visibility, although the dynamic scan exhibits a slightly broader $g^{(2)}$ peak, possibly due to a minor shift in Δf_{rep}. Nevertheless, the acquisition for the dynamic scan is three orders of magnitude faster.

Δf_{rep} Noise Correction

Despite the numerous advantages of using a dual-comb scanned laser, there are significant drawbacks. One of the main challenges, particularly in the high-resolution regime, is the requirement for a small repetition rate difference, Δf_{rep}, between the combs. The current version of the DCANDi is not sufficiently isolated; hence, the primary source of noise affecting the repetition rate arises from environmental influences such as temperature fluctuations or humidity. Furthermore, the RIN of the pump lasers directly translates into noise of the Δf_{rep}. While the pump lasers are generally more stable due to specific electrical filtering in their power supplies (to remove mains frequency noise), connecting the frequency generator required for dynamic scanning introduces noise into the pump system. The degradation in our results caused by noise can be visualized in Fig. 5.9(b).

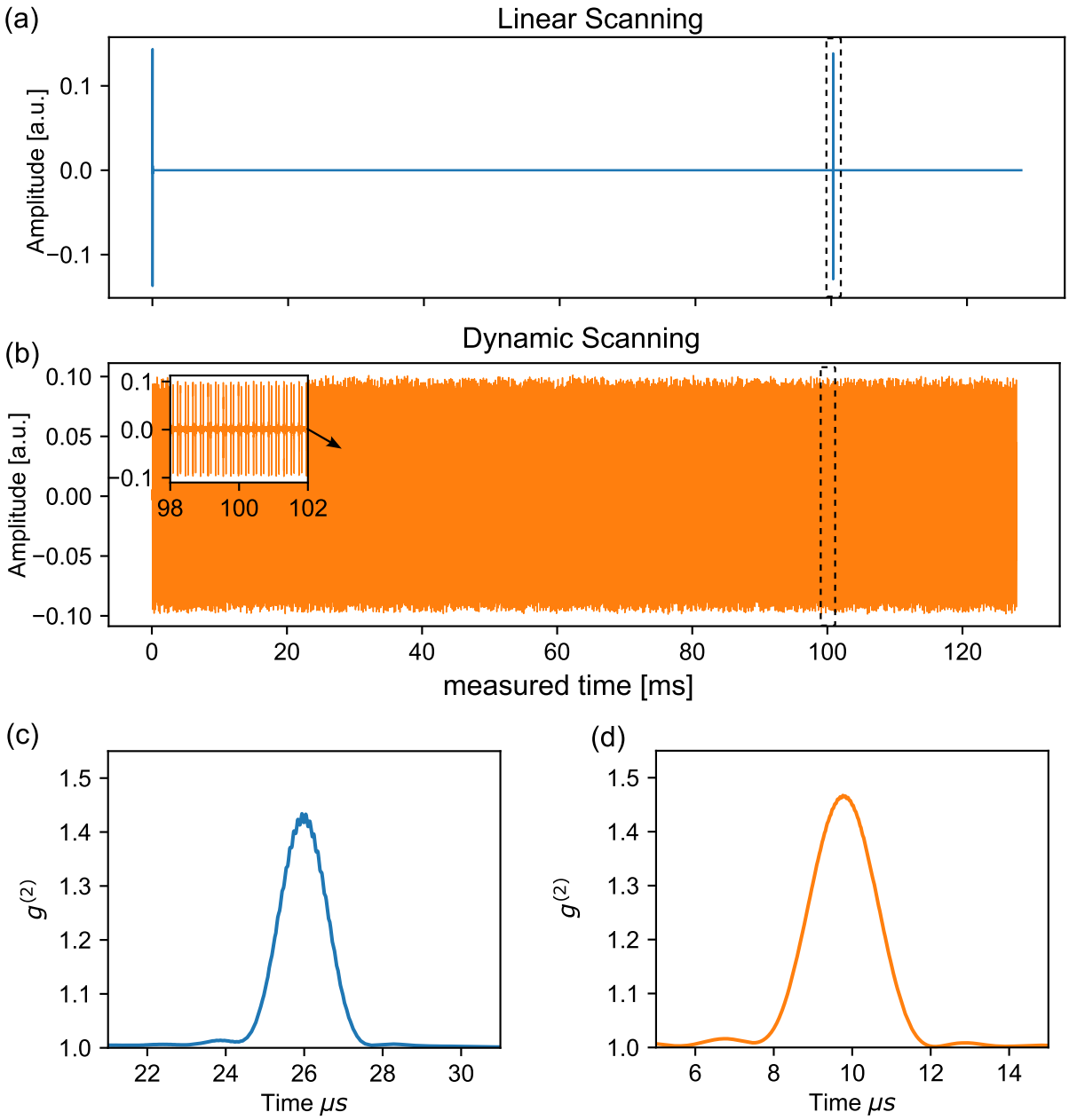

Figure 5.8: **Linear and Dynamic Scan Comparison:** Measured intensity (IGMs) as a function of time for the linear scan method (a) and the dynamic scan method (b). It is evident that the dynamic scan provides significantly more information within the same acquisition time. (c) The $g^{(2)}$ curve generated from 500 frames using the linear scan method, and (d) the dynamic scan method. The linear scan required an acquisition time of 50 s, while the dynamic scan achieved the same with only 50 ms, representing a 2-3 order of magnitude reduction in acquisition time.

To mitigate these issues, we developed several noise-correction methods. One approach involves positioning the trigger signal as close as possible to the measured signal. Since the measured time of arrival of the pulse is determined by the optical delay between the trigger and the signal, multiplied by the magnification factor, any noise in Δf_{rep} propagates through the magnifi-

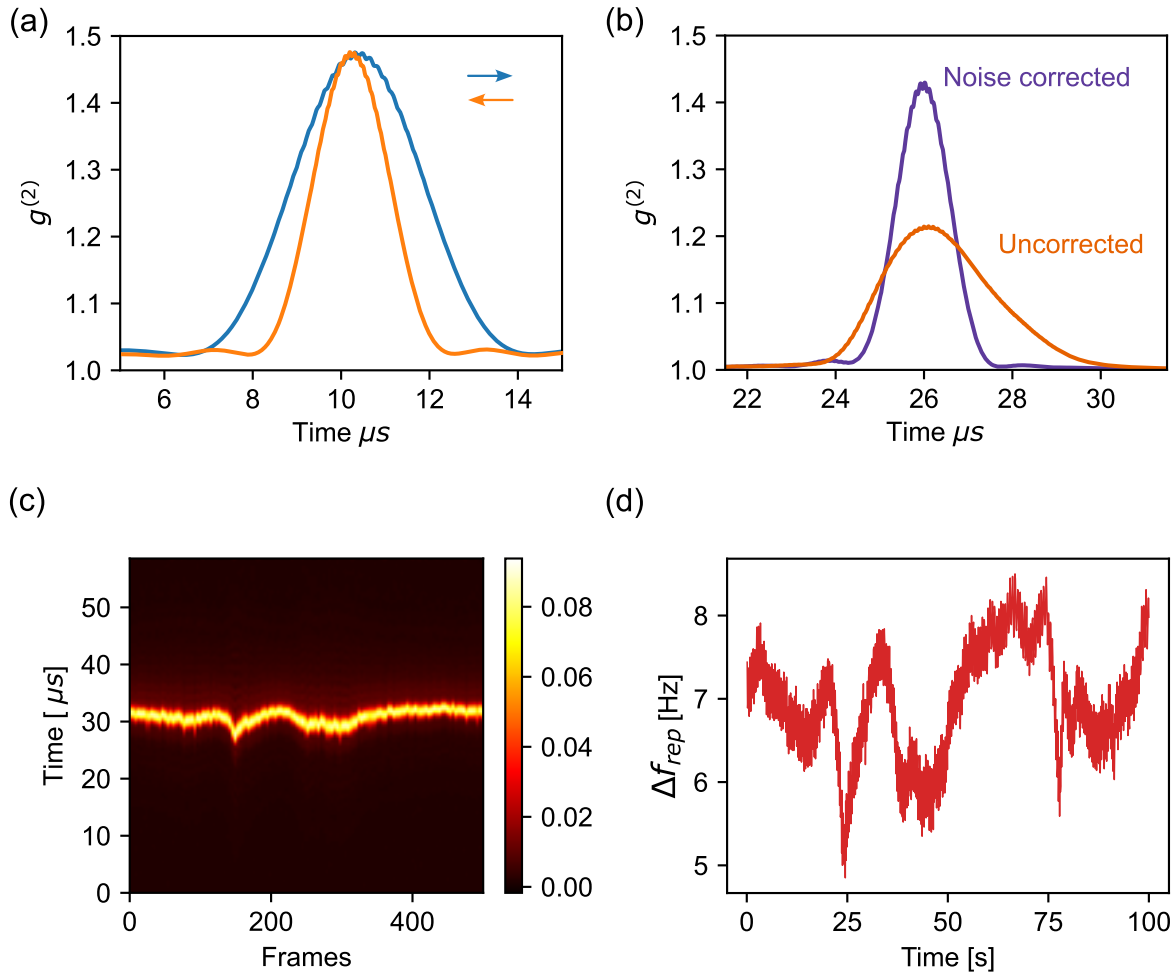

Figure 5.9: **DC Laser Noise Analysis:** Analysis of the dominant error and noise sources in the system. (a) The $g^{(2)}$ width resulting from asymmetric dynamic scanning, which requires correction. (b) Degradation in the visibility and width of the $g^{(2)}$ curve due to large Δf_{rep} noise, with the noise-corrected version applying timing correction. (c) Timing jitter of the IGMs as a function of frame number. (d) Measured Δf_{rep} rate difference using a frequency counter, showing behaviour similar to the IGM's jitter. This confirms that Δf_{rep} rate jitter is the main contributing factor to noise.

cation factor, leading to signal fluctuations. Additionally, we introduced a static reference signal after the trigger to monitor Δf_{rep}. In Fig. 5.9(c), we show the trace of the timing shifts used to correct the jitter generated from the measured IGMs. The correlation between the measured Δf_{rep} (from the frequency counter of each comb) and the timing shifts is clearly illustrated in Fig. 5.9(c).

For smaller jitter, noise correction can also be achieved without reference signals. As detailed in Section 5.2.2, we developed a method to correct noise by subsampling the frames and applying an optimization algorithm to the $g^{(2)}$ curve. Even with good SNR, this method limits the achievable resolution to tens of microns—adequate for many applications, but insufficient

for microscopy. Consequently, further efforts are necessary to improve the stability of the laser system.

Moreover, due to the nature of our dynamic scanning routine, it is necessary to correct for asymmetry in the tuning between both directions. This asymmetry can lead to significantly different magnification factors for each direction, as highlighted in Fig. 5.9(a).

Signal-to-Noise-Ratio

To reiterate, the main benefit of using $g^{(2)}$ correlations is their robustness against phase noise, enabling the generation of a $g^{(2)}$ peak even in very low SNR scenarios. The process can also be interpreted as a form of incoherent averaging. Here, we demonstrate the potential of our technique applied to various SNR conditions using the dual-comb laser. We define the SNR as:

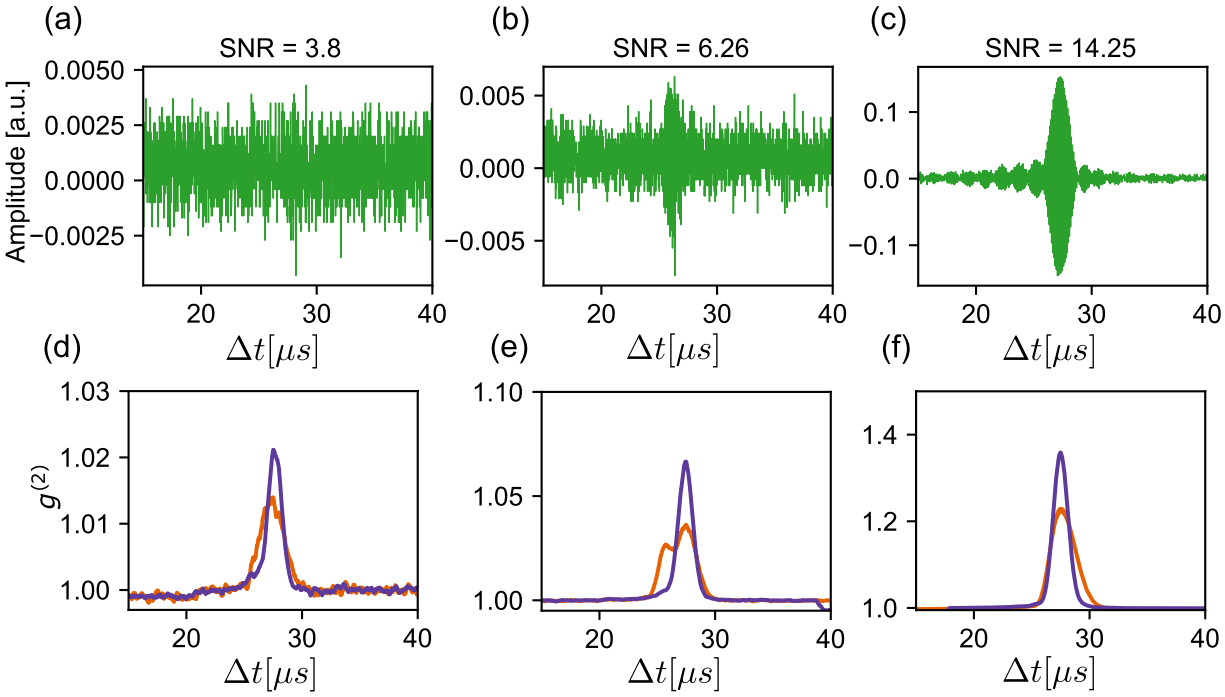

Figure 5.10: **DC SNR Analysis:** Demonstration of recovering the $g^{(2)}$ curve in extremely low SNR scenarios. (a)-(c) The IGMs at different SNR levels. (d)-(f) The corresponding $g^{(2)}$ curves, where the red lines represent the uncorrected case with timing jitter, and the purple lines show the corrected case using the developed subsampling algorithm. Note that the width remains consistent, while only the visibility decreases with lower SNR.

$$\mathrm{SNR} = \frac{|I_{\mathrm{peak}}|}{\sigma_{\mathrm{Noise}}} \tag{5.8}$$

Furthermore, we compare the $g^{(2)}$ peak when uncorrected and after correction with our $g^{(2)}$ optimization technique, as developed and described in Section 5.2.2.

In high SNR scenarios, the interferogram is clearly visible, and we achieve high visibility, as shown in Fig. 5.10(c). In Fig. 5.10(f), we display the corresponding $g^{(2)}$ peak for both corrected and uncorrected cases. The presence of noise broadens the peak and reduces visibility. In the case with an SNR of around 6.26, we observe a reduced visibility, but it remains distinguishable, with a double peak arising when uncorrected. Finally, in the scenario where the signal is comparable to the noise and the IGM is not visible, we can still extract the $g^{(2)}$ peak, as shown in Fig. 5.10(a)&(d), with a substantially smoother curve when applying the correction.

5.4 Conclusion

In this chapter, we have investigated the intricacies of dual-comb laser systems and their influence on measuring the $g^{(2)}$ correlation function, focusing on both the challenges and advancements in our methodology. The key result of our work is that utilizing a dual-comb laser system eliminates the need for a mechanical delay line, eliminating its associated drawbacks such as vibrations, scan speed limitations, alignment issues, and range constraints.

Compared to the state of the art, particularly established methods like time-correlated single-photon counting (TCSPC), ideal dual-comb laser systems provide much higher resolution—on the order of 1 mm for TCSPC systems [42] to sub-micron resolution for dual-comb lasers [139]. When compared to conventional delay-line setups with similar resolutions, our work represents a significant leap forward by eliminating the need for a delay line and its associated limitations.

Furthermore, the analysis highlighted the critical role of the spectrum and its direct connection to $g^{(2)}$. Specifically, the characteristic "cat ears" in the comb spectra introduced artefacts in the correlation curve. By employing targeted filtering techniques, we were able to significantly reduce these artefacts, improving the accuracy and reliability of our measurements.

The comparative analysis of linear versus dynamic scanning methods underscored the clear advantages of dynamic scanning, which dramatically reduces acquisition time—capturing data of the same quality in milliseconds, as opposed to seconds with the linear method. This breakthrough overcomes the traditional resolution-acquisition time limitations, enabling more efficient data collection and expanding the potential for high-resolution applications across various fields.

Despite all these benefits, a significant issue arises with dual-comb lasers, particularly the one we used: fluctuations in the repetition rate difference between the two laser combs. This repetition rate difference effectively leads to a shift in the signal's timing, as the difference de-

termines when the signal will be measured, even though optically it corresponds to the same time-of-flight (ToF) difference between the paths of the two combs (signal and reference). As a result, this fluctuation introduces an error in the arrival time measurement, as can be seen in Fig. 5.9(c)&(d). For example, a 1% error in the repetition rate difference (Δf_{rep}) would lead to a 1% error in the arrival time. For a distance of 2 mm, this results in an error of 20 µm, which scales with distance. For a target 100 cm away, the error becomes 10 mm, potentially worse than TCSPC systems. Hence we need a method that corrects for this error.

We developed a noise-correction techniques to maintain the integrity of our measurements. By implementing a subsampling algorithm, we lowered the impact of repetition rate noise, enhancing the visibility of our $g^{(2)}$ peaks even in low signal-to-noise ratio (SNR) conditions, without requiring any external reference or additional corrections.

While our findings underscore the robustness of the $g^{(2)}$ correlation technique against phase noise and other perturbations, the time resolution even in the noise corrected case (10s of microns) remains insufficient for non-line-of-sight (NLOS) imaging and microscopy applications, necessitating further work to improve laser stability. Although non-dynamic tunable lasers exhibit better noise performance, they come with their own set of disadvantages such as smaller range, bigger time steps and high repetition rate meaning less pulse energy for the same power of laser. Therefore, additional investigations are essential to enhance laser stability and refine algorithms, aiming for even higher resolution and reliability. This work paves the way for future research and applications of dual-comb laser systems across various fields, including microscopy and precision measurements, ultimately contributing to the advancement of optical technologies.

This work has demonstrated the potential of dual-comb lasers for $g^{(2)}$ measurements, providing proof of principle for their use in high-resolution applications. Although the current system is not yet sufficient in terms of stability and noise performance for the intended applications and remains cumbersome, with improvements and miniaturization, dual-comb lasers will provide a compelling alternative to mechanical scanning setups, while offering a much higher-resolution approach than conventional methods like TCSPC.

Chapter 6.

Conclusion & Future Outlook

6.1 Conclusion

This thesis highlights the importance and advantages of intensity correlation measurements across various imaging modalities, particularly in high-resolution microscopy and imaging through scattering media. We have established that time-of-flight (ToF) microscopy significantly benefits from employing $g^{(2)}$ techniques, which demonstrate improved phase stability compared to traditional methods. Although the resolution achievable with a single wavelength band is somewhat limited relative to other techniques, the introduction of a dual-wavelength approach substantially improves resolution, as validated by our Fisher information analysis. The dual-wavelength results demonstrate the ability to measure nanometric resolution, with achieved resolutions down to 10 nm of optical path length difference. This level of resolution is comparable to that of state-of-the-art techniques such as SLIM, QPI, and DHM, discussed in Section 3.1.

While our technique achieves resolutions comparable to established methods, significant stability challenges from environmental factors—such as temperature variations, vibrations, and mechanical instabilities—persist. These factors can introduce inaccuracies in temporal delay measurements, potentially resulting in large errors if not carefully managed. Although the $g^{(2)}$ correlation approach enhances stability by being robust to phase fluctuations, it does not completely eliminate the effects of environmental noise. This is particularly crucial for the dual-wavelength high-resolution method, where those inaccuracies in optical delay measurements can easily exceed the found 10 nm resolution limit. To enhance measurement accuracy and maintain competitive performance across various applications, continuous refinement of noise-correction strategies is essential. Specifically, the stability of the interferometer will impact the resolution achieved with the dual-wavelength approach. Additionally, the nature of the noise distribution plays a critical role in measurement fidelity; while Gaussian noise is generally manageable, skewed distributions or a drift can lead to significant challenges and further inaccuracies.

Furthermore, we explored the advancements made by replacing the established holographic method of SWH) with our phase-stable $g^{(2)}$ method. This transition yielded significant improvements in SNR and overall stability, as we no longer rely on holographic methods, which were previously the standard approach. Furthermore we showed how this approach shines in the presence of dynamic scattering since we can exploit it in our method, that needs phase randomization. However, the need for phase stepping introduces a trade-off in speed. Despite the resilience of

our technique to dynamic scattering, it does face limitations when the object under observation moves too rapidly, although potential solutions exist to address this issue.

Furthermore, the chapter on dual-comb lasers demonstrated the proof of principle for utilizing $g^{(2)}$. This advancement allows us to circumvent the challenges associated with mechanical scanning methods, such as beam walk and vibrations. Our experiments with the dual-comb laser system have shown promise for improving ranging capabilities over large scanning ranges, which would be cumbersome with a delay line, while maintaining high resolution. However, at present, the performance of our dual-comb system does not surpass that of mechanical scanning methods, primarily due to increased noise levels in the timing information, despite its faster acquisition times. Looking ahead, further research is needed to refine noise reduction techniques and optimize system configurations to enhance performance.

6.2 Future Outlook

The advancements made in this work through $g^{(2)}$ correlations are significant and set a promising foundation for future developments in optical technologies. These innovations not only enhance existing methodologies but also open up new avenues for research and practical applications.

Single-Shot & High-Speed Imaging

As highlighted throughout this thesis, rapid measurements for microscopy or NLOS is of paramount importance. In the context of microscopy, we have presented a method that combines both dual and single wavelength techniques to enable single-shot measurements by obtaining two estimations at different scales, thereby providing an absolute precise time-of-flight (ToF). Additionally, the integration of high-speed, large pixel count cameras could further enhance the speed of these measurements. However, this approach also introduces complexities and higher costs, indicating a clear trade-off between speed, complexity, and affordability.

In the NLOS imaging project, our current methodology faces limitations in applications involving dynamic objects due to the necessity of phase steps and the associated long measurement times, as discussed in previous chapters. Nevertheless, there is significant potential for improvement to expedite the measurements. We propose the implementation of a two phase-step method in a two-camera setup, which could reduce the measurement time by a factor of three. Furthermore, additional strategies could be explored by utilizing probabilistic methods to extract more information from the full measurement data, such as the development of a machine learning-based estimator.

Given the unique speckle patterns produced and the anticipated spatial correlations from the spreading of the synthetic wavelength, we could develop a machine learning-based estimator that analyses the correlations within small windows and effectively subsamples the hologram for reconstruction. In scenarios devoid of dynamic scattering, where phase fluctuations remain controlled and consistent across pixels, it may be feasible to investigate the actual correlation dynamics—not just the correlation magnitude. This understanding could lead to a more nuanced grasp of the synthetic wavelength and enhance holographic reconstructions.

Furthermore, incorporating additional parameters to refine the hologram into the reconstruction optimization may refine the reconstruction accuracy, paving the way for groundbreaking advancements in single-shot NLOS imaging or even videography. The combination of innovative techniques and advanced computational approaches holds the promise of significant progress in these fields.

On-Chip Processing

For the simplest approach, where we only measure the decorrelation magnitude as $g^{(2)}$ at $\tau = 0$, we could significantly simplify the process by using on-chip processing. The only two values of interest are the top and bottom terms of Eq. (2.18). If we could generate these on-chip, it would be revolutionary. This could be achieved with an FPGA, as done for Diffuse Correlation Spectroscopy (DCS) [142, 143], or through simple electronics utilizing a frequency mixer and splitter, as demonstrated in Chapter 5 when not performing wide-field imaging. This would enable faster processing since we would no longer need to transfer a vast amount of data for computation; instead, we could transfer a 2-3 channel image and be done. Not only would this streamline the process, making it easier and faster, but it would also reduce the computational requirements for calculating $g^{(2)}$, among other metrics. Ultimately, on-chip processing could enhance the accessibility and scalability of our methods across various scientific and industrial applications.

Exploiting Dynamic Scattering in Medical Imaging

An unexpected finding during this research was the ability to exploit dynamic scattering processes for phase scrambling in $g^{(2)}$ measurements. While dynamic scattering typically introduces noise and instability in imaging systems, we discovered that it can effectively serve as a method for phase randomization. This opens new avenues for enhancing robustness and simplifying experimental setups by utilizing naturally occurring scattering events, reducing the need for additional equipment like rotating diffusers or piezo stages. One of the most exciting applications of

our technique is in medical imaging, particularly for imaging through dynamic scattering media such as tissue. By refining our synthetic wavelength methods and improving their adaptability to real-world biological conditions, we can significantly advance imaging techniques used in diagnostics and treatment planning. The potential applications in medical imaging are twofold. First, in low-scattering scenarios, we could achieve cellular imaging. By using synthetic wavelengths slightly larger than optical waves in the multiple micron regime, we can enhance clarity and signal-to-noise ratio (SNR), maintaining good resolution defined by Abbe's diffraction limit. Second, in highly diffuse regimes, we could image larger structures, such as bones, potentially replacing traditional X-rays. For instance, this technique could be utilized in ambulances to assess whether a bone fracture is impacting an artery. Future research should focus on evaluating our methods in clinical settings, assessing their performance under varying conditions, and exploring their integration with existing medical imaging technologies.

Dual-Comb Laser Systems for NLOS

Our work with dual-comb lasers has shown significant potential, particularly in eliminating mechanical scanning for optical delay. We are currently collaborating with the University of Colorado, where they are developing a more stable version of the laser. As discussed in Chapter 4 and Chapter 3, a key limitation of ToF methods lies in the time resolution of the system; hence, employing interferometric techniques can yield much more precise information. In NLOS scenarios, where distances of several meters are typically investigated, constructing a stable delay stage becomes cumbersome, as demonstrated in [144]. Dual-comb lasers, therefore, offer significant advantages in this context, enabling precise measurements over large ranges—an aspect that is cumbersome with mechanical scanning—while maintaining high resolution, surpassing traditional TCSPC methods.

To ensure robustness against phase noise, we plan to adopt a $g^{(2)}$ method for detection, as outlined in Chapter 3, rather than the non-linear crystal detection used in [144]. We will employ ToF-based methods described in Chapter 4 instead of synthetic wavelength holography, leveraging our access to time-domain information.

The dynamic scanning potential of CANDi further benefits NLOS imaging, where time information is often sparse, allowing us to efficiently scan small regions of interest behind obstructions without the need for a full scan. Alternatively, we could explore other laser systems with higher repetition rates that offer greater stability, though these systems also present challenges, particularly with the resolution–measurement time trade-off.

6.3 Closing Remarks

This thesis demonstrated the clear benefits of $g^{(2)}$-based methods, highlighting their simplicity and robustness against phase noise, even in challenging environments. I've demonstrated how these techniques can be effectively applied to high-resolution microscopy and NLOS imaging, and there are exciting possibilities for expanding their use across various fields. From medical imaging—where they could enable non-invasive imaging through biological tissue—to other areas of NLOS imaging for surveillance, the versatility of $g^{(2)}$ opens the door for impactful advancements and innovations across various fields.

Bibliography

[1] James Clerk Maxwell, "VIII. A dynamical theory of the electromagnetic field," *Philosophical Transactions of the Royal Society of London*, vol. 155, pp. 459–512, 12 1865.

[2] J. D. Jackson 1925-2016, *Classical electrodynamics*. Third edition. New York : Wiley, [1999] ©1999.

[3] M. O. Scully and M. S. Zubairy, *Quantum Optics*. Quantum Optics, Cambridge University Press, 1997.

[4] R. Loudon and T. von Foerster, "The Quantum Theory of Light," *American Journal of Physics*, vol. 42, no. 11, 1974.

[5] G. R. Fowles and D. W. Lynch, "Introduction to Modern Optics," *American Journal of Physics*, vol. 36, no. 8, 1968.

[6] R. H. Brown and R. Q. Twiss, "Correlation between photons in two coherent beams of light," *Nature*, vol. 177, no. 4497, 1956.

[7] R. Hanbury Brown and R. Q. Twiss, "A test of a new type of stellar interferometer on Sirius," *Nature*, vol. 178, no. 4541, 1956.

[8] A. J. F. Siegert and M. I. o. T. R. Laboratory, *On the fluctuations in signals returned by many independently moving scatterers*. [Cambridge, Mass.]: Radiation Laboratory, Massachusetts Institute of Technology, 1943.

[9] A. Rosławska, C. C. Leon, A. Grewal, P. Merino, K. Kuhnke, and K. Kern, "Atomic-Scale Dynamics Probed by Photon Correlations.," *ACS Nano*, vol. 14, pp. 6366–6375, 6 2020.

[10] R. J. Glauber, "The quantum theory of optical coherence," *Physical Review*, vol. 130, pp. 2529–2539, 6 1963.

[11] R. J. Glauber, "Coherent and Incoherent States of the Radiation Field," *Physical Review*, vol. 131, p. 2766, 9 1963.

[12] A. A. Michelson and E. W. Morley, "On the relative motion of the Earth and the luminiferous ether," *American Journal of Science*, vol. s3-34, no. 203, 1887.

[13] L. Zehnder, "Ein neuer Interferenzrefraktor," *Zeitschrift für Instrumentenkunde*, vol. 11, 1891.

[14] Y.-S. Kim, O. Slattery, P. S. Kuo, and X. Tang, "Two-photon interference with continuous-wave multi-mode coherent light," *Optics Express*, vol. 22, p. 3611, 2 2014.

[15] J. W. Goodman, "Speckle Phenomena in Optics: Theory and Applications, Second Edition," *Speckle Phenomena in Optics: Theory and Applications, Second Edition*, 1 2020.

[16] J. Sutin, I. Rech, B. Zimmerman, D. Tyulmankov, M. A. Franceschini, J. Selb, D. Tamborini, K. C. Wu, D. A. Boas, A. Tosi, and A. Gulinatti, "Time-domain diffuse correlation spectroscopy," *Optica, Vol. 3, Issue 9, pp. 1006-1013*, vol. 3, pp. 1006–1013, 9 2016.

[17] A. Nwaneshiudu, C. Kuschal, F. H. Sakamoto, R. Rox Anderson, K. Schwarzenberger, and R. C. Young, "Introduction to confocal microscopy," *Journal of Investigative Dermatology*, vol. 132, no. 12, pp. 1–5, 2012.

[18] M. Wenninger, C. Marschik, K. Felbermayer, B. Heise, T. Kranzl, and G. Steinbichler, "A novel measurement approach based on optical coherence tomography for inline quality assessment of thermoplastic glass-fiber reinforced unidirectional tapes," *Journal of Thermoplastic Composite Materials*, vol. 36, pp. 3943–3965, 10 2023.

[19] Z. Wang, L. Millet, M. Mir, H. Ding, S. Unarunotai, J. Rogers, M. U. Gillette, and G. Popescu, "Spatial light interference microscopy (SLIM)," tech. rep., 2011.

[20] T. A. Zangle, J. Chun, J. Zhang, J. Reed, and M. A. Teitell, "Quantification of biomass and cell motion in human pluripotent stem cell colonies," *Biophysical Journal*, vol. 105, pp. 593–601, 8 2013.

[21] J. Pawley, *Handbook of Biological Confocal Microscopy*. Springer US, 2013.

[22] M. Minsky, "Memoir on inventing the confocal scanning microscope," *Scanning*, vol. 10, no. 4, 1988.

[23] C. Fouquet, J. F. Gilles, N. Heck, M. D. Santos, R. Schwartzmann, V. Cannaya, M. P. Morel, R. S. Davidson, A. Trembleau, and S. Bolte, "Improving axial resolution in confocal microscopy with new high refractive index mounting media," *PloS one*, vol. 10, 3 2015.

[24] L. Schermelleh, R. Heintzmann, and H. Leonhardt, "A guide to super-resolution fluorescence microscopy," *Journal of Cell Biology*, vol. 190, pp. 165–175, 7 2010.

[25] M. Schrader and S. W. Hell, "4Pi-confocal images with axial superresolution," *Journal of Microscopy*, vol. 183, pp. 110–115, 8 1996.

[26] B. E. Bouma, J. F. de Boer, D. Huang, I. K. Jang, T. Yonetsu, C. L. Leggett, R. Leitgeb, D. D. Sampson, M. Suter, B. J. Vakoc, M. Villiger, and M. Wojtkowski, "Optical coherence tomography," *Nature Reviews Methods Primers*, vol. 2, 12 2022.

[27] E. J. Fernández and W. Drexler, "Influence of ocular chromatic aberration and pupil size on transverse resolution in ophthalmic adaptive optics optical coherence tomography," *Optics Express*, vol. 13, no. 20, 2005.

[28] D. P. Popescu, L. P. Choo-Smith, C. Flueraru, Y. Mao, S. Chang, J. Disano, S. Sherif, and M. G. Sowa, "Optical coherence tomography: Fundamental principles, instrumental designs and biomedical applications," 9 2011.

[29] Z. Yaqoob, J. Wu, and C. Yang, "Spectral domain optical coherence tomography: a better OCT imaging strategy.," 2005.

[30] R. F. Spaide, H. Koizumi, and M. C. Pozonni, "Enhanced Depth Imaging Spectral-Domain Optical Coherence Tomography," *American Journal of Ophthalmology*, vol. 146, no. 4, 2008.

[31] M. Choma, M. Sarunic, C. Yang, and J. Izatt, "Sensitivity advantage of swept source and Fourier domain optical coherence tomography," *Optics Express*, vol. 11, no. 18, 2003.

[32] J. F. de Boer, B. Cense, B. H. Park, M. C. Pierce, G. J. Tearney, and B. E. Bouma, "Improved signal-to-noise ratio in spectral-domain compared with time-domain optical coherence tomography," *Optics Letters*, vol. 28, no. 21, 2003.

[33] M. K. Kim, "Principles and techniques of digital holographic microscopy," 2010.

[34] Y. K. Park, C. Depeursinge, and G. Popescu, "Quantitative phase imaging in biomedicine," 10 2018.

[35] C. J. Cheng, Y. L. Lee, and Y. C. Lin, "High-resolution digital holographic microscopy," in *2012 IEEE Photonics Conference, IPC 2012*, 2012.

[36] F. Zernike, "Phase contrast," *Z Tech Physik*, vol. 16, p. 454, 1935.

[37] Y. K. Park, C. Depeursinge, and G. Popescu, "Quantitative phase imaging in biomedicine," 10 2018.

[38] C. J. Mann, L. Yu, C.-M. Lo, and M. K. Kim, "High-resolution quantitative phase-contrast microscopy by digital holography," *Optics Express*, vol. 13, no. 22, 2005.

[39] A. McCarthy, N. J. Krichel, N. R. Gemmell, X. Ren, M. G. Tanner, S. N. Dorenbos, V. Zwiller, R. H. Hadfield, and G. S. Buller, "Kilometer-range, high resolution depth imaging via 1560 nm wavelength single-photon detection," *Optics Express*, vol. 21, p. 8904, 4 2013.

[40] A. Mccarthy, R. J. Collins, N. J. Krichel, V. Fernández, A. M. Wallace, and G. S. Buller, "Long-range time-of-flight scanning sensor based on high-speed time-correlated single-photon counting," tech. rep., 2009.

[41] R. H. Hadfield, J. Leach, F. Fleming, D. J. Paul, C. H. Tan, J. S. Ng, R. K. Henderson, and G. S. Buller, "Single-photon detection for long-range imaging and sensing," *Optica*, vol. 10, p. 1124, 9 2023.

[42] H. Bender, E. G. T. Bosch, O. Richard, S. Pellegrini, G. S. Buller, J. M. Smith, A. M. Wallace, and S. Cova, "Laser-based distance measurement using picosecond resolution time-correlated single-photon counting Terahertz imaging system with resonant tunneling diodes Tomoyuki Miyamoto, Atsushi Yamaguchi and Toshikazu Mukai-3D characterization of nanowire devices with STEM based modes Laser-based distance measurement using picosecond resolution time-correlated single-photon counting," tech. rep., 2000.

[43] C. K. Hong, Z. Y. Ou, and L. Mandel, "PHYSICAL REVIEW LETTERS Measurement of Subpicosecond Time Intervals between Two Photons by Interference," tech. rep., 1987.

[44] A. Lyons, G. C. Knee, E. Bolduc, T. Roger, J. Leach, E. M. Gauger, and D. Faccio, "Attosecond-resolution Hong-Ou-Mandel interferometry," tech. rep., 2018.

[45] B. Ndagano, H. Defienne, D. Branford, Y. D. Shah, A. Lyons, N. Westerberg, E. M. Gauger, and D. Faccio, "Quantum microscopy based on Hong–Ou–Mandel interference," *Nature Photonics*, vol. 16, pp. 384–389, 5 2022.

[46] S. Johnson, C. Lualdi, A. Conrad, N. Arnold, M. Vayninger, and P. Kwiat, "Toward vibration measurement via frequency-entangled two-photon interferometry," in *Quantum Sensing, Imaging, and Precision Metrology* (S. M. Shahriar and J. Scheuer, eds.), p. 176, SPIE, 3 2023.

[47] Y. Zhang, Z. He, X. Tong, D. C. Garrett, R. Cao, and L. V. Wang, "Quantum imaging of biological organisms through spatial and polarization entanglement," tech. rep.

[48] R. Murray and A. Lyons, "Two-Photon Interference LiDAR Imaging," tech. rep., 2022.

[49] G. Thekkadath, D. England, and B. Sussman, "Intensity correlation holography for remote phase sensing and 3D imaging," *Optics Express*, vol. 31, p. 43574, 12 2023.

[50] J. Szuniewicz, S. Kurdziałek, S. Kundu, W. Zwolinski, R. Chrapkiewicz, M. Lahiri, and R. Lapkiewicz, "Noise-resistant phase imaging with intensity correlation," tech. rep., 2023.

[51] P. Yepiz-Graciano, A. M. A. Martínez, D. Lopez-Mago, H. Cruz-Ramirez, and A. B. U'Ren, "Spectrally resolved Hong–Ou–Mandel interferometry for quantum-optical coherence tomography," *Photonics Research*, vol. 8, p. 1023, 6 2020.

[52] D. Triggiani, G. Psaroudis, and V. Tamma, "Quantum enhancement in time-delays estimation through spectrally resolved two-photon interference," 10 2021.

[53] R. Paschotta, "Beat note." RP Photonics Encyclopedia. Available online at `https://www.rp-photonics.com/beat_note.html`, url = https://www.rp-photonics.com/beat$_n$*ote.html*, *doi* = 10.61835/*ua*7*εtitle* = *εThislinkwillreloadthecurrentpage.*, *urldate* = 2024 − 08 − 08, *keywords* = *beatnote*.

[54] P. B. Patnaik, "The Non-Central χ 2 - and F-Distribution and their Applications," *Biometrika*, vol. 36, p. 202, 6 1949.

[55] M. Sankaran, "On the Non-Central Chi-Square Distribution," *Biometrika*, vol. 46, p. 235, 6 1959.

[56] K. Marwaha, *Practical Hematology for BDS*. Jaypee Bros. Medical Publishers, 2010.

[57] N. Adili, M. Melizi, and H. Belabbas, "Species determination using the red blood cells morphometry in domestic animals," *Veterinary World*, vol. 9, no. 9, pp. 960–963, 2016.

[58] P. M. Roma, L. Siman, F. T. Amaral, U. Agero, and O. N. Mesquita, "Total three-dimensional imaging of phase objects using defocusing microscopy: Application to red blood cells," *Applied Physics Letters*, vol. 104, 6 2014.

[59] G. L. Castoldi and L. del Senno, "Erythrocytes," in *Encyclopedia of Immunology (Second Edition)* (P. J. Delves, ed.), pp. 833–841, Oxford: Elsevier, second edition ed., 1998.

[60] M. Diez-Silva, M. Dao, J. Han, C.-T. Lim, and S. Suresh, "Shape and Biomechanical Characteristics of Human Red Blood Cells in Health and Disease," tech. rep.

[61] H. Park, S. Lee, M. Ji, K. Kim, Y. Son, S. Jang, and Y. Park, "Measuring cell surface area and deformability of individual human red blood cells over blood storage using quantitative phase imaging," *Scientific Reports*, vol. 6, 10 2016.

[62] K. Jaferzadeh, M. W. Sim, N. G. Kim, and I. K. Moon, "Quantitative analysis of three-dimensional morphology and membrane dynamics of red blood cells during temperature elevation," *Scientific Reports*, vol. 9, 12 2019.

[63] A. V. Belashov, A. A. Zhikhoreva, V. G. Bespalov, O. S. Vasyutinskii, N. T. Zhilinskaya, V. I. Novik, and I. V. Semenova, "Determination of the refractive index of dehydrated

cells by means of digital holographic microscopy," *Technical Physics Letters*, vol. 43, pp. 932–935, 10 2017.

[64] E. Lazareva and V. Tuchin, "Blood refractive index modelling in the visible and near infrared spectral regions," *Journal of Biomedical Photonics & Engineering*, vol. 4, p. 010503, 3 2018.

[65] Y. Yao, L. Ren, S. Gao, and S. Li, "Histogram method for reliable thickness measurements of graphene films using atomic force microscopy (afm)," *Journal of materials science & technology*, vol. 33, no. 8, pp. 815–820, 2017.

[66] B. Ndagano, H. Defienne, D. Branford, Y. D. Shah, A. Lyons, N. Westerberg, E. M. Gauger, and D. Faccio, "Quantum microscopy based on Hong–Ou–Mandel interference," *Nature Photonics*, vol. 16, pp. 384–389, 10 2022.

[67] A. C. Ulku, C. Bruschini, I. M. Antolovic, Y. Kuo, R. Ankri, S. Weiss, X. Michalet, and E. Charbon, "A 512×512 SPAD Image Sensor with Integrated Gating for Widefield FLIM," *IEEE journal of selected topics in quantum electronics : a publication of the IEEE Lasers and Electro-optics Society*, vol. 25, 1 2019.

[68] C. Bruschini, S. Burri, E. Charbon, T. Milanese, E. Bernasconi, and A. C. Ulku, "LinoSPAD2: an FPGA-based, hardware-reconfigurable 512×1 single-photon camera system," *Optics Express, Vol. 31, Issue 26, pp. 44295-44314*, vol. 31, pp. 44295–44314, 12 2023.

[69] D. B. Lindell, G. Wetzstein, and V. Koltun, "Acoustic Non-Line-of-Sight Imaging," tech. rep.

[70] N. Scheiner, F. Kraus, F. Wei, B. Phan, F. Mannan, N. Appenrodt, W. Ritter, J. DIckmann, K. DIetmayer, B. Sick, and F. Heide, "Seeing around Street Corners: Non-Line-of-Sight Detection and Tracking In-the-Wild Using Doppler Radar," *Proceedings of the IEEE Computer Society Conference on Computer Vision and Pattern Recognition*, pp. 2065–2074, 2020.

[71] T. Maeda, Y. Wang, R. Raskar, and A. Kadambi, "Thermal Non-Line-of-Sight Imaging," in *2019 IEEE International Conference on Computational Photography (ICCP)*, pp. 1–11, 2019.

[72] G. Gariepy, F. Tonolini, R. Henderson, J. Leach, and D. Faccio, "Detection and tracking of moving objects hidden from view," *Nature Photonics*, vol. 10, pp. 23–26, 1 2016.

[73] P. Caramazza, A. Boccolini, D. Buschek, M. Hullin, C. F. Higham, R. Henderson, R. Murray-Smith, and D. Faccio, "Neural network identification of people hidden from

view with a single-pixel, single-photon detector," *Scientific Reports*, vol. 8, no. 1, p. 11945, 2018.

[74] S. Chan, R. E. Warburton, G. Gariepy, J. Leach, and D. Faccio, "Non-line-of-sight tracking of people at long range," *Optics Express*, vol. 25, p. 10109, 5 2017.

[75] R. Geng, Y. Hu, and Y. Chen, "Recent Advances on Non-Line-of-Sight Imaging: Conventional Physical Models, Deep Learning, and New Scenes," 4 2021.

[76] M. Buttafava, J. Zeman, A. Tosi, K. Eliceiri, and A. Velten, "Non-line-of-sight imaging using a time-gated single photon avalanche diode," *Optics Express*, vol. 23, p. 20997, 8 2015.

[77] G. Musarra, A. Lyons, E. Conca, Y. Altmann, F. Villa, F. Zappa, M. J. Padgett, and D. Faccio, "Non-Line-of-Sight Three-Dimensional Imaging with a Single-Pixel Camera," *Physical Review Applied*, vol. 12, 7 2019.

[78] D. Faccio, A. Velten, and G. Wetzstein, "Non-line-of-sight imaging," 6 2020.

[79] A. Velten, T. Willwacher, O. Gupta, A. Veeraraghavan, M. G. Bawendi, and R. Raskar, "Recovering three-dimensional shape around a corner using ultrafast time-of-flight imaging," *Nature Communications*, vol. 3, 2012.

[80] M. Laurenzis, A. V. J. o. E. Imaging, and u. 2014, "Feature selection and back-projection algorithms for nonline-of-sight laser–gated viewing," *spiedigitallibrary.org*.

[81] V. Arellano, D. Gutierrez, and A. Jarabo, "Fast back-projection for non-line of sight reconstruction," *Optics Express*, vol. 25, no. 10, 2017.

[82] M. Otoole, D. B. Lindell, and G. Wetzstein, "Confocal non-line-of-sight imaging based on the light-cone transform," *Nature*, vol. 555, no. 7696, pp. 338–341, 2018.

[83] S. I. Young, D. B. Lindell, B. Girod, D. Taubman, and G. Wetzstein, "Non-line-of-sight surface reconstruction using the directional light-cone transform," in *Proceedings of the IEEE Computer Society Conference on Computer Vision and Pattern Recognition*, 2020.

[84] M. O'Toole, D. B. Lindell, and G. Wetzstein, "Real-time non-line-of-sight imaging," *ACM SIGGRAPH 2018 Emerging Technologies, SIGGRAPH 2018*, 8 2018.

[85] F. Heide, M. O'Toole, K. Zang, D. B. Lindell, S. Diamond, and G. Wetzstein, "Non-line-of-sight Imaging with Partial Occluders and Surface Normals," *ACM Transactions on Graphics*, vol. 38, 11 2017.

[86] C. Thrampoulidis, F. Xu, J. H. Shapiro, G. W. Wornell, F. N. C. Wong, G. Shulkind, and A. Torralba, "Revealing hidden scenes by photon-efficient occlusion-based opportunistic active imaging," *Optics Express, Vol. 26, Issue 8, pp. 9945-9962*, vol. 26, pp. 9945–9962, 4 2018.

[87] F. Heide, M. O'Toole, K. Zang, D. B. Lindell, S. Diamond, and G. Wetzstein, "Non-line-of-sight imaging with partial occluders and surface normals," *ACM Transactions on Graphics*, vol. 38, no. 3, 2019.

[88] X. Liu, I. Guillén, M. La Manna, J. H. Nam, S. A. Reza, T. Huu Le, A. Jarabo, D. Gutierrez, and A. Velten, "Non-line-of-sight imaging using phasor-field virtual wave optics," *Nature*, vol. 572, pp. 620–623, 8 2019.

[89] S. A. Reza, M. La Manna, S. Bauer, and A. Velten, "Phasor field waves: A Huygens-like light transport model for non-line-of-sight imaging applications," *Optics Express*, vol. 27, p. 29380, 9 2019.

[90] R. H. Stolt, "MIGRATION BY FOURIER TRANSFORM.," *Geophysics*, vol. 43, no. 1, 1978.

[91] D. B. Lindell, G. Wetzstein, and M. O'Toole, "Wave-based non-line-of-sight imaging using fast f-k Migration," *ACM Transactions on Graphics*, vol. 38, 7 2019.

[92] J. W. Goodman, *Speckle Phenomena in Optics: Theory and Applications*. Roberts & Company, 2007.

[93] I. Freund, M. Rosenbluh, and S. Feng, "Memory Effects in Propagation of Optical Waves through Disordered Media," *Physical Review Letters*, vol. 61, p. 2328, 11 1988.

[94] Y. Jauregui-Sánchez, H. Penketh, and J. Bertolotti, "Tracking moving objects through scattering media via speckle correlations," *Nature Communications*, vol. 13, 12 2022.

[95] J. Bertolotti, E. G. Van Putten, C. Blum, A. Lagendijk, W. L. Vos, and A. P. Mosk, "Non-invasive imaging through opaque scattering layers," *Nature*, vol. 491, pp. 232–234, 11 2012.

[96] O. Katz, P. Heidmann, M. Fink, and S. Gigan, "Non-invasive single-shot imaging through scattering layers and around corners via speckle correlations," *Nature Photonics*, vol. 8, pp. 784–790, 1 2014.

[97] C. Saunders, J. Murray-Bruce, and V. K. Goyal, "Computational periscopy with an ordinary digital camera," *Nature*, vol. 565, pp. 472–475, 1 2019.

[98] A. Beckus, A. Tamasan, and G. K. Atia, "Multi-Modal Non-Line-of-Sight Passive Imaging," *IEEE Transactions on Image Processing*, vol. 28, pp. 3372–3382, 7 2019.

[99] K. Tanaka, Y. Mukaigawa, and A. Kadambi, "Polarized non-line-of-sight imaging," *Proceedings of the IEEE Computer Society Conference on Computer Vision and Pattern Recognition*, pp. 2133–2142, 2020.

[100] J. G. Chopite, M. B. Hullin, M. Wand, and J. Iseringhausen, "Deep Non-Line-Of-Sight Reconstruction," tech. rep.

[101] W. Chen, S. Daneau, F. Mannan, and F. Heide, "Steady-state Non-Line-of-Sight Imaging," tech. rep.

[102] F. Mu, S. Mo, J. Peng, X. Liu, J. H. Nam, S. Raghavan, A. Velten, and Y. Li, "Physics to the Rescue: Deep Non-line-of-sight Reconstruction for High-speed Imaging," *IEEE Transactions on Pattern Analysis and Machine Intelligence*, 5 2022.

[103] J. He, Y. Zhang, S. Wu, and R. Wei, "Non-line-of-sight imaging and tracking of moving objects based on deep learning," *Optics Express, Vol. 30, Issue 10, pp. 16758-16772*, vol. 30, pp. 16758–16772, 5 2022.

[104] S. Zheng, S. Zheng, S. Zheng, M. Liao, M. Liao, F. Wang, F. Wang, W. He, X. Peng, G. Situ, G. Situ, and G. Situ, "Non-line-of-sight imaging under white-light illumination: a two-step deep learning approach," *Optics Express, Vol. 29, Issue 24, pp. 40091-40105*, vol. 29, pp. 40091–40105, 11 2021.

[105] F. Heide, M. M. Balaji, R. G. Baraniuk, A. Veeraraghavan, P. Rangarajan, A. Viswanath, and C. A. Metzler, "Deep-inverse correlography: towards real-time high-resolution non-line-of-sight imaging," *Optica, Vol. 7, Issue 1, pp. 63-71*, vol. 7, pp. 63–71, 1 2020.

[106] W. Chen, F. Wei, K. N. Kutulakos, S. Rusinkiewicz, and F. Heide, "Learned feature embeddings for non-line-of-sight imaging and recognition," *ACM Transactions on Graphics*, vol. 39, 11 2020.

[107] M. Isogawa, Y. Yuan, M. O'Toole, and K. Kitani, "Optical non-line-of-sight physics-based 3d human pose estimation," *Proceedings of the IEEE Computer Society Conference on Computer Vision and Pattern Recognition*, pp. 7011–7020, 2020.

[108] A. Kotwal, A. Levin, and I. Gkioulekas, "Swept-Angle Synthetic Wavelength Interferometry," 5 2022.

[109] F. Li, F. Willomitzer, M. M. Balaji, P. Rangarajan, and O. Cossairt, "Exploiting Wavelength Diversity for High Resolution Time-of-Flight 3D Imaging," *IEEE Transactions on Pattern Analysis and Machine Intelligence*, vol. 43, pp. 2193–2205, 7 2021.

[110] F. Willomitzer, P. V. Rangarajan, F. Li, M. M. Balaji, M. P. Christensen, and O. Cossairt, "Fast non-line-of-sight imaging with high-resolution and wide field of view using synthetic wavelength holography," *Nature Communications*, vol. 12, 12 2021.

[111] A. Gröger, G. Pedrini, F. Fischer, D. Claus, I. Aleksenko, and S. Reichelt, "Two-wavelength digital holography through fog," *Journal of the European Optical Society-Rapid Publications*, vol. 19, no. 1, p. 25, 2023.

[112] E. Abbe, "Beiträge zur Theorie des Mikroskops und der mikroskopischen Wahrnehmung," *Archiv für Mikroskopische Anatomie*, vol. 9, pp. 413–468, 12 1873.

[113] K. Khare, "The Angular Spectrum Method," *Fourier Optics and Computational Imaging*, pp. 145–151, 9 2015.

[114] K. Khare, M. Butola, and S. Rajora, *Fourier optics and computational imaging*. Springer, 2015.

[115] V. T. Keränen, A. J. Mäkynen, A. L. Dayton, and S. A. Prahl, "Polyurethane Phantoms with Homogeneous and Nearly Homogeneous Optical Properties," tech. rep.

[116] T. Moffitt, Y.-C. Chen, and S. A. Prahl, "Preparation and characterization of polyurethane optical phantoms," *Journal of Biomedical Optics*, vol. 11, no. 4, p. 041103, 2006.

[117] L. Gao and X. Feng, "Toward Non-Line-of-Sight Videography," *Optics and Photonics News, Vol. 32, Issue 11, pp. 22-29*, vol. 32, pp. 22–29, 11 2021.

[118] T. Fortier and E. Baumann, "20 years of developments in optical frequency comb technology and applications," *Communications Physics 2019 2:1*, vol. 2, pp. 1–16, 12 2019.

[119] S. B. Papp, P. Del'Haye, S. A. Diddams, K. Beha, K. J. Vahala, H. Lee, and F. Quinlan, "Microresonator frequency comb optical clock," *Optica, Vol. 1, Issue 1, pp. 10-14*, vol. 1, pp. 10–14, 7 2014.

[120] V. Torres-Company and A. M. Weiner, "Optical frequency comb technology for ultra-broadband radio-frequency photonics," *Laser & Photonics Reviews*, vol. 8, pp. 368–393, 5 2014.

[121] N. Picqué and T. W. Hänsch, "Frequency comb light sources for spectroscopy,"

[122] T. Udem, R. Holzwarth, and T. W. Hänsch, "Optical frequency metrology," *Nature 2002 416:6877*, vol. 416, pp. 233–237, 3 2002.

[123] J. Yang, X. Zhao, L. Zhang, and Z. Zheng, "Single-cavity dual-comb fiber lasers and their applications," *Frontiers in Physics*, vol. 10, p. 1070284, 1 2023.

[124] L. S. Ma, Z. Bi, A. Bartels, L. Robertsson, M. Zucco, R. S. Windeler, G. Wilpers, C. Oates, L. Hollberg, and S. A. Diddams, "Optical frequency synthesis and comparison with uncertainty at the 10(-19) level," *Science (New York, N.Y.)*, vol. 303, pp. 1843–1845, 3 2004.

[125] A. Bartels, D. Heinecke, and S. A. Diddams, "10-GHz self-referenced optical frequency comb," *Science*, vol. 326, p. 681, 10 2009.

[126] F. C. Cruz, W. H. Oskay, S. A. Diddams, E. A. Donley, T. M. Fortier, T. P. Heavner, L. Hollberg, W. M. Itano, S. R. Jefferts, M. J. Delaney, K. Kim, F. Levi, T. E. Parker, J. C. Bergquist, D. Ludlow, T. Zelevinsky, G. K. Campbell, S. Blatt, M. M. Boyd, M. H. G de Miranda, M. J. Martin, J. W. Thomsen, S. M. Foreman, J. Ye, J. E. Stalnaker, Y. Le Coq, Z. W. Barber, N. Poli, N. D. Lemke, K. M. Beck, and C. W. Oates, "Optical frequency combs generated by fourwave mixing in optical fibers for astrophysical spectrometer calibration and metrology," *Optics Express, Vol. 16, Issue 17, pp. 13267-13275*, vol. 16, pp. 13267–13275, 8 2008.

[127] P. Del'Haye, A. Schliesser, O. Arcizet, T. Wilken, R. Holzwarth, and T. J. Kippenberg, "Optical frequency comb generation from a monolithic microresonator," *Nature 2007 450:7173*, vol. 450, pp. 1214–1217, 12 2007.

[128] H. Murata, A. Morimoto, T. Kobayashi, and S. Yamamoto, "Optical pulse generation by electrooptic-modulation method and its application to integrated ultrashort pulse generators," *IEEE Journal on Selected Topics in Quantum Electronics*, vol. 6, pp. 1325–1331, 11 2000.

[129] R. Liao, H. Tian, W. Liu, R. Li, Y. Song, and M. Hu, "Dual-comb generation from a single laser source: principles and spectroscopic applications towards mid-IR—A review," *Journal of Physics: Photonics*, vol. 2, p. 042006, 9 2020.

[130] C. Zhang, F. Qu, P. Ou, H. Sun, S. He, and B. Fu, "Recent Advances and Outlook in Single-Cavity Dual Comb Lasers," *Photonics 2023, Vol. 10, Page 221*, vol. 10, p. 221, 2 2023.

[131] X. Zhao, Z. Zheng, Y. Liu, G. Hu, and J. Liu, "Dual-Wavelength, Bidirectional Single-Wall Carbon Nanotube Mode-Locked Fiber Laser," *IEEE Photonics Technology Letters*, vol. 26, pp. 1722–1725, 9 2014.

[132] N. Prakash, S.-W. Huang, S.-W. Huang, B. Li, and B. Li, "Relative timing jitter in a counterpropagating all-normal dispersion dual-comb fiber laser," *Optica, Vol. 9, Issue 7, pp. 717-723*, vol. 9, pp. 717–723, 7 2022.

[133] B. Li, B. Li, J. Xing, D. Kwon, Y. Xie, N. Prakash, J. Kim, and S.-W. Huang, "Bidirectional mode-locked all-normal dispersion fiber laser," *Optica, Vol. 7, Issue 8, pp. 961-964*, vol. 7, pp. 961–964, 8 2020.

[134] N. Prakash, J. Musgrave, B. Li, B. Li, B. Li, and S.-W. Huang, "Dynamic counterpropagating all-normal dispersion (DCANDi) fiber laser," *Photonics Research, Vol. 12, Issue 9, pp. 2033-2046*, vol. 12, pp. 2033–2046, 9 2024.

[135] J. B. Bates, "Fourier transform spectroscopy," *Computers and Mathematics with Applications*, vol. 4, no. 2, pp. 73–84, 1978.

[136] I. Coddington, W. Swann, and N. Newbury, "Dual-comb spectroscopy," *Optica, Vol. 3, Issue 4, pp. 414-426*, vol. 3, pp. 414–426, 4 2016.

[137] D. T. Reid, Z. Zhang, and T. Gardiner, "Mid-infrared dual-comb spectroscopy with an optical parametric oscillator," *Optics Letters, Vol. 38, Issue 16, pp. 3148-3150*, vol. 38, pp. 3148–3150, 8 2013.

[138] H. Wright, J. Sun, D. McKendrick, N. Weston, and D. T. Reid, "Two-photon dual-comb LiDAR," *Optics Express, Vol. 29, Issue 23, pp. 37037-37047*, vol. 29, pp. 37037–37047, 11 2021.

[139] H. Wright, A. J. M. Nelmes, N. J. Weston, and D. T. Reid, "Multi-target two-photon dual-comb LiDAR," *Optics Express*, vol. 31, p. 22497, 7 2023.

[140] Z. Zhu and G. Wu, "Dual-Comb Ranging," 12 2018.

[141] B. Martin, B. Martin, P. Feneyrou, D. Dolfi, and A. Martin, "Performance and limitations of dual-comb based ranging systems," *Optics Express, Vol. 30, Issue 3, pp. 4005-4016*, vol. 30, pp. 4005–4016, 1 2022.

[142] C. H. Moore and W. Lin, "FPGA Correlator for Applications in Embedded Smart Devices," *Biosensors*, vol. 12, no. 4, 2022.

[143] S. Saxena, D. R. Paskvan, N. R. Weir, and N. Sinclair, "A field programmable gate array-based timing and control system for the dynamic compression sector," *Review of Scientific Instruments*, vol. 93, no. 4, 2022.

[144] B. Wang, M. Y. Zheng, J. J. Han, X. Huang, X. P. Xie, F. Xu, Q. Zhang, and J. W. Pan, "Non-Line-of-Sight Imaging with Picosecond Temporal Resolution," *Physical Review Letters*, vol. 127, p. 053602, 7 2021.